UNED

EIDUNED
Escuela
Internacional
de Doctorado

GOBIERNO DE ESPAÑA
MINISTERIO DE CIENCIA E INNOVACIÓN

Ciemat
Centro de Investigaciones Energéticas, Medioambientales y Tecnológicas

TESIS DOCTORAL

2023

REAL TIME PERFORMANCE ANALYSIS OF AN OPTIMIZED LINEAR DISRUPTION PREDICTOR IN JET

Dhaval Gadariya

PROGRAMA DE DOCTORADO EN INGENIERIA DE SISTEMAS Y CONTROL

Dr. JESÚS ANTONIO VEGA SÁNCHEZ
Dr. SEBASTIÁN DORMIDO CANTO

Dedication

To my mother, for her unwavering support and belief in my capacities alongside constant efforts to help me reach where I am today.

Acknowledgements

Words cannot express my sincere gratitude to my supervisors, Dr Jesús Vega and Dr Sebastián Dormido-Canto, for their constant support, motivation and guidance throughout the duration of my PhD. It would be unfair to say that it would have been possible without their efforts alongside mine. Special mention should also be made of Dr Giuseppe Rattá and Dr Andrea Murari, who helped me at crucial moments. I would also like to thank the EUROFUSION consortium and the LNF for the financial support that I have been given to complete this Ph.D. thesis.

My friends from CIEMAT, starting with Sadig, with whom I not only shared the office, but also, the experience of navigating through the hardships of research life. Thank you very much for being always present, for listening when I need to vent and asking me to push when I felt I had nothing left in the tank. Gianluca, Sebastian, Antonio, Manolis, colleagues from the technology group, friends from the Fusion EP master course and everyone from building 20F- the list can be endless: thank you very much for all your support. Your presence made this work much more enjoyable and the whole experience an enriching one.

Friends who I have known for what it seems like an eternity: Isabella, Nishit, Jessica, Ana, María, Mosam, Pamu, Akshay, Charitarth and the whole SVNIT Physics Lab group as well as Chamartín bádminton group. Thank you very much for your constant support, for standing beside me when I felt lost and tired, for opening your hearts when I needed shelter and most of all, for believing in me and telling me time and time again that I can do it.

My dearest brother, Vaibhav: thank you very much for taking care of our mother and by doing so, permitting me to chase my dream. I am indebted to you for your constant contribution in me being able to fully concentrate on the task at hand. Both my aunts, Dhanlaxmi and Sushma; for your consistent efforts to take care of my mother and help Vaibhav, especially when she went through a lengthy period of severe illness. Your presence in Surat made sure I could focus on my work without having to worry much about the well-being of my mother.

Last, but not the least, my mother: thank you very much, for being my rock, my refuge, my protector and my biggest supporter. Thank you for teaching me to never give up- no matter what life throws at me. Thank you for being patient with me, when I lost mine. Thank you for being who you are. This work is as much yours as it is mine. Thank you, Maa!

Index

List of Figures

List of Tables

List of Symbols and Acronyms

AI	Artificial Intelligence
ALCATOR C-MOD	Alto Campo Toro C-MODification
ANN	Artificial Neural Network
APODIS	Advance Predictor Of DISruptions
ASDEX	Axially Symmetric Divertor Experiment
BS	Baseline Scenario
CART	Classification And Regression Trees
CCFE	Culham Centre for Fusion Energy
CFC	Composite Carbon Fiber
CIEMAT	Centro de Investigaciones Energéticas, Medioambientales y Tecnológicas
CM	Centroid Method
COMPASS	COMPact ASSembly
CQ	Current Quench
DDB	Dynamic Data Buffer
DEMO	DEMOnstration Power plant
DF	Decision Function
DMV	Disruption Mitigation Valve
DT	Deuterium-Tritium
EAST	Experimental Advanced Superconducting Tokamak
EFCC	Error Field Correction Coils
ELM	Edge Localized Mode
EURATOM	EURopean ATOMic energy community
FDI	Fault Detection and Isolation
FPGA	Field Programmable Gate Array
FWC	First Wall Component
GAM	Generic Application Module
ICRH	Ion Cyclotron Resonance Heating
HPC	High Performance Computing
HS	Hybrid Scenario
IAEA	International Atomic Energy Agency
IID	Independent and Identically distributed Data
ILW	ITER-Like Wall
INTOR	International TOkamak Reactor

ITER	International Thermonuclear Experimental Reactor
JET	Joint European Torus
JPN	JET Pulse Number
JPS	JET Protection System
JT-60	Japan Torus-60
JT-60SA	Japan Torus-60 Super Advanced
JT-60U	Japan Torus-60 Upgrade
KSTAR	Korea Superconducting Tokamak Advanced Research
LNF	Laboratorio Nacional de Fusión
MARTe	Multithreaded Application Real-Time executor
MCF	Magnetic Confinement Fusion
MHD	Magneto-HydroDynamic
ML	Mode Lock amplitude
MPTD	Magnetic Perturbation Time Derivative
NBI	Neutral Beam Injection
NCT	Nearest Centroid Taxonomy
NTM	Neoclassical Tearing Mode
PBOD	Predictor Based on Outlier Detection
PDX	Poloidal Divertor eXperiment
PETRA	Plasma Event TRiggering for Alarms
PFC	Plasma Facing Component
RF	Radio Frequency
RFX	Reverse-Field eXperiment
ROC	Receiver Operating Characteristic
RTN	Real Time Network
RTPS	Real Time Protection Sequencer
SOL	Scrape-Off Layer
SOM	Self-Organized Map
SPAD	Single signal Predictor based on Anomaly Detection
SVM	Support Vector Machine
SXR	Soft X-Ray
TM	Tearing Mode
TOKAMAK	TOroidalbnaya KAmera MAgnitnim Katushkami
TQ	Thermal Quench
VDE	Vertical Displacement Event
VV	Vacuum Vessel
WEST	Tungsten(W) Environment in Steady-state Tokamak

List of publications

1. "Performance analysis of the centroid method predictor implemented in the JET real time network"
   D. Gadariya, J. Vega, C. Stuart, G. Rattá, P. Card, A. Murari, S. Dormido-Canto and JET Contributors, Plasma Phys. Control. Fusion **64** (2022) 114004
2. "Characterization of physics events in JET preceding disruptions"
   G. A. Rattá, J.Vega, A.Murari, **D. Gadariya**, C.Stuart, G.Farías and JET Contributors, Fusion Engineering and Design **189** (2023) 113468
3. "PHAD: a phase-oriented disruption prediction strategy for avoidance, prevention, and mitigation in JET"
   G. A. Rattá, J. Vega, A. Murari, **D. Gadariya** and JET Contributors, Nucl. Fusion **61** (2021) 116055
4. "A linear equation based on signal increments to predict disruptive behaviours and the time to disruption on JET"
   J. Vega, A. Murari, S. Dormido-Canto, F. Hernández, T. Cruz, **D. Gadariya**, G.A. Rattá and JET Contributors, Nucl. Fusion **60** (2020) 026001

Conferences

1. "Comparison of unsupervised methods to determine common patterns in the termination phase of disruptive discharges in JET"
   J. Vega, R. Dormido, S. Dormido-Canto, G. Rattá, **D. Gadariya**, A. Murari and JET Contributors
   4th IAEA Technical Meeting on Fusion Data Processing,
   Validation and Analysis (2021) Chengdu, China.
2. "Review of a data-driven adaptive disruption predictor for mitigation based on a nearest centroid approach"
   J. Vega, G. A. Rattá, **D. Gadariya**, A. Murari, C. Stuart, S. Dormido-Canto and JET Contributors
   2nd IAEA technical meeting on plasma disruptions and their mitigation (2022), Saint Paul lez Durance, France.
3. "Characterization of physics events in JET preceding disruptions"
   G.A.Rattá, J.Vega, A. Murari, **D. Gadariya**, C. Stuart and JET Contributors, 32nd Symposium on Fusion Technology. 18-23 September 2022. Dubrovnik, Croatia.

4. "Building a parsimonious disruption mitigation trigger"
   J. Vega, G. A. Rattá, **D. Gadariya**
   2022 WPSA General Meeting.
5. "Anomaly Detection and Unsupervised Classification of Plasma Events"
   J. Vega, **D. Gadariya**, G. Rattá, A. Murari
   14^{th} Chaotic Modeling and Simulation International Conference. 8 – 11 June 2021. Athens, Greece
6. "Prediction of Disruptive Events on the Route to Nuclear Fusion Reactors"
   J. Vega, R. Dormido, S. Dormido-Canto, G. A. Rattá, **D. Gadariya**, A. Murari
   ISC High Performance 2021 Conference, June 24^{th} –July 2^{nd} 2021.
7. "Disruption predictors in nuclear fusion by using machine learning methods: an overview"
   J. Vega, A. Murari, G. A. Rattá, S. Dormido-Canto, **D. Gadariya** and JET Contributors
   1^{st} Workshop on Artificial Intelligence in Plasma Science. 20^{th} – 22^{nd} September 2021. Aix-en-Provence, France

Chapter 1 – Nuclear Fusion

This chapter contains a brief introduction to nuclear fusion, with main focus on magnetically confined controlled thermonuclear reaction. Also, a quick overview is given on JET- the current flagship fusion experiment and ITER- the experiment whole world is eagerly waiting to begin operation.

1.1. Introduction

Global environmental crisis has led humankind to search for effective alternatives to traditional energy sources. What started as a breakthrough with the invention of wheel, progressively grew with inventions of electricity and eventually culminated in industrial revolutions- the human evolution has lately shown the ugly side of overexploitation of natural resources. Repercussions have been massive and according to reports [1], it is just the beginning. Strides made in scientific discoveries taught us different ways to produce electricity, but the primary source has been combustion of fossil fuels. Coal and natural gas, with their abundance at the time of their discovery and comparatively smaller global energy demand- had become "traditional" fuels for energy production, dating thousands of years before the invention of steam engines. Steam engines changed the face of the earth- figuratively and literally; instigating the industrial revolution where we built machinery for mass production of utilities. Construction of heavy machinery resulted in drastic change of human lifestyle. Animal driven carts were quickly replaced by motorized vehicles. Steam powered trains and ships which used coal in the boilers became a faster way of transportation. But even before coal, wood was being used for heating- another organic material which upon combustion, liberates CO_2. The demand and use of coal, however, shot through the roofs upon realization that the energy liberated by burning of coal was much higher. Also, the fact that coal was much easier to transport compared to the wood made it the Materia prima for the industry.

Fast forward to the 19^{th} century and we are at another historical landmark- the discovery of crude oil. Edwin L Drake, drilling the first modern commercial oil well accompanied by advances in chemistry to refine the crude oil in order to obtain useful petroleum products provided a gigantic leap towards further acceleration of the industrial revolution. Kerosene for lighting lamps and gasoline for internal combustion engines quickly converted crude oil into a tool for world dominance, leading to world wars.

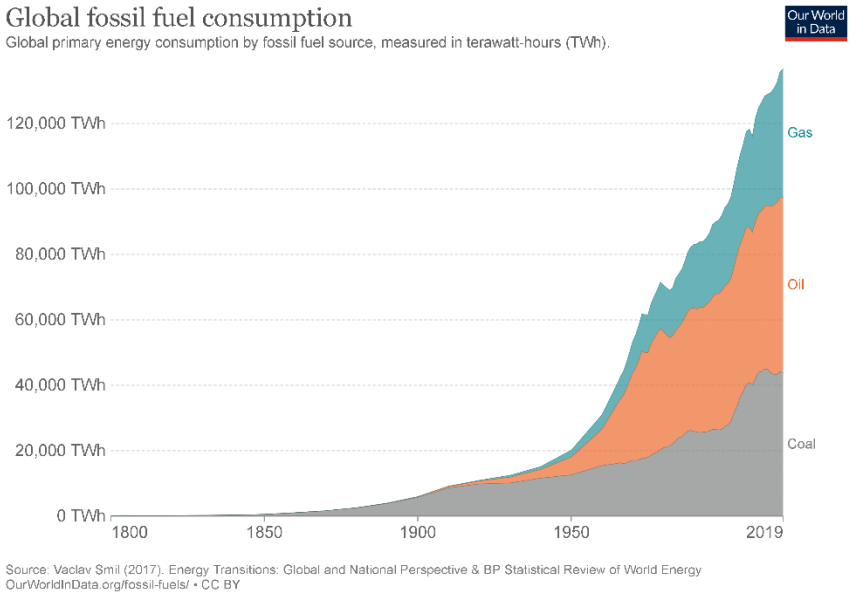

Figure 1.1: Global fossil fuel consumption chart [1]

If put into a general class, all the variety of fossil fuel belong to hydrocarbons- compounds consisting predominantly carbon and hydrogen and sometimes nitrogen, oxygen, sulfur. Assuming we have hydrocarbons containing only carbon and hydrogen, the chemical reaction of their complete combustion for energy production can be represented by following equation:

$$C_xH_{2x+2} + \left(\frac{3x+1}{2}\right) O_2 \xrightarrow{yields} xCO_2 + (x+1)\, H_2O$$

In case of hydrocarbons with either of nitrogen, oxygen or sulfur, several other unwanted byproducts are obtained. The liberated carbon dioxide is the main culprit of the greenhouse effect, trapping the heat in terrestrial atmosphere. We have named this phenomenon as global warming and even though, it is a little too late, there is a general consensus about the adverse effects of it. From as basic as melting of glaciers and rising sea levels to frequent wildfires and long draughts are some examples of consequences of global warming. Projections for future global temperature for different scenarios of CO_2 emission are alarming and we need to cut down drastically on our fossil fuel consumption in order to salvage the environment and the planet.

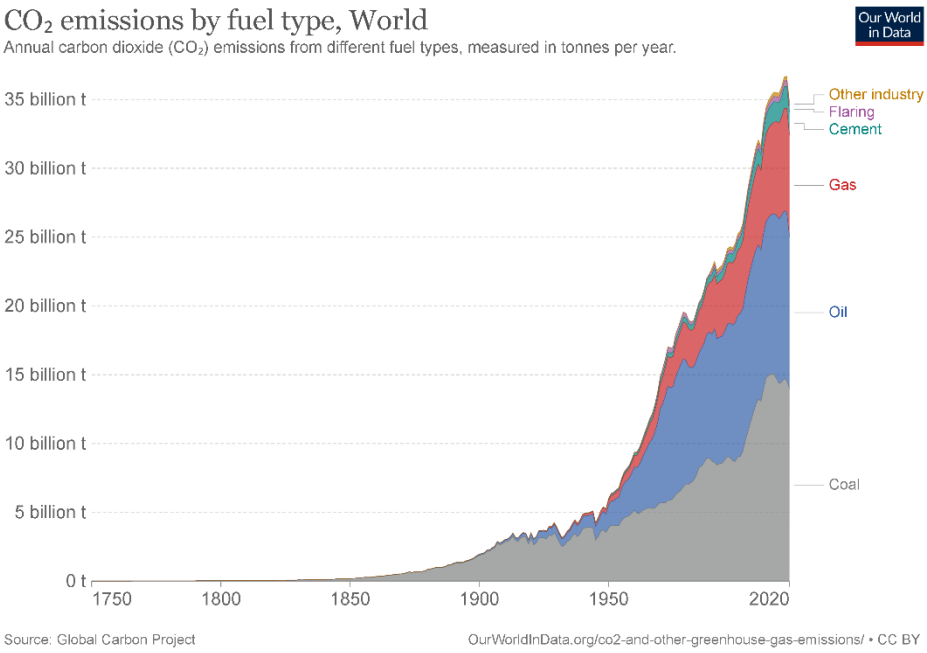

Figure 1.2: Global CO_2 emissions by fuel type [1]

The advent of atomic energy has played a very important role in keeping the CO_2 emissions in check. However, another problem, that of radioactive nuclear waste with a half-life time of tens of thousands of years and accidents like Chernobyl and Fukushima have rendered the comparatively better option of nuclear energy rather questionable. So much so, that several European countries like Germany, Italy, Spain and many more have decided to shut down their nuclear power plants [2] and opt for renewables like solar, wind and thermal energy. Traditional nuclear power plants use nuclear fission of Uranium 235 for energy production. However, up until recent decade, where modern modular reactors have been developed, the efficiency of the fuel cycle was quite low, which led to large amounts of fission fuel going to "waste". A recent study made by researchers of Stanford and University of British Columbia [3] has pointed out that even the small modular reactors, which are projected as a cleaner and more efficient alternative of the first generation reactors, will actually generate more radioactive waste than the conventional nuclear power plants. Fission is not the only pathway to nuclear energy. It is actually the least used form of nuclear energy on the universal scale. The cleaner and more abundant source of nuclear energy is Nuclear Fusion. Fusion per se does not produce radioactive residuals because it uses light atoms (mostly isotopes of Hydrogen and Helium) as fuels, which are available in abundance.

All the stars in the universe produce their energy via the nuclear fusion reaction. While in fission we break a heavy nucleus into several lighter ones to produce energy based on the mass defect, fusion combines two light nuclei to produce a heavier one and the resultant mass defect, can be harnessed to generate electricity using the famous Einstein equation:

$$E = \Delta mc^2$$

where Δm is the mass defect, c is the speed of light and E is the resultant energy.

Nuclear fusion in stars is made possible due to the gravitational confinement of matter. If stars were to be put into a single category based on what they are comprised of, that category could easily be termed as "Giant gaseous balls". These gaseous balls are very densely packed. The sun, which by no means is a "GIANT" in astrophysical terms, has a density of approximately 150 g/cm^3 [4] in the core- which is almost 10 times the density of gold. In such high-density region, the temperature also starts rising due to the collisions among Hydrogen gas molecules. As of today, the solar core is estimated to have a temperature of 15 million K. At these temperatures, all the visible matter gets converted to the 4th state- plasma. Plasma is a state of matter where due to high temperatures, almost all the atoms are stripped off their electrons and what remains is a very hot mix of electrons, ions and some neutral atoms and molecules. The nuclei, upon having such high energies, can overcome what is known as the Coulomb barrier and repulsion caused by the Coulomb force between like charges and end up going through the fusion reaction, where they combine to produce new nuclei.

The most important chain reaction responsible for energy production in solar core is known as the proton-proton chain reaction where four Hydrogen nuclei form a Helium nucleus. It is not a straightforward reaction, rather it occurs in stages.

$$^1_1H + {}^1_1H \rightarrow {}^2_1D + e^+ + \upsilon_e$$

$$^2_1D + {}^1_1H \rightarrow {}^3_2He + \gamma$$

$$^3_2He + {}^3_2He \rightarrow {}^4_2He + {}^1_1H + {}^1_1H$$

the total energy released at the end of the above cycle is 26.7 MeV. Once initiated, the reaction is self-sufficient if not all the Hydrogen in the core is converted into Helium. Abundant amounts of Hydrogen in core of stars would

mean that it might even take billions of years to use up all the Hydrogen. In stars, the massive gravitational force owing to their mass takes care of confining the plasma so that the proton-proton cycle continues occurring non-stop. Hence, in case of stars, the gravity not only plays a major part in igniting nuclear fusion but also, in maintaining it continuous by means of **gravitational confinement**. It is, however, unrealistic for the moment to be able to produce and maintain such high-density levels of a gas on earth. Worth mentioning is the fact that the first ever occurrence of fusion of two protons into a deuteron is so rare that the characteristic time for it at the extremely high temperatures and densities of the solar core is still a billion years. Mankind has therefore sought to use various methods to harness nuclear fusion for energy production on planet Earth. **Inertial confinement** and **magnetic confinement** are the other two methods being investigated into for exploitation of nuclear fusion as a source of energy.

For inertial confinement fusion, the fuel nuclei are located in form of a capsule inside a *hohlraum*- a German word for cavity. Intense laser beams are used to irradiate the fuel capsule, resulting in intense x-rays produced by the hohlraum, causing ablation-and hence, explosion of the outer portion of fuel capsule. Newton's third law guarantees an implosion of the inner portion of the fuel capsule, causing an effect of supercompression on the fuel material, raising the material density as high as 1000 g/cm^3. This density, however, is still not sufficient for causing the nuclei to fuse. The collapse of the fuel material causes shockwaves, which travel at very high speeds towards the center of the fuel. These shockwaves eventually collide inside the core of the fuel capsule and resultantly raise the density as well as temperature of the spot of collision. Such a rapid increment in density and temperature can assure there is enough kinetic energy for the nuclei to overcome the electrostatic repulsion and sufficient amount of fuel nuclei to maintain the fusion reaction rate high enough to reach *ignition*- a self-sustained state of burn. The alpha particles produced by the Deuteron-Triton (DT) fusion reaction also contribute to maintaining the reaction rate because high density in the surroundings result in thermalization of these alpha particles due to collision, eventually increasing the fusion rate.

$$ {}^{2}_{1}D + {}^{3}_{1}H \rightarrow {}^{4}_{2}He + {}^{1}_{0}n $$

The Q value of DT reaction amounts to be 17.58 MeV out of which 3.52 MeV is carried by the alpha particle and the remaining 14.06 MeV is carried by the neutron. Here it is important to mention the role a term often used in nuclear fusion community- the reaction cross-section plays for selecting the DT reaction. The reaction cross-section is defined as the probability of occurrence of a particular reaction under the influence of an excitation mechanism. In case of fusion reaction, the cross-section taken into consideration is a function of the relative velocity of the two reactant nuclei. As per usual convention in nuclear and high energy physics, the velocity is represented by energy, in particular, the kinetic energy. For a collection of reactants, the velocity and hence, the kinetic energy is usually defined in terms of a distribution function. An average computed over the distributions of the product of cross-section and velocity is termed as the *reactivity*. As can be seen in figure 1.3, the reactivity does not have a linear relation with the temperature of the reactants, instead, has a particular high value for each set of reactants at particular temperatures.

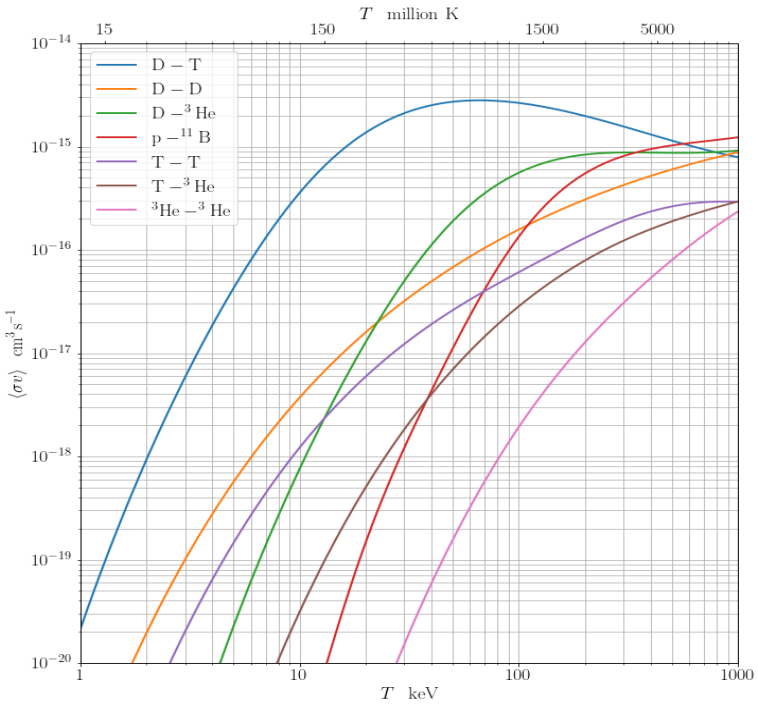

Figure 1.3: Reaction cross-sections as a function of temperature for nuclear fusion candidates [5]

In the next section, a brief overview is given on magnetic confinement fusion which encompasses some basic concepts starting from plasma physics up to various problems and challenges encountered in realization of a successful magnetic confinement scheme.

1.2. Magnetic Confinement Fusion (MCF)

The highest value of reactivity is obtained for a DT reaction at temperatures as high as ~100 keV and hence, the DT reaction is preferred for most of the ongoing fusion research. There exist some privately funded research start-ups which use other candidate reactions for fusion energy production from figure 1.3 to demonstrate their capability to achieve further extreme conditions. It is clearly demonstrated in figure 1.3 that for any other reaction different to DT, the temperature required to achieve highest reactivity is similar to that for the DT reaction but the maxima of reactivity curve is at lower value compared to the one for DT.

At such high temperatures, the reactants reach the plasma state. However, not every hot mix of charged and neutral particles can be termed a plasma because there are several characteristic quantities which are used to define a plasma- mainly macroscopic neutrality, Debye length and plasma frequency. Macroscopic neutrality means that in the absence of external forces, the plasma volume is large enough to contain many particles, but small enough that the particle density and temperature remain uniform and the net electric charge within such a plasma volume is zero. In other words, the macroscopic charge neutrality is obtained by mutual cancellation of microscopic electric fields generated by charge separation inside the plasma volume. However, natural departure from macroscopic neutrality can occur at distances large enough where the energy imbalance produced by appearance of an electrostatic potential is countered and nullified by the thermal energy of plasma particles. Since this distance plays a major part in maintaining the macroscopic neutrality, it is considered to be a characteristic distance, named after Peter Debye and his pioneering work in explanation of its existence. The Debye length is defined as the distance over which the influence of the electric field created by a charged particle is felt by the other charged particles inside the plasma. Charged particles arrange themselves inside the plasma such that effect of other charged particles is effectively screened within the distance of the order of Debye length. For plasmas, Debye length is given by:

$$\lambda_D = \sqrt{\frac{\varepsilon_0 kT}{n_e e^2}}$$

In other words, Debye length can also be understood as the distance beyond which, fluctuating electric fields may appear inside a plasma. For laboratory plasmas, λ_D can be of the order of 100 μm where for plasmas spanning over large distances, it can go as high as of the order of several hundred km. Which means that a necessary condition that the dimension of the plasma L be much greater than λ_D because otherwise there is no sense for Debye shielding. Mathematically,

$$\lambda_D \ll L$$

A sphere of radius λ_D can be termed a Debye sphere and it will have a characteristic property that the particles inside the Debye sphere can only feel the effect of the electric fields produced by the remaining particles inside. Any resultant electric field outside of the Debye sphere has no effect on the particles inside. The number of electrons inside a Debye sphere is given by:

$$N_D = \frac{4}{3}\pi\lambda_D^3 n_e = \frac{4}{3}\pi\sqrt{\left(\frac{\varepsilon_0 kT}{\sqrt[3]{n_e}e^2}\right)^3}$$

Once again, for effective shielding and hence, consistent collective behavior, the number of electrons inside a Debye sphere must be very large. Keeping in mind the usual value of λ_D for laboratory plasmas, one can conclude that:

$$N_D \gg> 1$$

For a medium to remain in plasma state, the condition of macroscopic neutrality must be fulfilled but there are instances where due to external perturbations, an instantaneous space charge distribution can be created inside the plasma volume. Such a charge separation is often countered by the collective oscillatory motion of the plasma particles and the frequency of these oscillations is known as the plasma frequency. These oscillations are of very high frequency, which make it near impossible for the massive ions to follow the electron motion due to inertia. Eventually, the electrons end up oscillating about ions and the electron-ion Coulomb force provides an effective counterbalancing measure. Since the oscillations are practically electron oscillations, the oscillation frequency is termed as plasma electron frequency and is given by:

$$\nu_{pe} = \frac{1}{2\pi}\sqrt{\frac{n_e e^2}{\varepsilon_0 m_e}}$$

Plasma, however, does not only comprise of electrons and ions. There can be neutrals as well and these neutral particles can create a hindrance to the process of re-establishment of macroscopic neutrality by means of colliding with electrons, eventually causing them to dissipate the energy they gained via the electron-ion Coulomb attraction force. The electron neutral collision frequency (ν_{en}) must be very negligible compared to ν_{pe} for achieving macroscopic neutrality once again after removal of the external perturbation. This discussion leads us to the third and final condition for definition of plasma.

$$\omega\tau > 1$$

where $\omega = 2\pi\nu_{pe}$, the angular frequency of typical plasma oscillations and $\tau = \frac{1}{\nu_{en}}$ is the time between two consecutive electron neutral collisions. In other words, there must be several electron plasma oscillations in between two successive electron neutral collisions to guarantee that the medium is still a plasma and not a neutral gas where the particles are dissipating energy by means of collisions.

The reason behind such an extensive definition of what is plasma is the fact that 99% of the visible matter in the universe is in plasma form. Solar core, nebulae, intergalactic medium, earth's atmosphere are some examples of naturally occurring plasmas. Different particle densities and collective temperatures characterize different types of plasmas and hence, different methods to exploit them for our benefit. Cold plasmas can be used for surface treatment and hot plasmas can provide the perfect playground for nuclear fusion. The question though, remained one of the highly sought-after ones about how to use such hot plasmas for nuclear fusion. In late 1920s, the idea to use magnetic field for controlling charged particles' motion without making them lose energy was first experimented upon. A moving charged particle under the influence of an electromagnetic field feels a force given by:

$$F = q[E + (v \times B)]$$

here $\boldsymbol{F}$ is the Lorentz force, q is the charge of the particle under observation, $\boldsymbol{E}$ is the electric field, v is the velocity and $\boldsymbol{B}$ is the magnetic field. In the absence of an electric field, a charged particle will end up travelling along magnetic field

lines in helical orbits provided there is no other source of kinetic energy present for the particle. According to Maxwell's laws, the non-existence of magnetic monopoles would mean that the magnetic field lines always create a closed loop, rendering the particle travelling along the field line trapped. This very principle is the underlying base of a magnetic mirror- a particle confinement scheme used in early days of magnetic confinement fusion research.

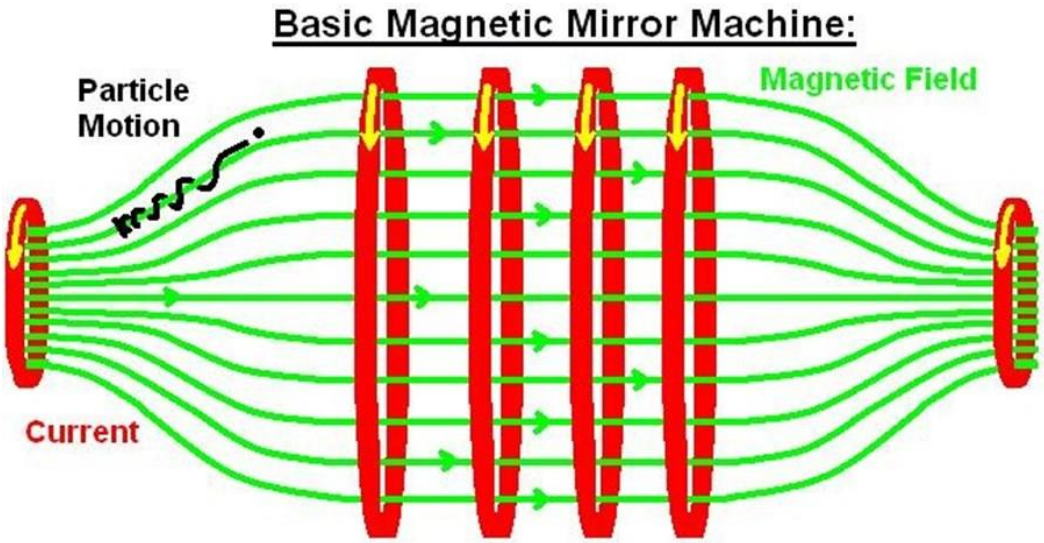

Figure 1.4: Conceptual representation of a magnetic mirror configuration [6]

As shown in figure 1.4, a particle travelling along the field line reaches the end of the mirror, where a lot of magnetic field lines are converging, raising the magnitude of magnetic field high enough to make the particle change the direction of its motion by π radians. In layman terms, the convergence of magnetic field lines near coil 1 and coil 2 in the figure create a mirror where a travelling particle is "reflected" by the sudden increase in the magnitude of the magnetic field. Such a basic magnetic mirror configuration can confine the particles, but the confinement efficiency is not large enough to use it for a reactor scale fusion device. It, however, provided a strong head start to the search of a better confinement scheme. Several different schemes like Z pinch, Θ pinch etc. were presented and experimented with before Lyman Spitzer, came up with a configuration named **Stellarator** in 1951, based on the idea of confining the particles in a toroidal tube and wrapping the tube with solenoidal coils to produce magnetic fields (see figure 1.5). The essence of the configuration lies in the "**rotational transform**" where a magnetic field line would come back to its original starting position after having intersected several cross-sectional planes in

points which rotate about the magnetic axis successively. Depending on the choice of method for generation of the rotational transform, different stellarator configuration exists, namely Torsatron, Heliotron, Modular, Heliac and Helias. Ever since its inception, the stellarator configuration has gone through many different upgrades. However, in its early days, lack of necessary particle confinement capability caused a loss of interest in stellarator research. Still, USA, Germany, Japan, Spain and Australia have kept investing in stellarator research due to a big advantage it provides over its contemporary configuration- the ability of continuous steady state operation without the need of a constant plasma current generation- and hence, without the need of a central solenoid- making it a viable option for a reactor scale configuration.

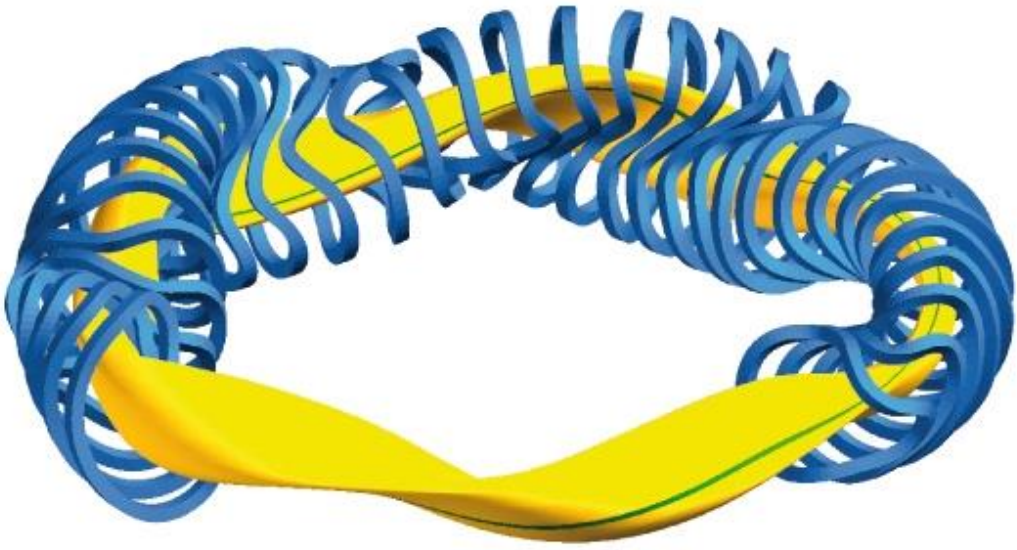

Figure 1.5: Schematic diagram of the Wendelstein 7-X in IPP Greifswald [7]

Parallelly, in USSR, a different configuration was proposed by Igor Tamm and Andrei Sakharov based on a letter written by Oleg Lavrentiev. The core concept was somewhat similar to the one of stellarators in the sense that curved magnetic field lines around a torus can provide a better particle confinement in a stable plasma equilibrium. Igor Golovin coined the term TOKAMAK- an acronym for a Russian phrase meaning Toroidal Chamber with Magnetic Coils. Unlike stellarators, tokamaks produce their magnetic field combining toroidal and poloidal magnetic field to obtain the helical field configuration as shown in figure 1.6. The toroidal field is produced using toroidal

field coils linking the torus whereas the poloidal field is produced by the current flowing in the plasma.

Tokamaks perform a very good job at restricting the particle loss at the walls of the vacuum vessel, something that initial configurations like z-pinch and early stellarators could not. The crucial bit is to not only make the magnetic field lines go around the torus but also make them twist. The relation between twists and orbits is an important parameter for magnetic confinement fusion devices and is termed as the **safety factor q**. Studies have shown that for the values of q>>1, the particle loss is suppressed by order of magnitudes as compared to configurations with q≤1. Some world-renowned tokamaks are Alcator C-MOD and DIII-D in USA, JT-60 in Japan, ASDEX in Germany, Joint European Torus (JET) in UK, WEST in France, EAST in China, KSTAR in Korea, Aditya in India, COMPASS in Czech Republic- and the biggest and most important in the history of magnetic confinement fusion research- ITER; which is still under construction. In the following section, a slightly more detailed account is given about JET since a large amount of work for this thesis was done using JET data.

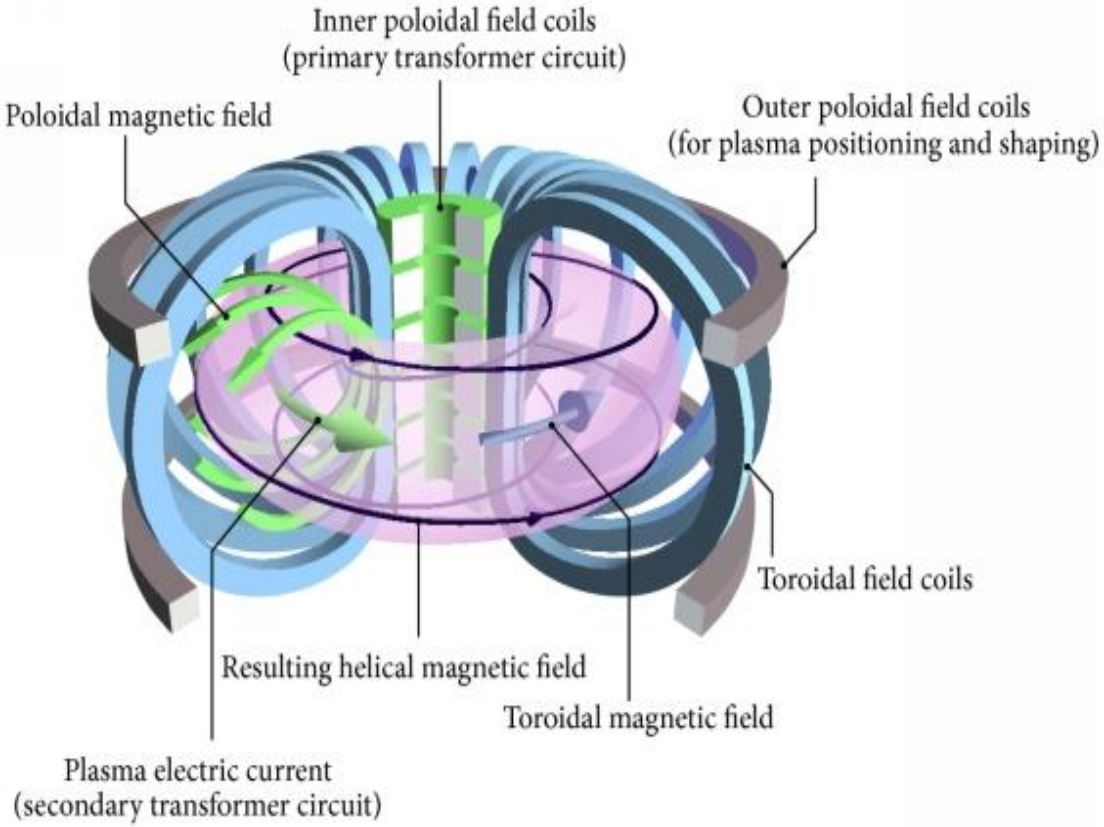

Figure 1.6: Schematic diagram of a TOKAMAK concept [8]

1.3. The Joint European Torus- JET

The JET is the biggest and only tokamak with a capacity to operate with Tritium. It is located at the Culham Centre of Fusion Energy (CCFE), Oxfordshire in United Kingdom. It will not be an exaggeration to say that JET is the European flagship magnetic confinement fusion device. In 2021, JET went through its second successful DT campaign, surpassing its previous records and in the process, yielding a lot of useful knowledge for the upcoming phase of ITER start-up.

JET came into inception in early 1970's, with the design procedure being initiated in 1973 and coming to conclusion in 1975. By the beginning of 1960s, the stellarator research had taken a backseat owing to their inability to suppress particle loss and on the other hand, tokamaks had become frontrunners for the magnetic confinement fusion ideas. Meanwhile in 1957, J. D. Lawson published his research, quoting a very important quantity for determining minimum optimal values of three major parameters: the particle density, the energy confinement time and temperature. The numerical product of these parameters, also known as the *triple product* determines whether a reactor can reach the state of self-sufficiency- the ignition. For the DT reaction, the Lawson criterion is given by [9]:

$$n\tau_E \geq 1.5 \times 10^{20} \frac{s}{m^3}$$

here n is the particle density and τ_E is the energy confinement time, defined as the rate of loss of energy of a system to its surroundings. In case of nuclear fusion, a lot of energy loss is observed especially by the acceleration of electrons, resulting in Bremsstrahlung, radiated in the X-ray regime as well as poor confinement leading to particles escaping the magnetic field and colliding into the vacuum vessel, resulting in energy loss as well as unwanted damage to the vacuum vessel walls. Also, it is important to note that the Lawson criterion sets a minimum limit for ignition and it is not the absolute solution to all the ignition and burning plasma related challenges. Ever since the discovery of the Lawson criterion, the fusion research has been dedicated towards achieving it.

As can be seen from the figure 1.7, from the moment of discovery of the Lawson criterion, two decades of work in tokamak research had yielded not much progress, in fact, there were no DT experiments made under reactor relevant

conditions. This makes JET an ever so important experiment in the quest for betterment of our understanding of the science and challenges of ignition. In context of fusion, ignition is the steady state of a reactor where the plasma is able to heat itself using the fusion products, without requiring any auxiliary heating mechanism, to produce net energy output. The net energy output, in scientific terms, the Q value of a reactor is defined as:

$$Q = \frac{Total\ energy\ output}{Total\ energy\ input}$$

Here, the total energy input is a very important quantity because not only the current necessary to be driven through the central solenoid of a tokamak, but also, the current used for powering the electromagnets to generate high magnetic fields, as well as different types of heating systems are main contributors to the value. So, for an ideal scenario, a reactor upon reaching ignition, should enter a phase called *burning plasma*- where the plasma is able to maintain the heating using the DT fusion reaction, heating by α particles and also, neutrals.

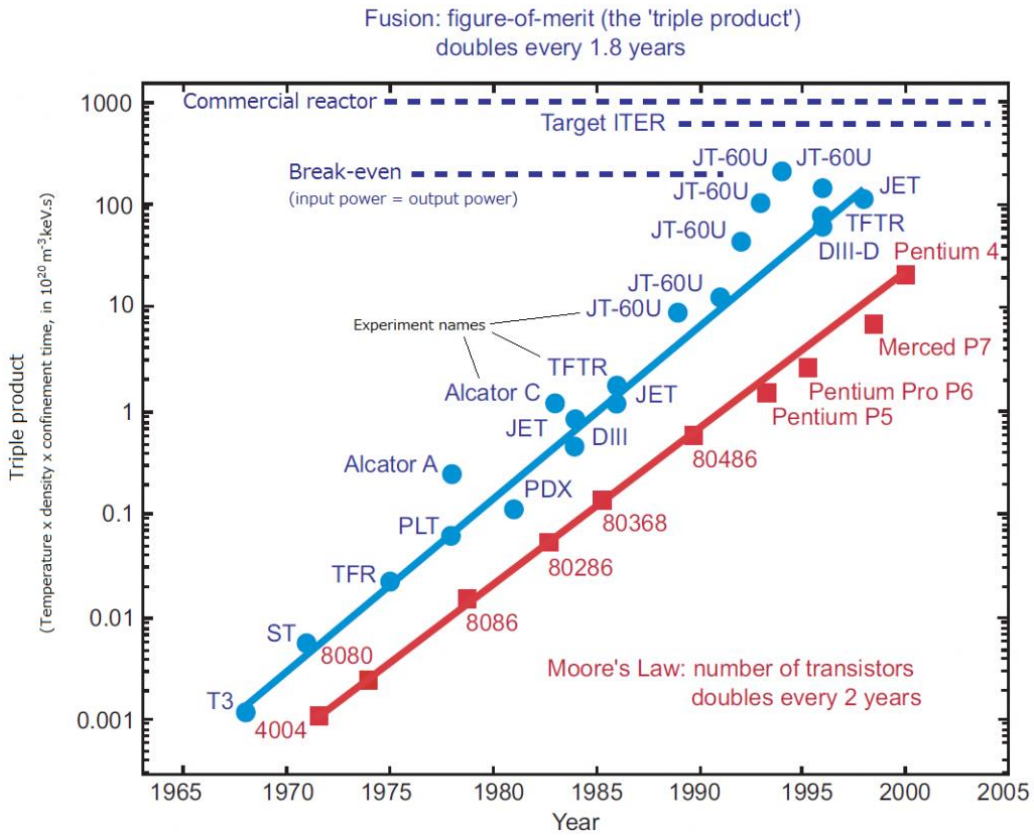

Figure 1.7: Progress in achieving fusion grade machine conditions [10]

JET was designed with the objective "to obtain and study a plasma in conditions and dimensions approaching those needed in a thermonuclear reactor" as per the design team of JET. These conditions included the capacity to be able to make DT plasmas and study α particle heating produced by the DT fusion reaction. Not only that, but the long list of specific objectives also included study of different heating methods, plasma wall interaction, train personnel for operation of reactor with emphasis on plasma start-up, shaping and termination. The initial parameters of JET in the draft design are given in table 1.1.

Table 1.1 does not include the parameters of extended performance scenario, which would raise the magnetic field up to 3.5 T and plasma current for a D-shaped plasma up to 5 MA. The initial design of JET even included a capacity to use additional heating power of the order of 4-10 MW. The additional heating systems included Neutral Beam Injection (NBI), Radio Frequency (RF) Heating and Adiabatic Compression. The JET vacuum vessel can contain a total plasma volume of the order of 100 m^3.

Parameter	Value
Horizontal plasma minor radius (a)	1.25 m
Vertical plasma minor radius (b)	2.10 m
Plasma major radius (R_0)	2.96 m
Plasma aspect ratio (R_0/a)	2.37
Plasma elongation ratio (b/a)	1.68
Flat top pulse length	20 s
Total magnetic field at plasma centre	2.77 T
Plasma current for a D-shape plasma	3.9 MA

Table 1.1: JET parameters from the initial design

The initial goal of JET was to reach Q=1 with DT experiments. After the successful DT campaign in 1991, where JET created record for the highest fusion power production, it was demonstrated that JET can and must be used for learning and understanding ITER operational scenarios. In 2009, it was decided to use JET with ITER like wall (ILW), where the JET Plasma Facing Components (PFC) were upgraded from Carbon Fiber Composite (CFC) to the ones with Tungsten and Beryllium (ILW) in order to simulate ITER experimental scenarios with further precision. JET was designed with a capacity to be operated with both circular and D-shaped plasmas because studies have shown that an elongated plasma cross-section helps improve particle confinement.

Also, the use of divertor can help improve plasma performance with removal of impurities. Hence, in elongated plasmas, a separation boundary is introduced in the magnetic field, termed as separatrix. There is a small zone between the separatrix and PFC, called the Scrape Off Layer (SOL), where a lot of interesting physics occurs. Studies of edge physics for elongated plasmas have benefitted a lot at JET, with different type of divertor configurations being tested.

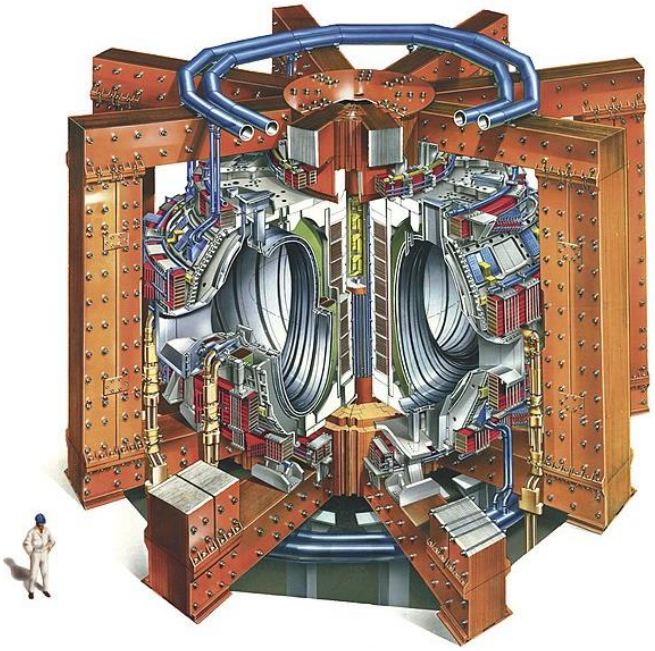

Figure 1.8: JET conceptual design [11]

Just like any other experiments, JET is also equipped with different types of very capable diagnostic systems [12,13,14]. Passive diagnostic systems like radiation detectors for studying all types of detectable radiation emitted by the plasma, particle detectors for detecting neutrons and charge exchange atoms etc. for measuring neutron yield and ion temperature as well as distribution functions alongside field detectors to observe, measure and control changes in electric and magnetic fields were installed initially. For active diagnostic systems, Laser based diagnostics like interferometer and Thomson scattering method have been an integral part of the JET diagnostic set-up. Over the years, many upgrades have been made in the existing ones to improve their time resolution and new diagnostic systems have been installed using novel approaches for better understanding of the JET plasma. Currently, the JET hosts over 100 different diagnostic systems, providing a hawk-eye view into the plasma. Not only is JET enabling the testing of newly developed diagnostics, it also serves as a breeding

ground for new methods and techniques, especially after being chosen to be the ITER dummy for physics and technology testing and benchmarking. A plasma cross section of JET is shown in figure 1.9

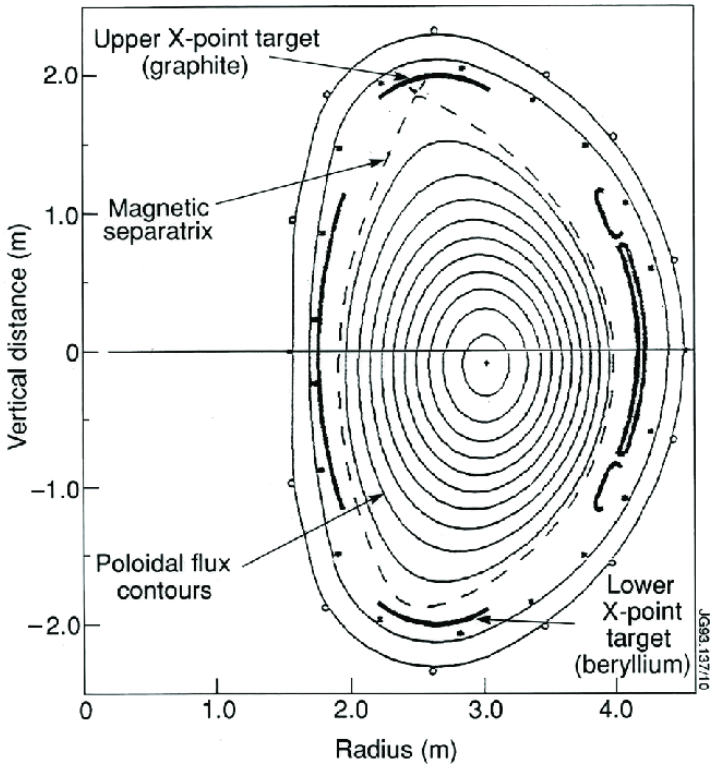

Figure 1.9: JET plasma cross-section [15]

In terms of auxiliary heating systems, JET is equipped with NBI system, where Hydrogen nuclei are accelerated to very high voltages (~80000 volt), only to be converted back to atoms in a neutralizer chamber before being shot inside the plasma to heat up a concrete region of plasma volume where the neutrals deposit the energy into the plasma by means of collisions with plasma particles. The key part of NBI heating lies in the fact that charge neutral particles are not affected by electromagnetic fields. So, for maximum efficiency, the neutralization rate in the neutralization chamber must be high enough for maximum penetration of the neutral beam. The NBI system also has the capability to use Deuterium atoms at energies up to 1.6 MV. At the commissioning of JET, a total of 10 MW worth of neutral beam power was available [16]. With several upgrades, the NBI power capacity at JET stands at a maximum of 25 MW today. Additional 15 MW of auxiliary heating power was supplied by the RF heating system, which worked on the principle of energy resonance. Lower Hybrid Resonance Frequency of the ionic oscillations at ~1 GHz and Ion Cyclotron

Resonance Heating (ICRH) in the range of 5-50 MHz was available during the commissioning of JET. Over the course of time, the capacity of the ICRH system has been fine-tuned further with higher power and precise frequency for heating depending upon the species to be heated. A total of 35 MW of additional heating power is now at disposal via ICRH at JET. The lower hybrid resonance heating system has also been upgraded and is now operating at the frequency ~3.7 GHz with a power capability of 15 MW.

In an experimental facility as large as JET, it is very important to have a streamlined control and data acquisition as well as storage system. With millisecond level precision required for the smooth conduct of a singular discharge, automated systems have been deployed as and where possible. A single JET discharge results in huge amounts of data- only diagnostics data amounting to ~60 GB and most of it is raw data, which needs further processing. Specialized computer-based data analysis tools have been developed for fast data processing. Dedicated data validation is done with critical scientific inputs and minimum machine usage to guarantee that the data available to the scientific community is checked for basic errors.

Apart from error free data, another salient feature of JET is the capability of instantaneous reaction to occurrence of unexpected scenarios during a discharge- scientifically termed as exceptions. A dedicated infrastructure is set-up at JET for real time exception handling and is called Real Time Protection Sequencer (RTPS). In order to alert the RTPS of necessary action, a real time data processing framework was successfully deployed in JET in 2018. The framework is called Plasma Event Triggering for Alarms (PETRA) and it holds machine protection and experimental schemes. The main objective of PETRA is to provide platform for various existing and novel methods which involve real time processing of JET data for controlling the trajectory of a discharge. It is quite possible that during an experimental discharge, a certain system responsible for the smooth execution of discharge as planned may run into a fault or the plasma evolution does not correspond to the forecast made prior to the discharge. In such a case, to avoid damage to the vacuum vessel or to avoid waste of resources in case of failed discharges, it is important to either drive the discharge towards a safe termination or force shut down the systems for failed discharges to save resources. PETRA provides the capacity for both, making it an important part of discharge execution as well as device protection system. PETRA is robust

enough to be able to maintain a processing cycle under the hard limit of 2 ms, guaranteeing the use of highest resolution of available data in real time [17]. Not only processing, PETRA is equipped with the capacity of storing all data necessary for analysis of PETRA response during a discharge and further analysis. The work presented in this thesis is a result of PETRA's operational capability and will be referred to time and again during the course of the document.

An important aspect of JET, often not talked about much is the remote handling capacity of radioactive components. JET boasts of housing a robotic arm which is often used for installation and extraction of vacuum vessel components and comes in very handy especially after DT experimental campaigns. All these features and facilities make JET the obvious and most suitable candidate for ITER mockup experiments, which will be briefly introduced in the next section.

1.4. ITER

After successful construction and commissioning of JET, the erstwhile plans and ideas for a joint international fusion project got revived. The roots of ITER though, can be attributed to the International Tokamak Reactor (INTOR) workshop organized by the International Atomic Energy Agency (IAEA) in the year 1978 [18]. In the following decade, efforts from fusion enthusiasts across the globe to study and assess the possibility of a tokamak for fusion energy production were exponentially increased. The Geneva summit in 1985, where Ronald Reagan and Mikhail Gorbachev agreed for a combined effort to harness fusion energy marked an important political milestone after the de-classification of initial tokamak results from the USSR in 1960s. Interest from European Atomic Energy Community (EURATOM) and Japan to join the efforts was welcomed and in 1988, the conceptual design of ITER began with four main parties namely EURATOM, Japan, USSR and USA. The final ITER design was approved in 2001 and by 2005, China, Korea and India had decided to join forces in the project. The same year, the member parties agreed to select the site proposed by the European Union in southern France, a village near Aix-en-Provence. In November 2006, the official ITER agreement was signed by officials from member parties and ITER Organization came to establishment in October

2007 and construction phase began. As of today, the assembly hall is ready and the work to veld the vacuum vessel has been initiated.

As per the official website, ITER is designed to produce 500 MW of net fusion power with DT fuel, similar to a medium size power plant. Upon commissioning, it will become world's largest tokamak having a plasma volume of 840 m^3. In table 1.2, key parameters for ITER are listed. The prime objective of ITER is to demonstrate Q=1, which is termed as breakeven. Breakeven is achieved when the net amount of fusion power produced is equal to the total amount of input power. However, Q=1 is the first goal, with the ultimate goal being achievement of Q=10, where injection of 50 MW of power would yield 500 MW of fusion power- thus, demonstrating the reactor scale operational capability of tokamaks and nuclear fusion in general.

Parameter	Value
Major radius (R)	6.2 m
Minor radius (a)	2 m
Toroidal field at R (B_T)	5.3 T
Plasma current (I_P)	15 MA
Safety factor (q)	3
Average ion temperature (T_i)	8 keV
Average electron temperature (T_e)	8.8 keV
Average electron density (n_e)	10.1×10^{19} m^{-3}
Fusion power (P_{Fusion})	400 MW
Fusion gain (Q)	10
Pulse length	400 s

Table 1.2: ITER parameters

On the roadmap of commercial fusion power, ITER is a very important milestone because it will put an end to the ever standing stigma and lack of belief in fusion as an environment friendly global energy crisis solution. Once ITER has been experimented with to test different technologies, it will pave the way for the demonstration power plants for all the member countries. Just like ITER is expected to show the world the proof of promise of magnetic confinement fusion, the demonstration power plants will be used as prototypes for commercial fusion power plants with Q going as high as 100. The scientific community is gearing up for first plasmas at ITER in 2025, which would mean that we might see deployment of commercial fusion power plants in later years of 2050s.

Chapter 2 – Thesis Objective

This chapter contains explanation and justification for the origin of the work presented in this document. Starting with principal objective, where we define the foremost reason and requirement to carry out the work, a brief introduction is given to the phenomenon of disruptions as well as the centroid method predictor.

2.1. Principal Objective

The work presented in this thesis drives its motivation from the idea to use nuclear fusion for future commercial energy production in order to meet rising global energy demand.

A broad objective of the research work being carried out across the world in the field of automated disruption prediction is to obtain reliable and fast predictors for future power plant class fusion reactors. Achievement of ignition is costly energetically speaking as well as continuous maintenance of triple product- hence, it is desirable that once a reactor is in the burning plasma phase, the duration of the discharge be as long as physically and technologically possible. Disruptions- as the name suggests, disrupts the continuous operation of a discharge and in many occasions, leads to undesired, rapid, violent termination of the plasma discharge.

An expedient quality in a disruption predictor is the simplicity of physics interpretation of the underlying model as well easy extrapolability for its usage in a different size and scale reactor. Not only that, but a consistent high successful detection rate alongside negligible false alarm rate is also expected accompanied by acceptable warning times. Ideally, large warning times are desired to provide sufficient time for suitable actions to be taken- be it avoidance, where the discharge is operated within the safe operational boundaries and in case of even a smallest departure from safety limits, quick return to the safety limits is executed. If the warning time is not sufficient for avoidance, prevention methods are used to drive the plasma towards a safe termination regime because if not done so, the discharge might end up disrupting. In the worst-case scenario, where the disruption is occurring, mitigation is the only remedy and the discharge is required to be terminated immediately in order to ideally prevent or reduce the harmful effects on the

vacuum vessel. If a disruption is detected falsely and the discharge is terminated in order to safeguard the tokamak, a sizable cost is incurred in terms of resources. It is also important to mention that the predictions need to be made using real time diagnostics data and not simulations because actual data provides a better basis for estimating the plasma state being disruptive or non-disruptive whereas simulations can sometimes mislead due to the usage of approximations or machine rounding errors.

2.2. Introduction to disruptions

Disruption is defined as a rapid loss of plasma confinement, often accompanied by perilous energy deposition in the VV as well as exertion of catastrophic level electromagnetic forces on several different components of a tokamak. Not only does a disruption pose threats to the structural and mechanical components of a tokamak, but it can also cause a reduction in the effective efficiency of energy production and hence, the net Q-value over the lifespan of a tokamak power plant.

When a disruption occurs, the plasma position control is lost and plasma eventually ends up making contact with PFCs, dumping huge amounts of thermal and mechanical energy into the VV. A very high energetic runaway electron beam is also produced during and following a disruption in some cases. This resultant runaway electron beam usually carries a large fraction of the plasma current as well very high energy- all of which is deposited in the PFC, causing tremendous harm and reducing their durability and hence, their lifespan significantly.

Subsequently, the continuity of a tokamak reactor operation is difficult to maintain given that the maintenance and replacement of various PFC components, which have been activated upon constant irradiation of neutron, alpha and several other types of particles as well as radiation, must be done using remote handling and for a reactor class tokamak, the size of these PFCs can make the duration of this task of the order of several days at the least.

Different approaches have been deemed useful to tackle the problem of disruptions. A timely detection should allow for usage of massive gas injection (MGI) to cool down plasma and alleviate the energy dump to the PFC in case of avoidance being out of scope. To compensate for large sideways movement caused by the electromagnetic forces, structural improvements for seismic

activity tolerance are also employed in the construction of the ITER main chamber building.

The key is to be able to detect upcoming disruptions, possibly, with also identifying the type of disruption- by means of an automated system to then, produce system response in accordance with the necessity of each disruption scenario. The task is not easy and there exist a variety of opinions over what is a bare minimum. A detailed account is given in the next chapter where disruptions and type of predictors are discussed in thorough detail.

2.3. Centroid Method for disruption predictions

The centroid method is an attempt to produce a disruption predictor with all the desirable qualities. A linear equation means adaptability feature regardless of the size or scale of a reactor, easy fundamental physics concept provides seamless scientific explanation and usage of few plasma diagnostics signals makes it versatile enough without special requirements of dedicated systems for implementation. The implementation would consist of a 3-phase process as described:

a. Training phase where existing data is used for gathering information about the disruptivity of a discharge, identification, and extraction of useful features to obtain centroids in the parameter space.

b. Testing phase where the centroids derived in the training phase are used to determine the success rates, false alarm rates and warning times. Fulfillment of desired threshold values of those three quantities would mean a successful validation of the physics model used in training.

c. Deployment phase where the centroid method predictor is installed in the RTN of an experimental device, functioning alongside several other critical systems for successful operation of the device.

Chapter 3 - Disruption Predictors

This chapter encompasses a detailed discussion about the progress made in the field of disruption predictors. A brief overview of disruptions in JET and ITER as well as disruption handling is given to introduce the need of disruption predictors. Different approaches and methods used are given an overview.

3.1. Disruptions in JET and ITER

For maximum exploitation of a tokamak plasma, it is essential to be able to control the evolution of the plasma with absolute planning and certainty. Over the years, constant research and experience has produced commendable understanding of fusion grade plasmas, which in turn, has resulted in scientists being easily able to drive the discharge in desired direction. It is, however, not the case for every single discharge since the extreme high temperatures, densities and electromagnetic fields create a rather hostile environment for plasma particles, resulting in plethora of phenomena that can perturb the planned course of evolution of a discharge. Up until 1982, only one confinement mode was known in tokamak plasmas but Wagner et al [19] showed that if additional neutral heating is applied upon reaching a certain density threshold during a discharge, a sudden improvement in plasma performance can be achieved. This enhancement in performance was found to be a consequence of simultaneous improvement of transport of energy and momentum transfer of particles and impurities. Later, H-mode transition was demonstrated using ICRH as well [20]. Even though the appearance of H-mode was a surprise, the physics of its occurrence was understood very soon as can be seen through H-mode demonstration in different devices like PDX [21], DIII-D [22] and JET [23]. Soon, it was understood that to achieve best fusion power output, it is necessary to use the H-mode and the highest fusion power achieved before ITER design was in fact in the H-mode [24] to influence ITER design [25].

Long before the discovery of H-mode, there were several unwanted plasma phenomena already detected and being understood. This class of phenomena is termed as Magneto Hydro Dynamic (MHD)-phenomena, deriving the name from the theory applied to understand flows in plasma. MHD approach combines electron and ion fluid model to yield a single fluid approach for the

description of the plasma as a fluid. Depending on the plasma configurations, one can use ideal MHD approach or resistive MHD approach for describing the confined plasma. In presence of perturbations, the MHD equilibrium is disturbed, leading the total plasma potential energy to change. If the energy change caused by the perturbation is positive, then it is understood that the plasma is stable with respect to the perturbation whereas in the case of a negative energy change, plasma becomes unstable. The change in plasma energy has several contributors and majority of them are mostly stabilizing. However, there are contributions which can be stabilizing or destabilizing. One such possibly destabilizing term is dependent on the pressure gradient and the instabilities rising through such a contribution are called "pressure-driven" instabilities. The other term causing loss of equilibrium is based on the parallel component of the current and hence, are termed as "current-driven" instabilities. There is a third class of instabilities, named as "particle-driven" instabilities and are based on the fact that some MHD instabilities can interact directly with the plasma particles.

Furthermore, depending on the nature of the instability, we could have "ideal" or "resistive" instabilities which either preserve or modify the flux surface boundaries in plasma. From a point of view of the plasma-vacuum interface, the MHD instabilities can be classified as "internal" or "external" depending on considerations whether the boundary between plasma and its surrounding is fixed or can be moved. Furthermore, another classification can be added based on the time evolution of such instabilities, namely "linear" and "non-linear" where in linear instability, there are possible ways to stabilize the perturbation but in case of a non-linear instability, only the saturation of mode saturation is reached and no free energy is available for dissipation. In a nutshell, it is not incorrect to say that classification of MHD instabilities is an imprecise task because in many cases, the destabilizing mechanisms are a mix of different origin and not a single prevalent one. Sometimes the origin of the instability is unknown and it is rather identified by a phenomenological name. A brief overview of some MHD instabilities is given.

1. Kink Instability: Rational flux surfaces are susceptible to intense effects of toroidal current ($q = \frac{m}{n}$). Low poloidal mode number (m) modes can be destabilized by the plasma current and the instabilities rising from such perturbations are named kink instabilities. They can be of both internal and external type. The internal kink modes result in sawtooth oscillations, typically

observed in the center of the plasma column. The detection of these sawtooth oscillations is made by soft X-ray (SXR) diagnostics.

2. Tearing Mode Instability (TM): Adding finite resistivity to the basic kink modes' theory results in the appearance of tearing modes. Term "tearing" is used because the structure of the flux surface prior to the appearance of perturbation is torn apart and the modification of flux surface results in reconnection of magnetic field lines- giving birth to "magnetic islands" in the vicinity of the rational surfaces. These tearing modes present a strong limitation on the maximum energy of a tokamak plasma. For high performance fusion plasmas, often the appearance of Neoclassical Tearing Modes (NTMs) is a great cause of concern because the slowing down of its rotation speed leads to a sudden and catastrophic loss of plasma in 100s of microseconds- a phenomenon called **Disruption**. In the following subsections, a detailed account is given of the causes and repercussions of the disruptions.

3. Ballooning Instability: The ballooning instability originates from the drifts the plasma particles experience in curved magnetic field lines. The pressure gradient in unfavorable magnetic curvature due to the anisotropy introduced by the magnetic field lines causes the plasma to bulge out, causing oscillations with a long wavelength along the field lines but comparatively much smaller in the direction perpendicular to the magnetic field.

4. Edge Localized Modes (ELMs): Studies have shown that a good plasma confinement in reactor class tokamaks will lead to steepened pressure profile at the plasma edge. If the value of pressure gradient exceeds a critical value, a certain type of instability is produced, featuring a periodic fast collapse of the edge pressure. This edge pressure drop is accompanied by a sudden loss of confinement, which, consequently, leads to the particle and heat dump on PFCs. These periodic heat and particle release on PFCs reduce their lifetime significantly and hence, in the past two decades, dedicated efforts have been made to understand the cause, types and ways to control ELMs since ELMs are bound to appear in the H-mode operation of tokamaks and the fact that H-mode is so far the best plasma performance mode, it is given that all the future reactors, including ITER will operate in H-mode.

ELMs, as the name suggests, appear in the plasma edge and even though their origin is well understood, so far there has been not one single individual cause identified for their destabilization. Characteristics like magnetic

fluctuations, shorter growth time scales as well as eerie vicinity to the MHD stability limits of a plasma at the occurrence point at the onset establish ELMs to be an MHD phenomenon (or a combination of several). However, different size and shape of plasmas may lead to different types of ELM drives, which makes the classification of ELMs a very important task. Different approaches have been used over the course of time to distinguish between various types of ELMs. Theoretical, experimental and analytical research done during the past 3 decades has brought a general understanding about three different types of ideal MHD instabilities at the edge transport barrier namely **Localized Peeling Modes**, **Edge Ballooning Modes** and **Coupled Peeling-Ballooning Modes.**

While considering the plasma contact with the vacuum vessel walls, one needs to utilize the "resistive" MHD model. In this consideration, the kink instability is modified and termed as **Resistive Wall Mode** instability which is characterized by its comparatively slower growth rate with respect to the ideal MHD instability.

Above mentioned and many other instabilities alone or in form of a combination, can hamper the equilibrium of plasma, resulting in a **Disruption**. Since the fundamental theme of this thesis revolves around disruptions, it is only fair to have a closer look at the phenomenology of disruptions. For obtaining maximum energy output from a tokamak, it is essential to be able to operate it in a disruption free steady state condition for longer periods. However, there are multiple constraints that reduce the steady state operational regime of a tokamak. Maximum values of plasma current, particle density and normalized plasma pressure (also known as plasma β) are the main constraints. The limits are set up as follows:

i. The plasma edge safety factor $q_{95} \geq \sim 2$ sets up the current limit because q is defined as

$$q \approx \frac{rB_{\varphi}}{RB_{\theta}}$$

with B_{θ} being the poloidal magnetic field and B_{φ} being the toroidal magnetic field, r is the distance of point of interest where we want to evaluate the safe factor from plasma core and R the major plasma radius. The poloidal magnetic field is produced using the toroidal plasma current, which means that for plasma currents higher than a certain values, the poloidal magnetic field is too high to bring the edge safety factor below 2, causing the plasma to be

magnetohydrodynamically unstable at the last closed flux surface. Also, the notion of q_{95} has been used in divertor configuration tokamaks to emphasize that it is convenient to use the q value at a flux surface that encloses 95% of the poloidal flux, just inside the separatrix since the value of q approaches infinity at the separatrix.

ii. The density limit is set by the fact that the plasma temperature varies from the core to the edge of the plasma cross-section and the plasma at the edge, specifically near the separatrix is comparatively cold and radiative. In case of very high densities, this cold and radiative plasma starts expanding inwards towards core from the separatrix and using the closed field lines of the core plasma, a poloidal symmetrization of the radiating layer is obtained quickly, which resulting in the plasma being resting on a radiation gas mantle instead of a solid limiter [26]. In theory, such a configuration can be stable but more often than not, these "poloidally detached" plasmas are unstable and lead to a rapid, uncontrolled contraction of the temperature profile, eventually perturbing the MHD stability of the plasma. It is a phenomenological limit and theoretical investigation for a complete physics based understanding of the origin of the density limit is still on. Numerically,

$$n_G = \frac{I_P}{\pi a^2}$$

Where I_P is the plasma current, a is the minor radius and n_G is the line averaged density.

iii. The pressure limit originates form the study made by Troyon, where the hard limit was set for MHD stability against all types of ideal MHD modes. In the original study, Troyon and his coworkers performed an optimization procedure by means of variation of plasma cross section, plasma current and plasma pressure profiles for an expansive set of realistic conditions. It is defined using the plasma beta, a parameter often utilized for plasma performance description.

$$\beta = \frac{\langle p \rangle}{B^2/2\mu_0}$$

where $\langle p \rangle$ is the mean plasma pressure, B is the total field strength. The Troyon factor, also known as the normalized beta is given by,

$$\beta_N = \beta \frac{aB_T}{I_P}$$

with B_T being the toroidal magnetic field, a is the minor radius and I_P is the plasma current.

The onset of a disruption can be further divided in different segments, starting from an instability appearance, going through a precursor phase and terminating with either a current quench (CQ) followed by a thermal quench (TQ) and vice versa. In many cases, thermal quench does not mark the end of a disruption since a rapid current quench may produce very high electric fields in the plasma, leading to the generation of runaway electrons. More details about phases of disruption evolution can be found in Schuller et al. [27].

Occurrence of instabilities in fusion plasma is a very common phenomenon owing to the fact that there can be many actuators. Also, sometimes due to operational or mechanical errors, plasma equilibrium can be lost, which eventually results in a breeding ground for a disruption. It is important to mention though, that constant monitoring of plasma behavior is now possible and still, sometimes the growth rate of an instability or slightest delay in machine system failure detection is enough for provocation of a disruption. By the time changes in plasma parameters or faults in machine systems are detected by diagnostics and real time plasma control system, the plasma equilibrium worsens and concrete signs of such deterioration are picked up by the monitoring systems and are commonly known in the scientific community as **precursors**. These precursors are used in design of disruption predictors with focus being put on prompt detection of precursors. Such disruption predictors play a vital part in disruption mitigation and amelioration and hence have been one of the most sought-after tools for the future reactor grade tokamaks.

Rapid growth of MHD instabilities and detection of precursors is followed by a sudden collapse of favorable plasma profiles, flattening of radial current profile and core temperature drop are a couple of indicators of a collapsing plasma. This kind of collapse leads to the plasma dumping a significant portion of its thermal energy on the VV wall in a time span of ~ 100 µs. This phase is known as **thermal quench**. The thermal quench cools down the plasma, and in process, increases plasma resistivity and as a consequence, the plasma current decays rapidly, too. For tokamaks with a vertically elongated plasma cross section, thermal quench may also provoke vertical instability, where the control over vertical plasma position is lost and plasma ends up moving upwards or downwards with respect to the magnetic axis, resulting in what is known as a

Vertical Displacement Event (VDE). This vertical movement of plasma cause the plasma to make contact with the first wall. Typical time scale for current quench and VDE development in medium size tokamaks is of the order of several ms.

3.2. Importance of disruption handling

The reason behind disruptions being given such a detailed attention in MCF research community is the severity of repercussions caused. Thermal quench results in extreme heat loads on First Wall Components (FWC), current quench can cause extremely high electromechanical forces, causing structural damage to the VV and runaway electrons can result in localized surface and substrate damage.

According to Hender [28,29], for a tokamak of linear dimension L, the energy stored in a tokamak plasma rises to the order of L^5 and hence, the energy dissipation at the VV wall caused by a disruption gets to the order of L^3. This would mean that for the case of going from JET to ITER, the disruption wall load can result in an increment of one order of magnitude. The electromagnetic loads produced during disruptions are also dependent on the size of the tokamak alongside the toroidal magnetic field B_Φ. The electromagnetic load has a squared dependency on both L and B_Φ ($W_{EM} \sim L I_P B_\Phi$ and furthermore, $I_P \sim L B_\Phi$), leading consequently again to a dependence order of L^3 since B_Φ does not increase linearly with L in tokamaks empirically. To improve the confinement and stability of reactor class tokamaks, the plasma cross-section is chosen to be of **D** shape for a given edge safety factor. This vertical elongation of the plasma cross-section, however, renders the plasma vulnerable to vertical instabilities, which can eventually cause the plasma to move in vertical directions and disrupt regardless. To combat such vertical displacement events, a sturdy control system is required. Sometimes, the operation in close vicinity of plasma stability limits can also result in a disruption.

Several exhaustive studies made on JET over the years have demonstrated the effects of disruptions. According to Hender [29], the minimum current quench (CQ) duration at JET on average has been observed to be of the order of 9.4 ms, resulting in induction of eddy currents capable of causing relative forces of the order of 220 T^2/s. Additionally, the production of runaway electrons can induce an electric field as strong as 38.3 V/m in the plasma, resulting in

exponential avalanche gain and reducing the shutdown time to avoid Be first wall melting to 30 µs. These numbers are only for JET, when extrapolated for ITER and eventual commercial reactor class tokamak using appropriate scaling laws, still return values that are very high for tolerance of materials used in fusion research today.

For preparations of ITER experiments, JET PFCs, which were previously made predominantly of carbon, were replaced by a metallic wall (ILW), comprising of main chamber beryllium (Be) tiles and on the divertor, tiles made from bulk tungsten (W) as well as tungsten coating. The heat loads produced by disruptions are quite capable of melting the first wall tiles of Be at ~20 MJ m^{-2} $s^{-1/2}$ and W at ~50 MJ m^{-2} $s^{-1/2}$ [30]. As per de Vries [31], the Be melt limit can be easily reached for a quench occurring ~ 2.5 ms of 1 MJ thermal energy.

In case of a current quench, the outcome is a strong electromagnetic force on VV caused by either the quench induced eddy currents or the infamous **halo** currents. The eddy currents are induced due to the increase in plasma resistivity and subsequent current decay whereas halo currents are produced when the plasma makes physical contact with the surrounding conductor- in case of a tokamak, the VV. The value of halo current depends on the time plasma takes to make contact with the VV during the CQ phase. If the contact is made very early during the CQ, large amounts of halo currents are generated. This points towards the conclusion that if the growth rate of plasma positional instability can be slowed down, the resultant halo current can be lower. It is observed in JET [31] that the dynamic reaction force produced during the disruption also changes with the change in PFC material. The ILW produces higher reaction forces in the vessel and are explained to be related to the duration of CQ phase and halo time. In the past, forces of strength as high as several tones and sideways roll and swing have been observed. These force damage the structural integrity of the VV mechanical components and reduce their lifetime.

Another detrimental outcome, probably the most directly visible of all possible outcomes, is the generation of runaway electrons. The rapid rate of current quench causes induction of a parallel electric field. This electric field can end up accelerating plasma electrons. If an electron is already moving sufficiently fast, can further benefit from the acceleration of the induced electric field and move even faster, reducing the collision frequency in the process. This reduction

in collision frequency is also reflected in the reduction of friction force and hence, the electron can indefinitely keep gaining kinetic energy, as discovered by Dreicer [32, 33]. In recent years, another theory has been put forward and investigated both theoretically as well as experimentally. According to the new theory [34], if during a collision, the velocity of colliding particles changes considerably, one of the colliding particle is a runaway electron, it can push a thermal electron beyond the runaway threshold while still remaining a runaway electron itself. Such collisions may result in an exponential growth of the runaway electron population, resulting in an avalanche. The only necessary condition for the onset of such a runaway avalanche is the presence of a "seed" population of fast electrons in the plasma. Usually, the kinetic energy of runaways is of the order of tens of MeVs and a beam of such high energy runaways can produce significant damage to the PFCs.

3.3. Disruption predictors

As explained in the previous section, disruption handling is a crucial part of successful tokamak operation. The most important role in disruption handling is played by disruption predictors. In order to be able to carry out mitigation or avoidance action, it is important to predict an impending disruption with sufficient time. As shown by de Vries [35], the improvement in understanding of JET disruptions and introduction of vigorous precautionary protocols in operational scenarios have reduced the yearly averaged number of unintentional disruptions from a low 20% in 1990s to a significantly below 6% in 2000s. The merit was given to the improvements in the technical capabilities of tokamak operation near stability limits.

Complete suppression of disruptions seems impossible until a closed physics understanding encapsulating all the possible causes and repercussions is developed. Even though the root cause of the onset of a disruption is related to physical phenomena for majority cases, there are chances that human error during operation or even machine systems failure may result provoking a disruption. The consequences being extremely severe as discussed in the previous chapter, ITER is aiming for an operational efficiency of less than 1% of total discharges to be disruptive. With a projected operational life span of 15 years and the number of approximate experimental discharges to be of the order of 50000, still the 1% comes out to be large enough for ITER, which is not designed

to withstand disruptions. Extended studies have shown that classification of disruptions based on their severity in terms of machine impact leaves little to no room for disruptions in ITER.

With ever improving understanding, different approaches have been adopted to tackle the incoming disruptions. The ideal scenario being a complete avoidance, where the disruption is detected well in advance so that the operational conditions could be modified in order to cure the root cause and terminate the discharge without any damage. The more practical approach is the one of prevention, due to the lack of existence of predictors which can reliably predict an impending disruption with sufficient warning time where the operators can select a course of action and the vessel control system can execute it (in JET this time is ~ 10 ms). The least desired option is that of mitigation action, which has the objective to minimize the damage caused to the vessel by dissipating the plasma energy before swiftly terminating the discharge, mostly by cooling down the plasma using different methods to achieve minimum energy dump on the VV walls.

In order to prepare for disruption handling, various methods have been used to design disruption predictors. Some methods are based on physical phenomena like detection of radiation peaking or density peaking whereas some methods rely purely on data from past experiments and use machine learning methods deploying artificial neural networks, support vector machines, reinforcement learning etc. Each approach has its pros and cons e.g. a physics based predictor depends only on the availability of reliable diagnostics in order to detect the onset of disruption root cause and no past data is needed but in case of a data based predictor, one only needs vast amount of past experimental data to train a model and once trained, the model can be deployed straightaway into the real time system for disruption prediction. The problem of availability of historical data is not a big issue with the discovery of approximation from scratch method, where a predictor is trained on the go, using data from new experiments and being independent of availability and reliability of substantial amount of historical data. The former approach not only leads to prediction of disruptions but also provides capability to provide a scientific explanation of why a certain prediction was made. For a data based predictor, often the conflict arises from the lack of acceptable physics interpretation behind a prediction. Given this, it is also important to note that machine learning methods not only

provide the capacity of disruption detection, but also, the possibility of classification of the type of disruption. It is worth mentioning that development of such predictors is one of the biggest challenges for fusion research community because it has vast potential of opening new research pathways based on class identified disruption predictors, which can be implemented for catered experimental scenarios in order to improve the fusion power output performance of future reactors and enabling the maximum exploitation of the potential of fusion energy.

The general approach in machine learning for disruption prediction is based on the fact that the task can be simplified to be a binary classification problem where the system only needs to identify the plasma behavior as either disruptive or non-disruptive. There can be different ways to solidify this classification by adding weight systems or voting systems or even a combination of both. Final outcome though, is whether the plasma state under examination is disruptive or not. In the following sections, a summary is provided on different types of models and predictors designed and being used during the thesis.

3.4. Physics Based Detectors

A brief overview about PETRA was given in Ch. 1 and how it performs the tasks related to exception handling in the JET Real Time Network (RTN). PETRA hosts a variety of disruption predictors as well as event detectors since the operational protocols at JET require the usage of real time device protection system. The protection scenario in PETRA works in the following manner: A disruption warning is triggered when threshold for one or multiple predictors is crossed. The predictors are based on several diagnostic signals obtained for observing physical quantities like plasma current, total plasma energy, locked mode amplitude, radiated power and loop voltage signal. These signals carry information about possible existence of commonly known disruption precursors. Event detectors available on PETRA are not always directly related to disruptions but there are several event detectors that can be used for monitoring if plasma is moving towards the disruptive regime. In any case, if there is an event detector alarm, the discharge is driven towards a safe termination in order to protect the device from potential harm by means of a pre-programmed system intervention.

3.4.1.Locked Mode

Mode locking is one of the most used precursor in disruption prediction research. The origin of the term **Locked Mode** lies in the theory of the notoriously infamous Tearing Mode (TM) instability. Since their discovery by Furth et al [36] in 1963, there has been significant advances in understanding of its origins. The fundamental idea behind generation of a tearing mode instability is appearance of a local perturbation in an otherwise stable system. Just like any other perturbation, it can grow under suitable conditions and change the trajectory of natural evolution of the system. In case of a magnetically confined plasma with a finite conductivity, if there exist a magnetic flux surface for which the field-aligned component of the wave vector of a helical perturbation vanishes, tearing mode instability is developed, resulting in the appearance of a magnetic island. However, it was shown by Reiman [37] that existence of such a perturbation is a sufficient but not necessary condition for appearance of a magnetic island and that a plasma boundary distortion can eventually simulate a perturbation. While operating in the vicinity of stability thresholds, a small distortion may suffice for the provocation of tearing modes.

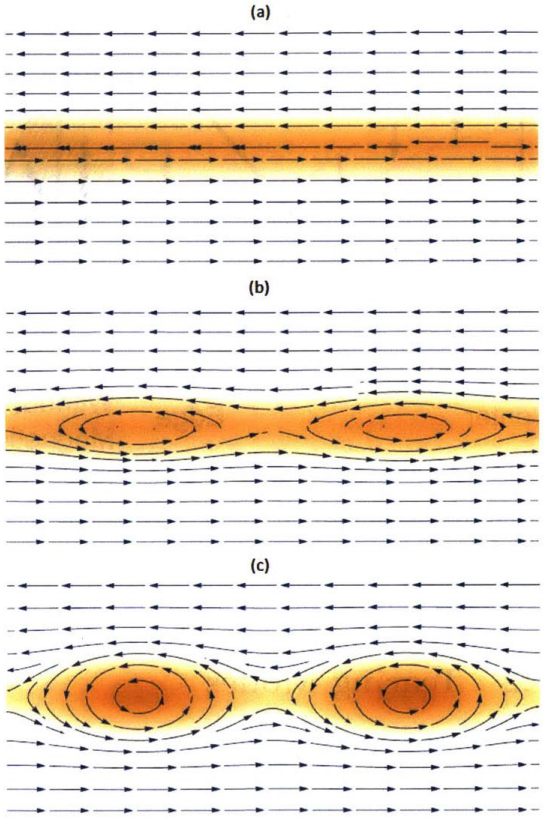

Figure 3.1: Illustration of origins of tearing modes [38]

As can be seen in figure 3.1, a thin current sheet usually much smaller than the system scale is created, which eventually breaks down into its characteristic magnetic island. Field lines in opposite directions produce a current layer as shown in 3.1 (a). These field lines, upon reconnection, end up modifying the magnetic field topology and create alternate, shorter paths for energy transfer between plasma layers (fig. 3.1 (b)). The magnetic island keeps growing until reaching a saturation point, which is also a sign of complete destruction of current sheets in the region where islands have been formed (fig. 3.1 (c)). The instability does not only appear and subside after some time, instead, it starts growing with a non-linear growth phase. In JET and ITER class tokamaks, the plasma is so hot that a tearing mode instability is almost born in a nonlinear regime given that the linear layers are very thin. Tearing modes are a type of macroscopic instability, which affects the entire plasma volume.

When free energy in the current profile overcomes the pressure effects which are contributing to maintaining the stability of the plasma, a "classical" TM appears. To confine plasma particles, even inside a combined toroidal and poloidal magnetic field, the ideal configuration is that a field line never returns to a point it has passed through before. This, however, is an ideal scenario and it is possible that a field line can return to the same point after n toroidal transits as well as m poloidal transits. Magnetic flux surfaces for which this occurs are termed as "rational surface" because the ratio of m to n is a rational number. These rational surfaces are susceptible to appearance and eventual growth of TMs and resultant magnetic islands.

With more experiments, even a NTM has been discovered where the free energy is not derived from the plasma current profile but instead, from the "bootstrap" current profile. Bootstrap current is a self-generated current, originating in presence of a pressure gradient and benefitting from collisional momentum transfer from the trapped particles to the passing particles, amplifying the plasma current and eventually helping with the creation of poloidal magnetic field. Deficit of bootstrap current at a rational surface and the resultant magnetic island reduces pressure profile by means of providing shorter paths for particle flow via magnetic reconnection and leads to further reduction of the bootstrap current on that rational surface- evidently reinforcing the initial perturbation.

The immediate effect of tearing modes is degradation of plasma confinement by means of flattening of pressure and temperature profiles. It also restricts the highest achievable β value and hence, contributes towards the β limit. The shortened path provided by a magnetic island allows for rapid heat diffusion radially. In addition, the tearing mode itself starts rotating with the plasma. This mode rotation imposes a radial magnetic field fluctuation at the VV wall which is resistive and hence, results in induction of eddy currents in the wall which lead to a new magnetic field that exerts additional force on the plasma rotation.

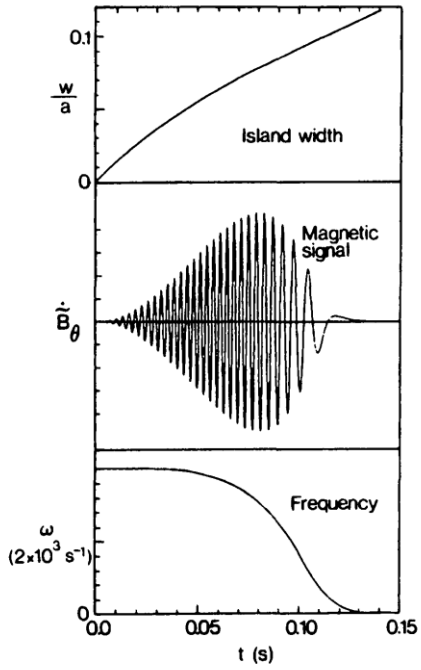

Fig 3.2: Starting from a high frequency and finite island width as well as rotation frequency, the magnetic field perturbation grows and after reaching a maximum value, slows down [39]

In general, when MHD modes grow in amplitudes, their rotation frequency reduces, especially in tokamaks (fig 3.2). For tearing modes, even the associated magnetic islands grow, generating magnetic field perturbations ($\mathbf{B}_{\text{pert}}$) outside the plasma and are observed to be rotating with a characteristic frequency of 1-10 kHz. This rotation is seen as an oscillatory perturbation by the external conductor (VV wall) and the resultant induced electric fields give rise to fluctuating currents ($\mathbf{j}_{\text{pert}}$). The simultaneous presence of $\mathbf{B}_{\text{pert}}$ and $\mathbf{j}_{\text{pert}}$ gives rise to $\mathbf{j}_{\text{pert}} \times \mathbf{B}_{\text{pert}}$ forces in the conductor. Similar forces are induced in the plasma which culminates in a momentum transfer from plasma to conductor, eventually slowing down the plasma rotation- measurable in form of a reduction in rotation frequency. The slowing down of rotation translates into an increased penetration of perturbation fields into the conductor, amplifying the rate of momentum

transfer from the plasma to the conductor. Upon reaching a certain value, the magnetic islands come to rest- causing them to "lock" on the conductor. Sometimes, after locking, the magnetic islands can still grow in amplitude, reaching a saturation value at zero frequency, whereas in some cases, the reduction rate of rotation frequency is low enough to provide enough time for the islands to saturate even before mode locking. In either scenario, the cause of mode locking is understood be of the form of a magnetic viscous drag in the external conductor. A detailed mathematical and analytical account is given by Nave [39], La Haye [40] and several other authors since mode locking is a recurring precursor to many disruptions in JET and other tokamaks like DIII-D, ASDEX, JT-60 [41, 42, 43].

As is normally the case with any perturbation leading to perilous instabilities, the non-linear growth plays a key role in the time to locking for a given mode. Also crucial are the factors like initial seed island width, type of plasma rotation and even the chunk of plasma mass involved in the momentum exchange. These factors do not affect the physics of the phenomenon but can alter the frequency evolution and time it takes for the mode to lock. The conducting VV walls do play a role in the growth of the instability even though it might seem counter-intuitive at high frequencies but as the frequency is reduced, the growth rate of the mode accelerates, which in turn, reduces further the frequency- hence creating a self-sustained drive for instability growth. The island growth remains independent of the fact that the vessel wall can be conducting.

The amplitude of locked mode is measured in JET in real time and is used to set-up the protection scenario in PETRA. The default protection scenario uses the locked mode amplitude signal as well as the locked mode amplitude normalized to plasma current for raising mitigation alarm. The condition for triggering an event alarm with only the locked mode amplitude signal is |ML| > 2 mT whereas the condition for locked mode normalized to plasma current is $\left|\frac{ML}{I_P}\right|$> 400 pT/A for 20 ms continuously. Several different predictors have been designed based on the locked mode amplitude signal because mode locking is one of the most common and most occurring disruption precursor. Apart from the topic of this thesis, works done by Sias [44], Ferreira [45] etc. are some examples of previous attempts to maximize the use of mode locking for disruption prediction.

3.4.2.Plasma Current

The plasma current is essential for a tokamak since it is used to generate the poloidal magnetic field. Any sudden change in plasma current is reflected straightaway in the magnetic field strength and eventually, in the plasma confinement configuration. In the PETRA protection scenario, the time derivative of plasma current over 2 ms (SHRTDIDT) and 16 ms (LONGDIDT) is used to detect any sudden changes in the plasma current. The thresholds for SHRTDIDT and LONGDIDT are 50 MA/s and 7 MA/s respectively.

3.4.3.Restraint Ring Loop Voltage

The restraint loop voltage detector detects magnetic fluctuations which might be caused due to MHD activities or change in the plasma current. As discussed in the thesis so far, in many cases, MHD activity is a principal instigator of the chain of events that culminate in a disruption. Hence, it is important to keep an eye on it. In the PETRA protection scenario, the combined loop voltage and combined loop voltage normalized to plasma current is used for detecting upcoming disruptions. The threshold values are 500 V^2 and 50 pV^2/A^2 for activation of assigned machine intervention response.

3.4.4.Radiated Energy Fraction

Fundamental basis of this kind of event detector lies in the acknowledgement of the fact that if plasma is not dissipating certain amount of heat via radiation, which means that it is depositing the energy directly onto the PFCs, which is highly not desirable for obvious reasons. For starters, all this additional heat-load can damage the PFC over time and lead to their erosion and even sputtering, causing significant loss of plasma purity and once impurities enter plasma, the contaminated plasma performance is degraded noticeably. Also, PFCs for ITER as planned to be made of tungsten and the high Z impurities radiate more power, causing excessive energy loss and lowering the Q value. In JET, the PETRA experimental scenario allows the user to set up the machine intervention in two different cases. If the ratio of radiated energy to input energy is less than a threshold defined by the scientist in charge of the experiment, pre-defined action is taken or it could even be set in terms of a minimum length of time for which the ratio is continuously lesser than the defined threshold. The

values of radiated energy and total input energy are calculated using real time data.

3.4.5.Radiated Power

Another way to ascertain that the plasma is in a quiescent state is to monitor the power radiated by it. In JET, diagnostics is set up to observe both core and edge power radiation and it is aptly used for determining whether plasma is approaching an undesired energy state or not. It is done via calculating the ratio of core and edge radiated power and comparing it to a threshold value and minimum duration of time for which it remains continuously above the threshold. These values can be set for the given series of experiments and provide flexibility as well as protection. The threshold value for both core and edge radiated power above which the detector is activated is set by default at 8 kW/m^2.

3.4.6.Beryllium Melting Detector

Ever since the decision to use JET for ITER preparation has been made, many changes to JET have been introduced in order to be able to closely simulate ITER conditions in terms of plasma environment. One such change was the upgrade of JET first wall components from carbon material to ILW material which mainly uses beryllium and tungsten. The combination of Be and W is chosen taking into consideration various ways in which it can affect the plasma performance. Still, operating the device on limits might sometime lead to the plasma crossing the operational safe regime, which could result in overheating of ILW PFCs. This overheating could provoke melting of Be tiles, introducing impurity into the plasma as well as compromising the integrity of VV, making the diagnostics placed around the melted area directly vulnerable to be affected by the plasma. In order to detect such occurrences and protect the PFCs as well as other machine components, a melting detector is installed in JET. The detector is switched on as soon as total RF or NBI power goes past 100 kW and it raises an alarm if beryllium is detected for more than 100 ms.

All the above mentioned predictors are based on the current understanding of the physics of disruptions and also, known precursors. Constant research and technological improvements keep adding novel physics and hence, methods that can be used for designing more physics based predictors but as long

as there are unknown variables in the theory of disruptions, these predictors will only be able to partially identify impending disruptions and that too, without much anticipation since they rely on the processing and interpretation of real data. Also worth highlighting is the fact that all the above mentioned detectors have a set threshold value for each discharge and hence, are sometimes susceptible to either falsely signaling a safe plasma behavior as dangerous or in some cases, entirely missing an upcoming disruption. Both these scenarios are counter-productive for a future commercial reactor class tokamak since the ignition is energetically expensive so one cannot keep switching on and off the tokamak on accounts of false alarms but one can also not afford to have a massive disruption which could damage not only the PFCs but also, the structural integrity of the mechanical housing of the reactor. Hence, an alternative approach has been used lately, reliant on the data obtained using the diagnostics. However, the combination of data results in a model too complicated to explain entirely via physics. In the next section, we will have a quick overview of the working principles of such detectors and also, some examples.

3.5. Data Based Detectors

The continuous technological improvement has introduced many new ways to understand fusion plasmas. Better time resolution due to improved processing speeds, extremely high image resolution at very fast frame-rates on cameras etc. have not only provided us with a better "view" of the plasma but also, the data generated by them is more reliable and contain more information. Past couple decades have seen the rise of machine learning methods in every science disciplines. Machine learning methods rely strongly on availability of historical data to derive models based on data which can be used for forecasting future occurrences of several events in either probabilistic or deterministic manner depending on the method being used. Starting from early 2000s, several disruption predictors using data based methods have been developed and a brief account of some of those follows.

- Cannas et al. have published various articles [46, 47, 48, 49] using different machine learning methods for disruption prediction at JET. Starting from a simple state classifier between disruptive and non-disruptive based on an artificial neural network (ANN). The results from such classification are presented by means of Self Organizing Maps (SOM). Smaller database lead to

a rather modest success rate ~70% and as discussed previously, it is not sufficient. Usage of a different method for learning, namely the non-linear generative topographic map manifold learning was used in [49] to attempt to determine disruption type (e.g. density limit disruption, β limit disruption etc.).

- ASDEX Upgrade also served as a testing ground for several ANN based disruption predictors. Pautasso et al. [50] achieved 85% success rate with a slightly bigger database than that used by Cannas et al. during their studies on JET. Morabito et al. [51] used fuzzy ANN approach to reach success rates as high as 95%. These are all, a posteriori studies and hence, to benchmark the performance of such systems, a simulated real time network test was carried out in 2002 and as communicated by Pautasso et al. [52], a success rate of 79% with 1% of false alarm rate is reported. Cannas et al. [53] also developed a novel predictor for ASDEX Upgrade where dependency on the reproducibility of discharge condition is observed regardless of promising results.
- DIII-D can be termed as a pioneer in ANN usage for disruption prediction. As early as in 1997, Wroblewski [54] attempted to develop a predictor for detecting β limit disruptions. The goal was to obtain a threshold value for alarm triggering and as commented while discussing JET and ASDEX, lack of sufficiently large database was reflected in terms of high rate of false detection, reaching ~20% while obtaining 90% success rates.
- JT-60U was also used for ANN training efficiency check by Yoshino et al. [55]. Having trained the predictor using 12 disruptive and 6 non-disruptive discharges, it was put to test against 300 disruptive and 1008 non-disruptive discharges. A success rate better than 85% was obtained with an average warning time of 50 ms before disruptions. In a work done in 2005 [56], a hybrid trained network was put to test where previously trained disruption predictor was fitted to a new network trained only using non-disruptive discharges, which obtained success rates in excess of 75% for β limit disruption prediction.
- With passing time and improvement in understanding of such predictors, an inter-machine study was made between JET and ASDEX Upgrade by Windsor [57] where a combined database of 185 disruptive discharges (89 from ASEDX Upgrade and 96 from JET) was used. The ANN predictor was trained using JET data and was tested using ASDEX Upgrade data and vice versa to check flexibility and global extrapolation capacity of it. The results were encouraging with success rates $> 65\%$ for both the training and testing scenarios. This study

was a landmark in its own because it opened a new horizon for similar inter-machine studies. Rea et al. [58, 59] have tried using random forest method for disruption prediction during their inter-machine studies between DIII-D and ALCATOR C-Mod.

- Murari [60] came up with a method using fuzzy logic based on Classification And Regression Trees (CART). The unique advantage CART has is that it keeps partitioning the input space in each iteration keeping the nodes of the tree as independent as possible from other nodes.
- Deep learning Artificial Intelligence (AI) broke into limelight with beating the human world champion in the videogame GO [61]. Later on, a similar AI engine for chess also revolutionized how it was played. Hence, it was only natural that deep learning based AI was developed for disruption prediction [62] and a cross device architecture based on deep learning was also reported by Zhu et al. [63].
- Jesús Vega has been one of the pioneering names when it comes to usage of data driven methods for disruption prediction. Starting from data mining techniques for retrieval of similar waveforms in massive fusion databases [64, 65], usage of Bayesian methods and support vector machines [66, 67], conformal predictors [68, 69] etc. are some examples of work that has been done by him and his coworkers on offline application of data-based techniques. Application towards development of real time systems were also realized with the introduction of ITER like wall in JET [70, 71, 72]. More recently, an overview of the progress made in the past two decades was published in Nature Physics [73].

The list can be very long, with different methods using reduction in dimensionality, independent feature extraction etc. with the goal to eventually obtain a machine independent predictor for wider usability and affordable scaling. In the next chapter some examples of such predictors are discussed in detail which were developed by the data analysis group headed by Jesús Vega at CIEMAT.

Chapter 4 – State of the Art

In this chapter, a detailed discussion is presented with regards to the advances made in the field of disruption predictor development at the Laboratorio Nacional de Fusión (LNF). Different predictors based on usage of different machine learning methods are discussed alongside a brief overview of their performance analysis. A concise introduction to some of the machine learning methods used in development of these predictors is given in the beginning in order to help the reader familiarize the terminology.

Majority of machine learning problems can be simplified by bringing them down to a classification problem. Different shades of colors, fruits or vegetables from the same class, species belonging to the same class etc. are some examples. In case of fusion plasma discharge, when disruption prediction is the task at hand, the problem can be translated to a binary classification problem with two class labels: disruptive and non-disruptive. One of the most used machine learning method at the heart of such classification problems is known as Support Vector Machine (SVM), which falls under the category of supervised learning. Supervised learning consists of training the machine using examples with labels. Just like humans learn to distinguish between lemons and oranges after being told at least once which one is an orange and which one is a lemon- as if they were labelled. This is an example of supervised learning because prior information was provided in terms of someone telling us which one is an orange and which one is a lemon. Based on that information, certain properties are associated with each of them. Their color, odor, texture etc. are features (they can be scalars or vectors), characteristics that we use to recognize automatically once we have seen enough examples of that. Similarly, a support vector machine is a supervised learning technique where labels are provided in the training phase of the algorithm. The ultimate goal is to be able to assign a class label automatically in future after having seen a wide variety of features for each class. As per Noble [74], the most essential concepts for a working understanding of SVM classification are:

I. **The separating hyperplane:** Hyperplane is the general term for a straight line in a multi-dimensional space. For a linearly separable problem, this hyperplane is a straight line separating two different clusters

of objects whereas for a multi-dimensional problem, it is a hyperplane. In a nutshell, it can be reduced to a problem of pattern recognition based on features.

II. **The maximum-margin hyperplane:** There exist different machine learning methods that use a separation boundary for classification problems. SVM is different to others by virtue of the process by which the separating hyperplane is selected because there can be infinite lines passing through one single point but in SVM, the line for which the distance between the line and the nearest feature is maximum for all the classes is chosen. This way, SVM intrinsically possesses a very high possibility for correct classification even for future objects. An important factor for this to work at its maximum potential though, is that the data used to obtain the hyperplane should belong the same distribution as the one whose classification is at hand. Also, it is important that the feature extraction procedure is unchanged during training and testing, otherwise, the features might carry artifacts that can affect the performance of the SVM.

III. **The soft margin:** There might be instances where an object cannot be classified as belonging to one single class due to many different reasons. Ideally, SVM should be able to tackle such exceptional occurrences but there is also a possibility to introduce a **soft margin**, which essentially allows some data points to push through the margin of separating hyperplane without altering the final result. It is also important to recognize that the definition of such a soft margin is a very complicated task and must be carried out with utmost caution in order to reduce existing misclassification without paying the price of eventual misclassification of otherwise correctly classified objects.

IV. **The kernel function:** Even though dimensionality reduction is considered to be helpful for classification problems, there may be cases where it is actually hindering the determination of a separation hyperplane for SVM based classification. Hence, a kernel function is implemented to add n new dimensions to the data- where n can be infinite. This transformation can eventually result in reduction or even removal of the problems related to classification. However, the choice of kernel function is not straightforward and needs a lot of experience and intuition towards the data to be classified. One can prove analytically that if the data set

has consistent labels (meaning that no identical objects are assigned two different labels), a kernel function exists which will allow the data to be linearly separated.

Before proceeding further, it is important to mention the JET Protection System (JPS) [75]- a real time system used for producing disruption alarms. JPS mostly relied on elevated values of mode locked signal for alarm triggering. The methods discussed in following sections were designed with an objective of providing better alarm triggers compared to the JPS. Recently JPS was replaced by PetraMit1 and PetraMit2 for device protection.

4.1. Advanced Predictor Of DISruptions

APODIS is not a physics based system, it rather uses data science to come up with a functionally viable disruption predictions. Starting from as many as 13 diagnostic signals (as listed in table 4.1), throughout the process of performance improvement, APODIS ended up with 7 signals (those in bold in table 4.1) which are used in the real time version.

A feature extraction scheme as described in [76] was employed to obtain features at every 32 ms in order to achieve better detection rates. It is very important to highlight that not all the signals were available at a uniform sampling rate and hence, as a part of pre-processing, a common sampling rate was established and all the signals were brought to the same. Several different predictors, based on SVMs were trained focusing on different time intervals prior to disruptions. Based on the outputs of those SVMs, a decision function (DF) was used. The objective of the DF is to make a decision regarding alarm trigger. Hence, the "prototype" APODIS worked on a double layer SVM based combination of predictors. One criterion, essential while evaluating the viability of such systems, is the amount of computational time they require for training. In case of this prototype, the first layer required a computational time of ~1h on a Pentium 4 3.2 GHz CPU using Matlab. The critical layer, the one containing DF required ~10h for training. These timings can be further reduced using high performance computing and hence, make this prototype a viable option.

The training was carried out using JET discharges (a mix of disruptive and non-disruptive discharges, ranging from Jet Pulse Number (JPN) 42815-57346). For testing purposes, discharges up to C14 have been used and no performance degradation has been observed. Structural modifications after C14

resulting in replacement of the divertor and bolometric diagnostic reflected a slight degradation in the performance from C15 till C19. This predictor was tested in a simulated environment whose in depth analysis and results are presented by Rattá et al. [77].

Signal Name	**Units**
Plasma Current (I_P)	A
Poloidal Beta (β_{Pol})	
Time derivative of Poloidal Beta ($\frac{d\beta_{Pol}}{dt}$)	s^{-1}
Mode lock amplitude (ML)	T
Edge safety factor (q_{95})	
Time derivative of edge safety factor ($\frac{dq_{95}}{dt}$)	s^{-1}
Total input power (P_{TOT})	W
Plasma internal inductance ($L_{Internal}$)	
Time derivative of plasma internal inductance ($\frac{dL_{Internal}}{dt}$)	s^{-1}
Plasma vertical centroid position (z_{plasma})	m
Plasma density (n_e)	m^{-3}
Time derivative of stored diamagnetic energy ($\frac{dW_{dia}}{dt}$)	W
Net power (P_{TOT} - P_{RAD})	W

Table 4.1: The original list of signals considered for APODIS, the symbols in brackets next to the signal names are used in JET communications.

When the JET went an overhaul for preparation for ITER relevant experiments, the PFC wall was changed and ILW was implemented. Using the learnings of the prototype version of APODIS and its consequent performance degradation after JET divertor replacement as well as bolometric diagnostic upgrade, several changes were made prior to real time implementation of APODIS. Apart from inclusion of exhaustive data pre-processing for outlier removal and usage of high performance computing, the signal representations, the signals, the amount of data considered for training and real time applicability were the improvements made to the prototype. Studies revealed [78] that different signal representations combination in APODIS provides the possibility to reduce the number of signals required and as a result, two signal representations per window were used: mainly the standard deviation of the Fourier spectrum (without the continuous component) and the mean value. In terms of real time implementation, the moment in a JET discharge the plasma

current supersedes a certain threshold value (presently 1 MA), APODIS starts forming a feature vector $\boldsymbol{x}$ every 32 ms. As mentioned, using the two signal representations being mean value and Fourier spectrum standard deviation for 7 signals (table 4.2), a feature vector $\boldsymbol{x} \in \mathbb{R}^{14}$. Upon completion of a 32 ms time window at a time instance t, APODIS uses the three most recent feature vectors $(\boldsymbol{x}(t-64), \boldsymbol{x}(t-32), \boldsymbol{x}(t))$ as inputs for three SVM based classifiers M3, M2 and M1 respectively (see fig. 4.1).

Signal Name	**Units**
Plasma Current (I_P)	A
Mode lock amplitude (ML)	T
Total input power (P_{TOT})	W
Plasma internal inductance (LI)	
Plasma density (n_e)	m^{-3}
Time derivative of stored diamagnetic energy ($\frac{dW_{dia}}{dt}$)	W
Net power (P_{TOT} - P_{RAD})	W

Table 4.2: Final list of signals used in APODIS.

The outputs from M3, M2 and M1 are classified as disruptive or non-disruptive depending on the properties of the features and there may be occurrences where not all three output are in agreement with one another. Hence, the DF based on SVM in the second layer eventually decides the prediction value for the given discharge at time instance $\boldsymbol{t}$. Detailed results of APODIS performance on ILW discharges are summarized by Vega [70].

As shown by Moreno et al [79], APODIS relies highly on the mode lock amplitude and plasma internal inductance signal. The remaining signals are also essential but any alteration in those signals by means of noise or calibration artifacts are not reflected as a grave degradation of performance. Also, the use of a sliding window method to test APODIS performance for different temporal resolutions without actual resampling of original data shows that the higher the temporal resolution, the better the performance even in terms of improvements in warning times as shown in the same article.

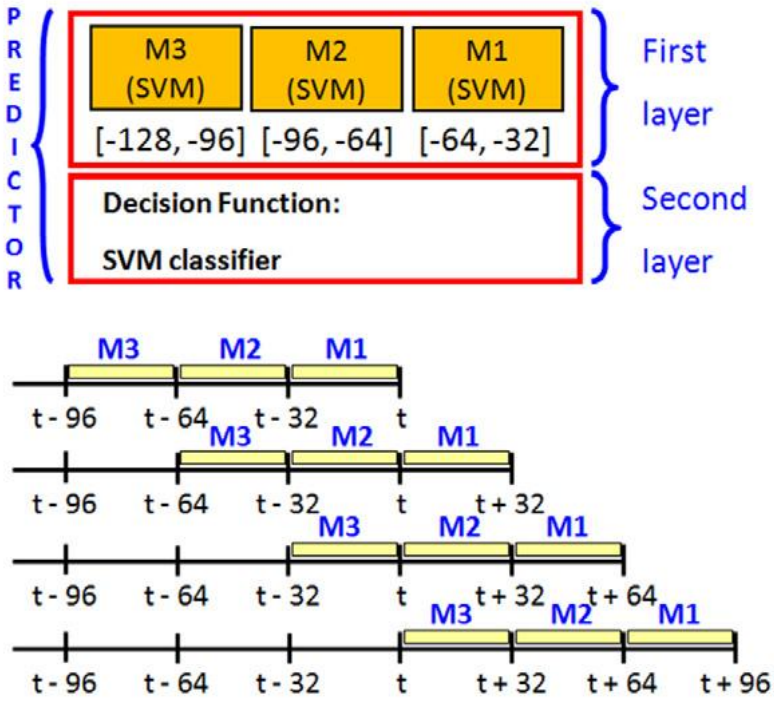

Figure 4.1: APODIS architecture implemented in the JET RTN.

4.2. Approximation from Scratch

A large number of machine learning and data driven methods for prediction and classification strongly rely on the vastness of the available historical data to learn from it before making predictions. However, ITER will not have the luxury of such a database for training disruption predictors mainly because it is not designed to withstand disruptions. According to Strait [80] the maximum number of unmitigated disruptions in ITER is very limited at high current scenarios ($I_P > 8.4$ MA). Lehnen [81] provides an insightful take on possible disruption rates for different operational scenarios in ITER depending on the successful execution of the tasks (fig 4.2).

A very important strategy that can be adapted to prevent damages from disruptions for ITER is to develop predictors from scratch. The core idea in such an approach is usually to carefully select diagnostics signals and investigate relations between them to identify an impending disruption. The physics interpretation is desirable but not compulsory. One such predictor was related to APODIS. The APODIS performance during the first three ILW campaigns was very satisfactory. Good detection rates, no apparent "ageing" and reliable detections caused APODIS to be chosen for predictions from scratch. Here the

word “ageing” is related to the degradation of performance of a predictor when used in environment drastically different than the one used for training.

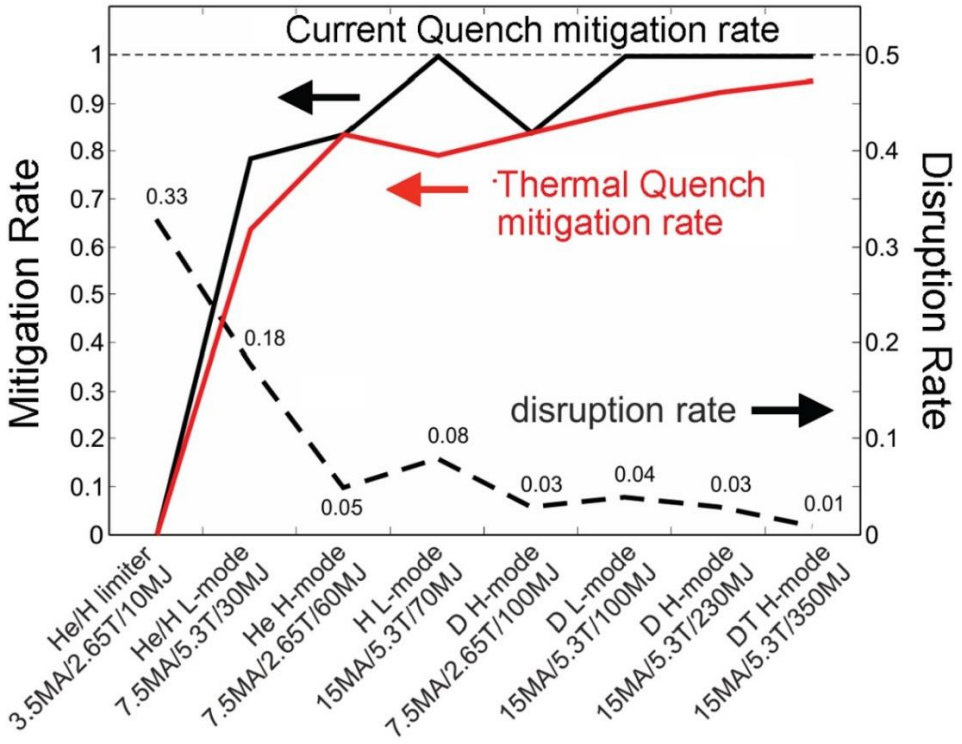

Figure 4.2: A probable scenario of permissible disruption rate at ITER [81]

The most important criterion in development of a predictor from scratch is the chronology of discharges- the system needs to learn on the go which behavior caused disruption. So, whenever a disruption occurred, re-training was carried out to incorporate new knowledge to the predictor for future predictions. Different types of training datasets were considered in order to train the predictor for different scenarios. As shown by De Vries [82], the number of disruptive and non-disruptive discharges is rather unbalanced considering only unintentional disruptions. High performance computing (HPC) facility available at CIEMAT, containing 240 nodes of 2 Quad-Core Xeon processors was used to train models based on APODIS. A total of 1035 non disruptive and 201 disruptive discharges from ILW campaigns at JET were used for training and testing the models. All the discharges with incomplete or unreliable data were excluded from the database. Careful selection of signals was made to maximize the learning parameters for the models without overloading the predictor with information.

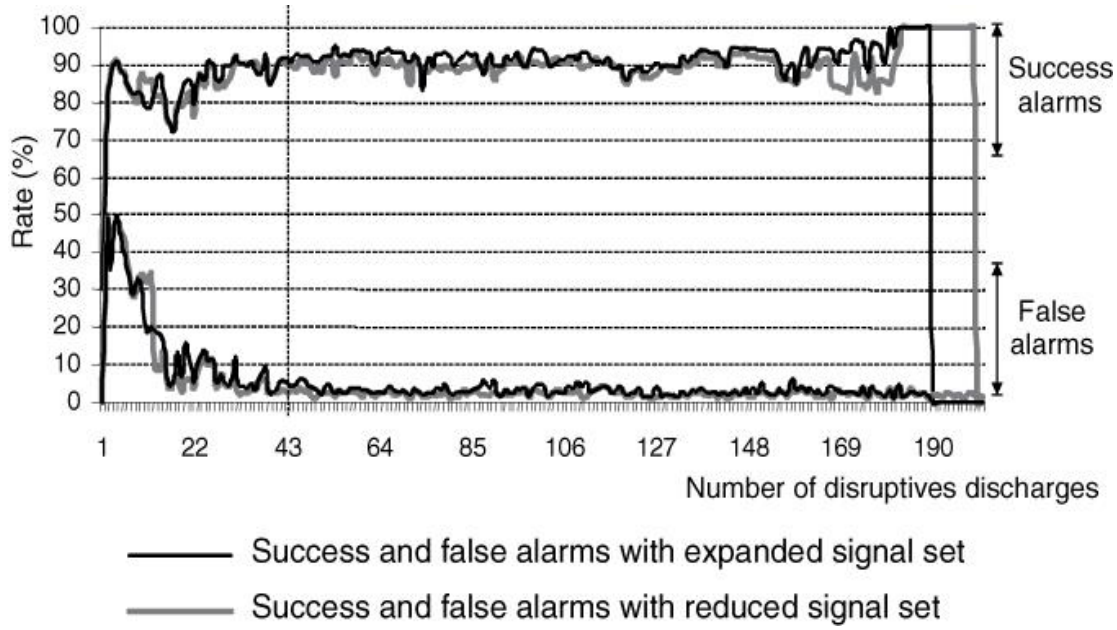

Figure 4.3: Disruption prediction results from scratch [83]

As can be seen figure 4.3, a model, trained from scratch is good enough to achieve very high success rates while maintaining a very low false alarm rate. The expanded signal set used 12 carefully chosen plasma diagnostics signals whereas the reduced signal sets used only 7 of the 12 signals utilized by the expanded set. Here it is important to point out the sudden fall of success rate in figure 4.3. It is due to the fact that for model 200, there is only 1 disruptive discharge in the test set and hence, if it is missed, the success rate falls to 0%. This raises an important question regarding re-training, highlighting the fact that not every occurrence of disruption mandates it since if the disruption is detected, it means that the model does have the necessary knowledge to detect similar disruptions and only the ones missed have new information that need incorporation in the knowledge pool. Such a deduction is very useful to avoid unnecessary time loss in re-trainings and swift employment of the predictor. A detailed account of this predictor is given by Dormido-Canto et al. [83].

The predictor from scratch based on APODIS managed to achieve success rate of 93.5% and false alarm rate of 2.3% after using only 40 disruptions to train the model. This is still too high a number for ITER and future reactor class tokamaks because while operating at high performance scenarios, unmitigated disruptions can be fatal. Another approach based on fault detection and isolation (FDI) techniques was also devised and deployed in AUG [84] but higher false alarm rates left more to desire. A predictor based on Venn prediction

framework was proposed and reported by Vega et al. [85] providing probabilistic predictions, qualified with a probability interval to interpret the efficiency of the predictions. Such auto-qualification of predictions made by a predictor put them in a category known as conformal predictor, formulized by Vovk and Gammerman [86].

Conformal predictors work differently when compared to normal machine learning predictors. Instead of using a fraction of the available database to train itself, a conformal predictor makes predictions sequentially and can be used either in batch mode or online mode. In other words, the induction derived from the training does not need to go through the model unlike a normal classifier, it can straightaway be translated to a prediction and qualified for its efficiency. This makes it fit perfectly in the requirements of predictions from scratch. Each new prediction made by a Venn predictor is based on all the previous samples. The only assumption made in the formulation of the Venn predictor is that the information to be used satisfies the independent and identically distributed data (IID) hypothesis.

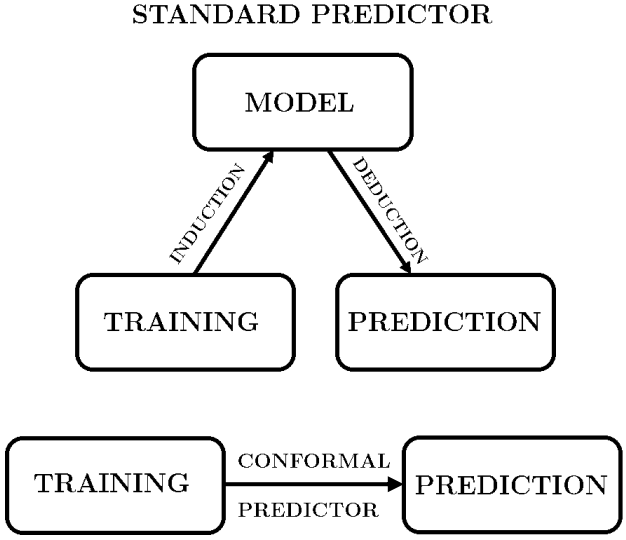

Figure 4.4: A comparison between standard and conformal predictors.

Different Venn machines can use different taxonomies to classify samples into different groups. For multiclass classification, neural networks as well as SVMs and even logistic regression have been used. The Venn predictor discussed in [85] was based on the nearest centroid taxonomy (NCT) given the fact that the problem could be tackled in terms of a binary classification problem and the information about *disruptivity* can be stored in centroids of disruptive and non-

disruptive type. This meant that the NCT Venn taxonomy number is 2 where the label to a sample was assigned similar to its nearest centroid. The metric for distance was chosen to be Euclidean. Once a taxonomy was chosen, probabilities were calculated for each sample belonging to each class and at the end, labels were assigned with the condition that the label with highest average probability interval is the prediction. The probability interval was given by the minimum and maximum probability for each label for the given sample.

4.3. Anomaly Detection

Continuing with the theme of the chapter, continuous learning and sequential data observation as well as decision making remains the principal focus of the next type that we discuss- predictor based on anomaly detection. The fundamental assumption for anomaly detection is the data be compliant to the IID hypothesis because this would guarantee any anomaly detection to be associated with interesting time-dependent phenomenon useful for prediction of disruptions. This system could also be employed in a predictor from scratch framework, where the predictor acquires new knowledge with each new discharge- be it disruptive or non-disruptive. Especially, non-disruptive discharges in different experimental scenarios could demonstrate different classes of non-disruptive plasma behavior, essential for a seamless performance. As for disruptions, any detected anomaly must be associated with a precursor to assure that the false alarms are minimized and interesting plasma scenarios are obtained for better understanding. For starters, the most reliable precursor- locked mode amplitude was chosen to test a predictor based on outlier detection (PBOD, later known as Single signal Predictor based on Anomaly Detection -SPAD). Here the reference to term *outlier* points to the fact that any anomalous behavior observed in the data stream that has little to no relevance of previous samples of the data stream is most likely to appear rather far away from an otherwise closely grouped cluster of samples in the parameter space. Several points taken into consideration while designing the predictors are as follows:

- **i.** The sequential data must be read only once.
- **ii.** The time delay between a true alarm and its detection is minimal.
- **iii.** Number of false and missed alarms remain negligible.
- **iv.** Handling of the data streams be highly efficient from a computational point of view in order to facilitate real-time implementation.

Based on experiences with APODIS, the feature selection process for SPAD was carried in a similar way to that for APODIS. A time window of 32 ms was chosen to extract features from the ML signal, which is usually sampled at 500 Samples/s- producing 32 samples per time window to be processed. The information in those 32 samples was further reduced in terms of fewer components using the Haar wavelet transform. Additionally, a sliding window mechanism was used which so that every new sample was grouped together with previous 31 samples in order to assure a continuous sequential feature flow. A detailed account of the model as well as results obtained by SPAD is given by Vega et al. [87].

The PBOD approach provided an encouraging result, which was developed further with more sophisticated design capable enough for real-time application. SPAD was designed specifically for a Multithreaded Application Real-Time executor (MARTe) framework- originally developed for JET real-time applications but now extended to be used in fusion experiments across the globe like COMPASS, RFX etc. The SPAD algorithm aimed at detection of anomalies in the data distribution following the approach adopted in PBOD- where a 32 samples long feature vector was decomposed using the 4^{th} level Haar wavelet transform and the resultant decomposition coefficients were used as feature vectors. This way, the information in both time and frequency domain is put to use for anomaly detection. As can be seen in figure 4.5, non-disruptive and disruptive behavior is different and deviation from non-disruptive behavior is clearly visible. Presence of high covariance resulted in Mahalanobis distance from the centroid of the cluster representing non-disruptive behavior being used to separate the outliers in an effective manner. Qualification of outliers was carried out by means of calculation of an outlier factor based on the mean and standard deviation of the Mahalanobis distance during the discharge. A threshold value of outlier factor was chosen for alarm triggering.

A quick overview of MARTe applications is necessary since SPAD is based on it. Any MARTe application consists of a set of generic application modules (GAMs) which are connected via the dynamic data buffer (DDB) such that each GAM is capable of reading and writing an arbitrary number of data from the DDB. Task specific GAMs are also used but in general, GAMs are executed inside processing threads managed by the real-time scheduler. GAMs in separate threads can communicate and synchronize if needed and configured to

do so. The biggest benefit of such an architecture is the possibility to modularize an algorithm so that if needed, the intermediate steps of the algorithm can be easily used by other applications, reducing the redundancy of data processing while providing efficient real-time capabilities. Figure 4.6 shows the structure of SPAD architecture in MARTe.

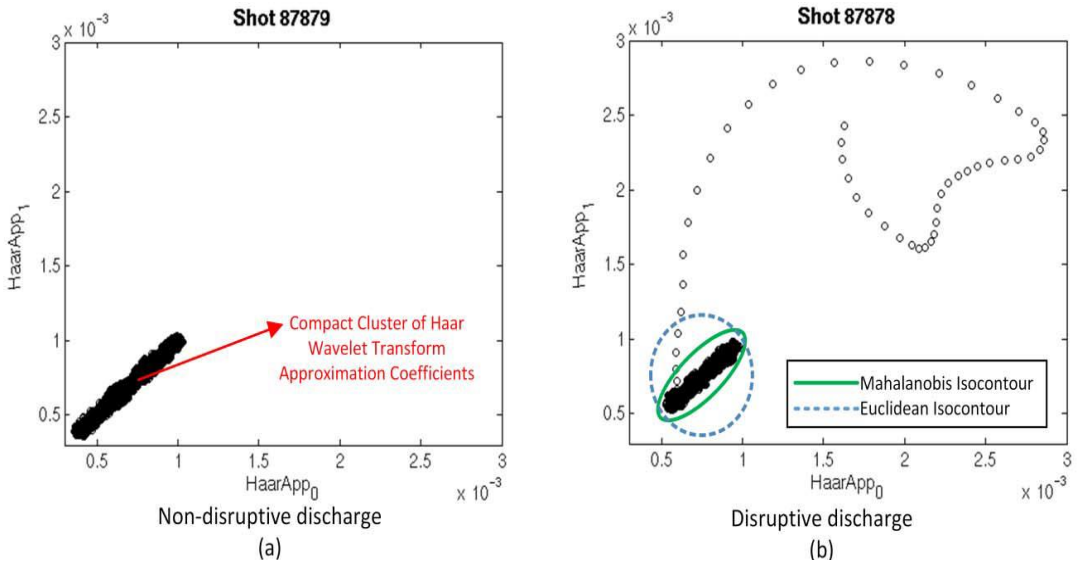

Figure 4.5: Comparison of the Haar wavelet transformation coefficients for a non-disruptive discharge (a) and a disruptive discharge (b). For both the discharges, the non-disruptive behavior is represented by a concise clustering of the feature vectors and the appearance of disruptive tendency is visible in (b) in terms of presence of outliers.

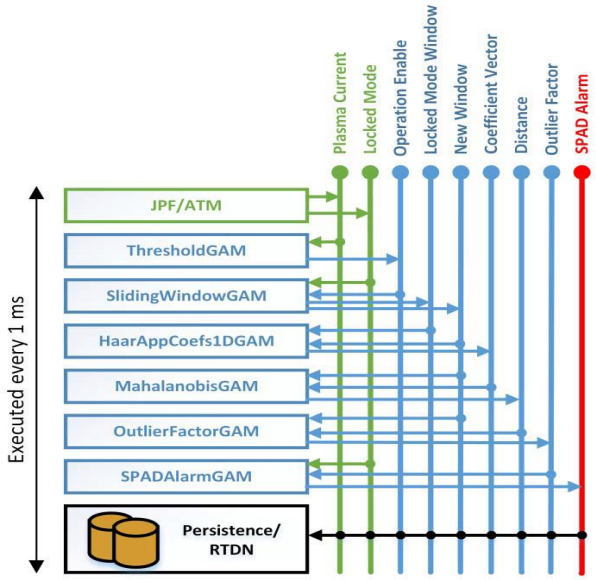

Figure 4.6: Diagram of SPAD implementation in MARTe. GAMs are executed in order from top to bottom [88].

A detailed account of implementation of SPAD in JET real-time network as well the results obtained from JET campaigns C28-C34 are given by Esquembri et al [88]. Different sizes of feature vectors were tested to verify if it was a factor in the performance of SPAD. Overall, SPAD was found to be better compared to APODIS and ML predictor based on a hard threshold. Using only one signal, the execution time is also low so that in case of requirement of immediate action, it can be trusted fully.

Chapter 5 – The Centroid Method Predictor

In this chapter, a detailed discussion is presented of the Centroid Method (CM) predictor, which is at the core of this work. Some examples of implementation of the CM predictor to detect upcoming disruptions are also provided.

5.1. Centroid Method

Having seen the advantages and shortcomings of the different approaches for disruption predictor a simplistic yet efficient method was designed in recent years [89]. The method was designed keeping in mind the physics interpretation requirement as well as reduced complexity for easier implementation to new devices, regardless of their size and working principle. One of the most exploited disruption precursors, Mode Lock Amplitude, is used to guarantee a reliable performance and efficiency, especially for disruption mitigation purposes. A multi-dimensional parameter space $\mathbb{C} \subset \mathbb{R}^m$, with each dimension being a physics related quantity can be considered. Using two simple rules, a global method for defining generic predictors can be summarized:

1. The knowledge of disruptive and non-disruptive physics in $\mathbb{C}$ can be represented by individual points C_D and C_{ND} as shown in figure 5.1.

2. Throughout a discharge, the plasma state at time t can be represented by a point $P(x_1, x_2, \ldots, x_m) \in \mathbb{C}$. The plasma state is recognized to be disruptive or non-disruptive based on the Euclidean distance of P from C_D and C_{ND}. If the Euclidean distance of P from C_D (d_{P,C_D}) is shorter compared to the Euclidean distance of P from C_{ND} ($d_{P,C_{ND}}$), then the discharge is categorized to be in a *disruptive* state whereas for the contrary scenario, the discharge is categorized to be in a *non-disruptive* state. The consistency in reasoning is drawn from the fact that the physics understanding of the plasma state is represented by C_D and C_{ND} and hence, the Euclidean distance provides a metric for similarity in behavior in the parameter space.

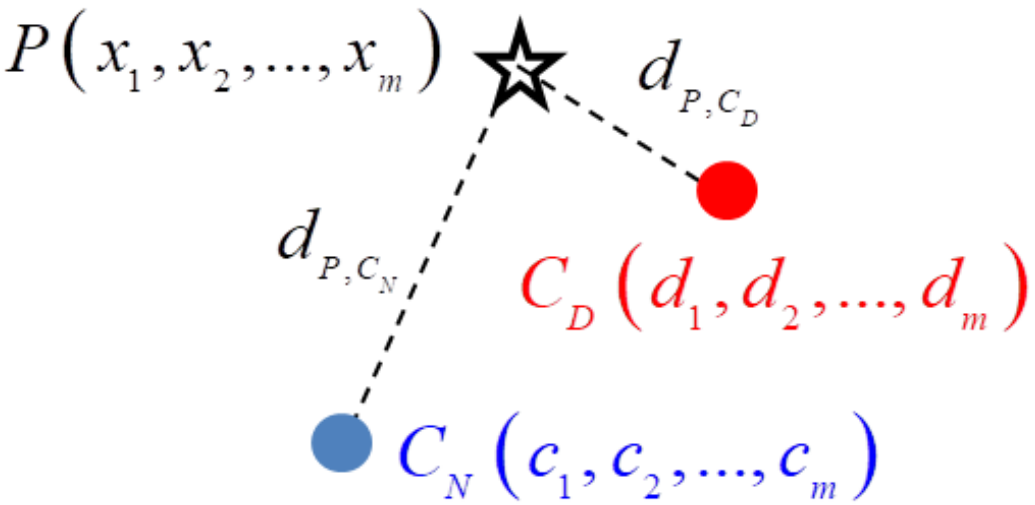

Figure 5.1. A general predictor can be based on the well-known nearest centroid technique. From m physics quantities, C_D and C_{ND} are centroids, which condense the relevant information about disruptive and non-disruptive behaviors, respectively, into two points in $\mathbb{C}$.

Points $C_D(d_1,d_2,\ldots,d_m)$ and $C_{ND}(c_1,c_2,\ldots,c_m)$ are the respective centroids of the disruptive and non-disruptive examples in the parameter space $\mathbb{C}$. Hence, the method is termed as the Centroid Method (CM) and the predictor is called CM predictor. Mathematically speaking, if a training dataset for each disruptive and non-disruptive type examples is given, then the coordinates of C_D and C_{ND} are obtained in the following manner. If the disruptive training dataset Ψ and non-disruptive training dataset $\mathbf{X}$ is defined as:

$$\Psi_i(\psi_{1,i}, \psi_{2,i}, \ldots, \psi_{m,i}) \in \mathbb{C}\,, i = 1, \ldots, n_D$$
$$\mathrm{X}_i(\chi_{1,i}, \chi_{2,i}, \ldots, \chi_{m,i}) \in \mathbb{C}\,, i = 1, \ldots, n_{ND}$$

C_D and C_{ND} are given by:

$$(d_1,d_2,\ldots,d_m) = \mathrm{mean}(\psi_{1,i}, \psi_{2,i}, \ldots, \psi_{m,i}),\ i = 1, \ldots, n_D$$

$$(c_1,c_2,\ldots,c_m) = \mathrm{mean}(\chi_{1,i}, \chi_{2,i}, \ldots, \chi_{m,i})\,,\ i = 1, \ldots, n_{ND}$$

where mean(O) returns a vector comprised of the average value of each column of Ψ and $\mathbf{X}$ with $\psi_{j,i}$ or $\chi_{j,i}$ and j=1,…,m.

A disruptive behavior is attributed to a point $P(x_1, x_2, \ldots, x_m)$ using such a predictor when the following condition is fulfilled.

$$d_{P,C_D} < d_{P,C_{ND}}$$

where $d_{P,C_D}$and $d_{P,C_{ND}}$ being the Euclidean distances, are defined by:

$$d_{P,C_D} = \sqrt{\sum_{i=1}^{m}(x_i - d_i)^2}$$

$$d_{P,C_{ND}} = \sqrt{\sum_{i=1}^{m}(x_i - c_i)^2}$$

resulting in,

$$\sqrt{\sum_{i=1}^{m}(x_i - d_i)^2} < \sqrt{\sum_{i=1}^{m}(x_i - c_i)^2}$$

which can be simplified using simple algebra to arrive at a condition for disruptive behavior as:

$$2\sum_{i=1}^{m}(d_i - c_i)\,.\,x_i \;>\; \sum_{i=1}^{m}(d_i^2 - c_i^2) \qquad (1)$$

Recurring to the fact that for each independent training set, the centroid coordinates are unique, the equation above is linear in x_i as follows:

$$\sum_{i=1}^{m} A_i . x_i > K \qquad (2)$$

where A_i, i=1,…,m and K are constants, determined during the centroid computation process as follows.

$$A_i = 2.(d_i - c_i)$$

$$K = \sum_{i=1}^{m}(d_i^2 - c_i^2)$$

Equation 2 summarizes the formulation of a very general disruption predictor that can be implemented in a simple way.

To compare the predictor represented by equation 2 with a machine learning predictor, several key points as followed must be taken into consideration.

i. The criterion for assigning classification label is very simple, shortest distance to a centroid. There are no underlying factors like layers, neurons, kernels, leaves. The absence of these factors also remove the dependency on otherwise time consuming optimization algorithms for training. Improvements in terms of re-trainings can be made in a quick and efficient ways if new examples are added to the training set. In a nutshell, equation 2 is extremely use friendly.

ii. Linearity of equation 2 in physics quantities translates in reliable physics interpretation compared to predictors relying on several different signals resulting in a non-linear model.

iii. Continuous recognition of plasma behavior can be achieved with a resolution of the order of 100 µs since the only mathematical operations to be executed are a product, sum and comparison after obtaining coordinates of points $P_t(x_1, x_2, \ldots, x_m)$ and plug them in equation 2.

iv. Equation 2 presents a case for multiple uses in terms of mitigation as well as avoidance of disruptions. One only needs to choose precursors for specific application and the corresponding signal(s) can be added to the parameter space $\mathbb{C}$. This flexibility is a result of global validity of equation 2- a feature most desired for disruption predictors.

v. The cost of computation is another salient feature of a predictor based on equation 2. The classification criterion being a linear inequality provides prediction efficiency even for a higher dimensionality (larger values of m) at minimal computational cost, making their real time implementation a much easier task compared to multi-layer and multi-system predictors. In JET, for example, the real-time network has 2 ms of characteristic time, which is sufficiently long for making predictions with equation 2.

Such a framework is very important for designing simple predictors with physics interpretation capability because the ultimate goal is not only to predict upcoming disruptions reliably, but also, to understand their causes. As a field test, a disruption predictor based on equation 2 was implemented in the JET real-time network under following specifications.

a. To facilitate physics interpretation of the predictions, usage of quantities in time domain was made. Avoiding the usage of frequency domain serves twin purpose in terms of easier physics basis as well as getting around the need of additional data processing in time windows with a limited sample size.

b. Lack of high performance ($> 95\%$ success rate and $< 5\%$ false alarm rate simultaneously for ITER) predictors and these predictors not being linear as well asserts another challenge to find the simplest linear predictor adhering to ITER requirements.

c. The dimensionality of the predictor was also chosen very carefully. It could be argued that the simplest linear predictor could be achieved by using only one dimension in equation 2. Consequently, that would lead to a single threshold value, an approach already used in JET and proven time and again to be not quite useful in achieving a performance we aim for. The principal reason for non-existence of an optimized threshold for JET discharges is the lack of a "universal" threshold value, valid for all types of experimental discharges. In some cases, even non-disruptive discharges surpass the preset threshold without disrupting, and hence, it has not been possible yet to obtain one single threshold value. For the one dimensional case, equation 2 gets reduced to:

$$A_1 . x_1 > K$$

which in its analytical form can be written as follows,

$$2.(d_1 - c_1).x_1 > (d_1^2 - c_1^2)$$

and with further simplification, we obtain the equation for one dimensional predictor

$$x_1 > \frac{(d_1 + c_1)}{2} \qquad (3)$$

which is represented graphically in the figure 5.2 as shown below:

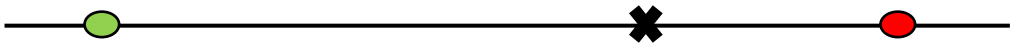

Figure 5.2: Here the green circle would represent non-disruptive centroid c_1 and the red circle would represent disruptive centroid d_1 with X being the point defined by x_1 in equation 3. In a nutshell, if a plasma state point has co-ordinate value higher than the average of disruptive and non-disruptive centroid value, the plasma will be characterized to be in a disruptive state and non-disruptive otherwise and hence, a threshold value.

The next attempt would lead to usage of two dimensional parameter space and with a classification condition of the form:

$$A_1 . x_1 + A_2 . x_2 > K$$

which takes the following form when we use the analytical forms of all the constants

$$2.(d_1 - c_1).x_1 + 2.(d_2 - c_2).x_2 > (d_1^2 - c_1^2) + (d_2^2 - c_2^2)$$

with further simplification, the equation to arrive at the condition for disruptivity for a plasma point x_2 reduces to:

$$x_2 > -\frac{(d_1 - c_1)}{(d_2 - c_2)}.x_1 + \frac{(d_1^2 + d_2^2 - c_1^2 - c_2^2)}{2 \cdot (d_2 - c_2)} \qquad (4)$$

where x_2 is the point of plasma representing the actual state of plasma and x_1 is the plasma state point for the previous time instance.

d. Once the initial values of A_1, A_2 and K are found, a one-time optimization process was carried out to obtain the best suitable values for a global predictor such that no further optimization is required unless there are changes made to the measurement conditions (i.e. improvement of diagnostics, changes in the vessel etc.).

e. Based on several studies made over time [35, 82], mode locking is one of the most repetitive precursor to disruptions and the focus of the predictor being disruption mitigation. As a first step, the locked mode amplitude (ML) signal was chosen as the physical quantity for the predictor.

Based on above mentioned specification, for a two dimensional parameter space, the second signal to be chosen should also be related directly to physics of mode locking. However, if the interdependence of the two chosen signals is not simple enough to translate into straightforward physics interpretation, the option to totally avoid the second signal could also be employed. This would render the predictor independent of practical issues related to a second signal like availability, sampling rate, reliability etc. and improve the robustness. In order to test the possibility, the ML signal itself was mapped in a two dimensional feature space and used in the predictor based on studies reported in [89, 90, 91]. Consecutive samples of the ML signal were used to define the two dimensional parameter space and figure 5.3 shows how the consecutive samples from ML signal are used to define plasma state points in the parameter space. Assuming

the sampling period of the ML signal to be τ, the two consecutive samples x(t-τ) and x(t) would define a plasma state point P(x(t-τ), x(t)).

Having defined the two dimensional feature space, the next step was to compute the coordinates of disruptive and non-disruptive centroids C_D and C_{ND} respectively. In consistency with the procedure elaborated earlier in the section, if the training datasets of disruptive and non-disruptive examples are:

$$\Psi_i(\psi_{1,i}, \psi_{2,i}) \in \mathbb{C}, i = 1, \ldots, n_D \text{ and}$$
$$X_i(\chi_{1,i}, \chi_{2,i}) \in \mathbb{C}, i = 1, \ldots, n_{ND}$$

the coordinates of C_D and C_{ND} are given by:

$$C_{ND}(c_1, c_2) = \text{mean}(\chi_{1,i}, \chi_{2,i}), i = 1, \ldots, n_{ND} \text{ and}$$
$$C_D(d_1, d_2) = \text{mean}(\psi_{1,i}, \psi_{2,i}), i = 1, \ldots, n_D$$

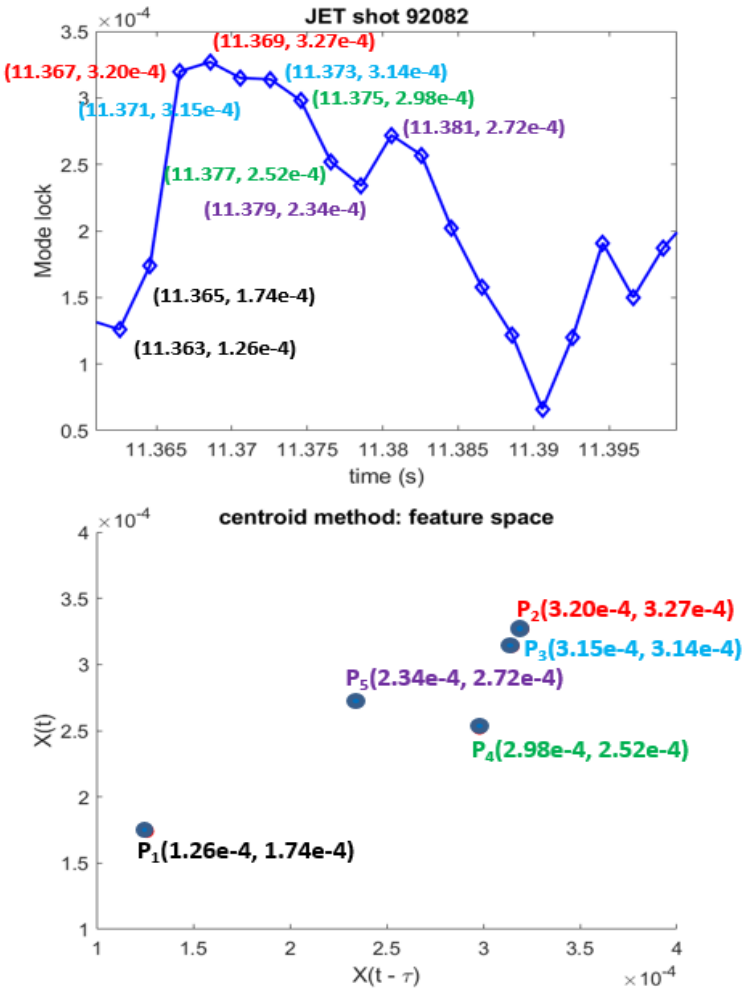

Figure 5.3: ML amplitudes in black, red, cyan, green and purple diamonds are points P1, P2, P3, P4 and P5, respectively, in then feature space. X(t) are the ML amplitudes (in T).

A quick description of how the examples of disruptive and non-disruptive examples of each individual discharge are obtained is also important for the completeness of explanation. For a non-disruptive discharge, the time interval for training is determined based on the values of plasma current, that is, the interval begins when the plasma current surpasses a value (say I_{start}) for the first time and finishes when the plasma current goes below a different value (say I_{finish}) for the last time. For the given predictor, the values chosen were: $I_{start} = 0.9$ MA and $I_{finish} = 0.7$ MA.

In case of a disruptive discharge, the procedure is slightly different largely owing to the fact that the appearance of disruption precursors is not consistent in terms of the time between their appearance and time of disruption because different instabilities grow on different timescales and it is quite possible that the same instability in two similar discharges may grow at different growth rates since the growth rates are dependent on factors that might not be identical even for similar discharges.

The difficulty was partially eased out since the main purpose of the predictor to be designed was disruption prediction for mitigation and hence, it was reasonable to choose the feature vectors closer to the disruption in order to capture the essential characteristics of the disruptivity of each discharge. Care was also taken that only one example per discharge was considered in $\mathbb{C}$ and that it was as close as possible to the disruption. The example to be chosen must comprise of consecutive samples of features nearest and prior to the disruption with a positive difference of their ordinates. The reason behind such a stringent criterion is the fact that appearance of the chosen precursor is generally associated with and identified by a monotonous increment in the amplitude of the corresponding diagnostic signal.

Here it is also crucial to define the meaning of the term *training*. Training in this case means computation of centroids, which is carried out after feature vectors for all the discharges selected as representative cases for different type of disruptive and non-disruptive discharges depending on the experimental scenario they belong to; because different plasma configurations lead to different precursors. All the discharges used to train this predictor were executed after the upgrade of JET first wall to facilitate ILW conditions as mentioned in chapter 1. The time of disruption is chosen to be the time of beginning of the current quench. Only filtering criterion in terms of selection of disruptive discharges for

training and test was the disruption to have occurred naturally and not provoked intentionally.

The predictor based on the centroid method presented in this thesis is tested with the mode lock amplitude normalized to plasma current (ML/I_P). As explained in detail in chapter 2, the ML/I_P is already used in JET as a part of the protection scenario in PETRA and the disruption alarm is triggered once it crosses a threshold value, typically set between 0.4-0.52 mT MA^{-1} depending on the experimental scenario [91]. Worth highlighting is the fact that both ML and I_P are two routinely produced signals in tokamaks and hence, the usage of such a predictor is very appealing to the community.

Type/use	**Number of discharges**	**Range**
Disruptive/Training	113	80181-82504 SEP 2011-MAR 2012
Non-Disruptive/Training	1397	80176-82550 SEP 2011-MAR 2012
Disruptive/Test	277	82569-92410 MAR 2012- NOV 2016
Non-Disruptive/Test	3027	82552-92504 MAR 2012- NOV 2016

Table 5.1: Datasets of disruptive and non-disruptive discharges to train and test a predictor based on centroids in JET.

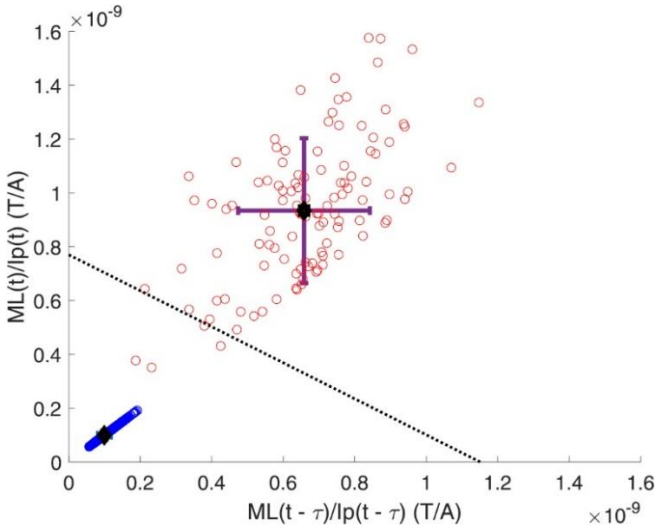

Figure 5.4: Black points with error bars are the centroids. Blue and red points are non-disruptive and disruptive examples of individual discharges, respectively.

Using the discharges from table 5.1, disruptive and non-disruptive centroids were obtained and are shown in the figure 5.4. The centroids are demonstrated for the mode lock normalized to plasma current. The sampling period of the ML/IP signal is $\tau =$ 0.002s. The dashed straight line is the separation line between disruptive and non-disruptive behaviors. The dashed line in the same figure represents the decision boundary, separating disruptive and non-disruptive zone in the parameter space. If we look at this model, it could be compared to an SVM based model where the task at hand is to label the plasma state at a time instance $\boldsymbol{t}$ to be either disruptive or non-disruptive- in other words, a binary classification problem. As was discussed briefly in the beginning of chapter 4, one of the key aspect of an SVM based classifier is the separation hyperplane and our parameter space being two dimensional, we obtain a straight line, represented by the dotted line in figure 5.4. The grouping of disruptive and non-disruptive centroids is well separated among themselves but the clustering is rather compact among the same type of examples.

$$C_D = (d_1 \pm \text{std } x_D,\ d_2 \pm \text{std } y_D), \text{ disruptive centroid}$$

$$C_{ND} = (c_1 \pm \text{std } x_{ND},\ c_2 \pm \text{std } y_{ND}), \text{ non-disruptive centroid}$$

with std(O) representing standard deviation

$$(\text{std } x_D, \text{std } y_D) = \text{std}(\psi_{1,i}, \psi_{2,i}), i = 1, \ldots, n_D$$

$$(\text{std } x_{ND}, \text{std } y_{ND}) = \text{std}(\chi_{1,i}, \chi_{2,i}), i = 1, \ldots, n_{ND}$$

High degree of compactness in the non-disruptive centroids cluster means that the effect of error bars in the determination of the separation hyperplane is negligible and that the individual centroids for each test discharge are similar to one another, mathematically, std $x_{ND} \approx$ std $y_{ND} \approx 0$. This, however, is not the case for disruptive centroids because there is considerable amount of spread in the cluster of disruptive centroids. Defining a square shaped region of interest using the values of error bars in each dimension, one can optimize and select the best disruptive centroid for the given set of training discharges. As shown in figure 5.5, 80 additional disruptive centroids were obtained. This exercise was important to correctly obtain the characteristic parameters of the separation hyperplane- mainly the slope and the intercept. In this case the hyperplane being a straight line in two dimensional feature space. 81 different centroids were considered, leading to testing of corresponding 81 different models and for

qualification of the best model, receiver operation characteristics (ROC) analysis was utilized. ROC analysis provides a performance analysis curve for different models based on identical datasets for training and testing by means of plotting the success rates versus their corresponding false alarm rates. The model whose corresponding coordinates in the ROC curve are closest to (0,100) is chosen as the most qualified model.

The ROC curve obtained from testing all 81 models corresponding to the disruptive centroid in figure 5.5 is presented in figure 5.6. The optimal model according to the ROC curve corresponds to the disruptive centroid with coordinates (d_1 – 0.75std x_D, d_2- std y_D). Results of success and false alarm rates corresponding to some of the 81 centroids tested for selection of best centroid are given below in table 5.2.

Model label	**Success rate (%)**	**False alarm rate (%)**
1	95.73	0.30
0.75	96.44	0.36
0.5	97.51	0.46
0.25	97.86	0.66
0	98.58	0.99
-0.25	99.29	1.35
-0.5	99.29	1.95
-0.75	99.29	3.73
-1	99.29	5.12

Table 5.2: Results of the process of optimization of disruptive centroid for JET. Here the model label is the value multiplied to the standard deviation of respective x and y co-ordinates of the base centroid obtained by taking global mean of the set of training discharges.

In terms of implementation, the CM predictor model in the JET RTN on PETRA is given by:

$$\mathrm{X\ (t)} = -0.6680\ \cdot\ \mathrm{X\ (t} - 0.002) + 7.2068 \times 10^{-10}$$

with X(t) being ML(t)/I_P(t), 0.002s is the sampling period of the signals used. ML being measured by the magnetic diagnostics, it is given in T and I_P in A. Provided the sampling period is the same as in the model, the presence of disruptive behavior is detected in case

$$X\,(t) > -0.6680 \cdot X\,(t - 0.002) + 7.2068 \times 10^{-10}$$

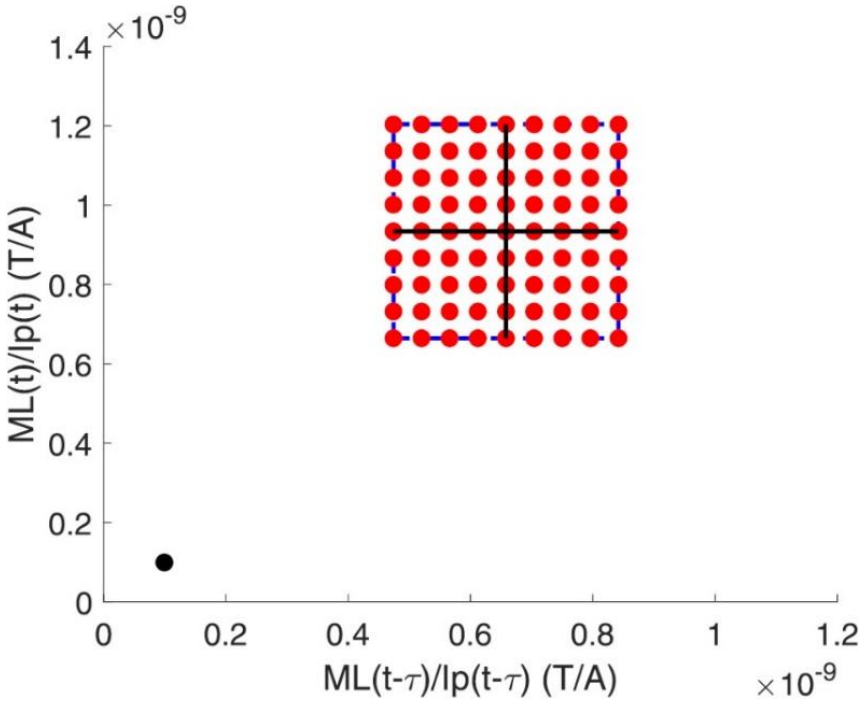

Figure 5.5: Apart from the initial disruptive centroid C_D (d_1, d_2), 80 new disruptive centroids are obtained with positive/negative increments of its coordinates in relation to the error bars in each dimension. Resultant 81 centroids are the red points.

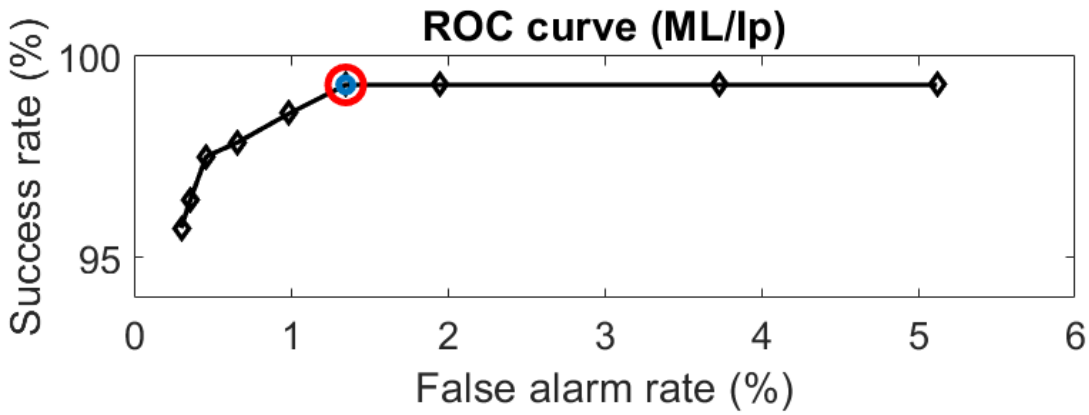

Figure 5.6: ROC curve for ML/I_P. The red square is the closest points to (0, 100) and determines the best predictor.

The CM predictor has more features, like an SVM based binary classification predictor. It removes dependence of the performance from a factor as trivial as temporal resolution of a diagnostic system. Not only that, but also, use of a soft margin as discussed in the early part of chapter 4 has been implemented as an additional feature.

The essence of CM predictor can be summarized via the fact that the predictions are made if abrupt changes are detected in the ratio of ML/I_P. A sudden increment in the ML amplitude while I_P being similar to the previous sample is a sign of mode rotation being slowing down and the mode locking on the VV wall, which is interpreted as disruptive behavior whereas a sudden drop in I_P value while ML amplitude is similar to the previous sample can also bump the resultant value of ML/I_P. A third possibility, where the amplitudes of both ML and I_P increase or decrease respectively at the same instance of time, could result in the value of ML/I_P not changing drastically, and hence, maintain around a hypothetical diagonal line X=Y in the feature space. Such behavior cannot be considered disruptive even if the corresponding plasma state points P(t) appear in the disruptive zone because during the training phase, such behavior is seen to correspond non-disruptive plasma state. However, as in the case of an SVM soft margin, a limit must be established in order to maintain the performance of the CM predictor without introducing any untoward bias.

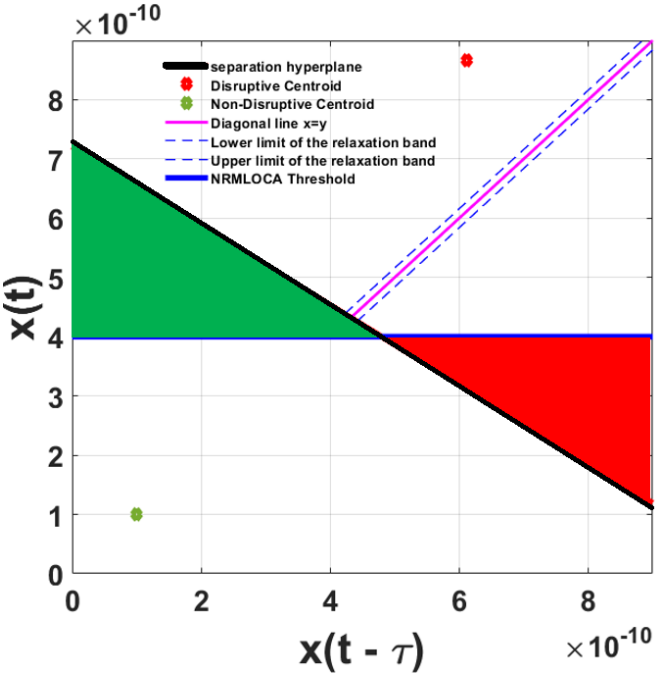

Figure 5.7: An illustration of the parameter space used in the analysis.

The green and red triangles in figure 5.7 are also highlighting the independence of CM predictor on manually set thresholds by comparing with the NRMLOCA predictor, constituent of the PETRA protection scenario using the same ML/I_P signal for disruption alarm triggering. The threshold for NRMLOCA at $X(t)=4\times10^{-10}$ T/A would result in false alarm triggering if a point P(t) appeared in the green triangle. If a point P(t) appeared in the red triangle, it would be considered as a non-disruptive behavior, which could lead to catastrophic effects in case of ITER. The CM predictor provides a greater degree of assurance in these regards with its separation frontier and hence, adds another point to the already favorable list of positive features.

The value of the soft margin, also known as the width of the relaxation band was chosen to be 1.1667×10^{-11} T/A on either side of the diagonal line X=Y as shown in figure 5.7. During the analysis of false alarms, it was observed that ~33% of false alarms were generated due to small disruptions, which plasma managed do recover from. In essence, those are actual alarms, only because plasma recovered and did not disrupt, they get the label of false alarms but it is important to note that the plasma went to the disruptive state, causing an alarm to be raised. Remaining 67% of false alarms followed a pattern where all the plasma state points in the disruptive zone are not only concentrated around the diagonal X=Y in the parameter space but also, their distribution around the diagonal can be represented mathematically as follows:

$$|x(t-\tau)-x(t)| \leq d_B \qquad (5)$$

where $x(t-\tau)$ and x(t) are consecutive plasma state points and d_B is the Euclidean distance of the farthest point from the diagonal line X=Y in the disruptive zone. Figure 5.8 shows a graphical representation of the relaxation band.

Optimal width of the relaxation band was chosen following a meticulous procedure where reduction in false alarms without the cost of reducing success rate was the main objective. Several values of d_B were tested as per following criterion.

$$d_{B,k} = k \cdot \sigma_D \qquad (6)$$

here, σ_D is the standard deviation of the distances of the individual disruptive training centroids to x(t) = x(t − t), k= 0,0.01,0.02,..., 0.1. The comparison of effect of different values of k on success rate, positive warning time and false alarm rate is demonstrated in table 5.3.

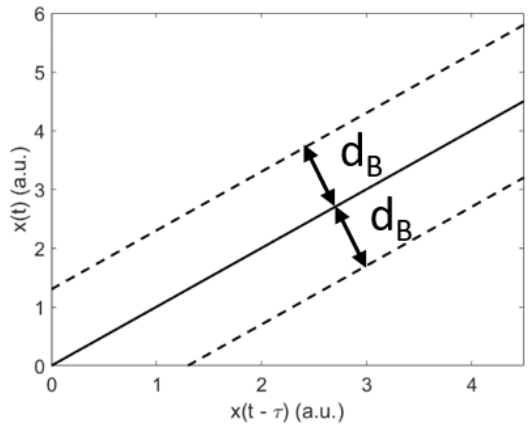

Figure 5.8: A graphical representation of the relaxation band on either side of the X=Y diagonal line.

k	**$d_{B,k}$ (mT/MA)**	**SR (%)**	**WT>0 (%)**	**FA (%)**
0	0	99.29	97.51	1.35
0.01	0.0021	99.29	97.51	1.32
0.02	0.0041	99.29	97.51	1.32
0.03	0.0062	99.29	97.51	1.32
0.04	0.0083	99.29	97.51	1.29
0.05	0.0103	99.29	97.51	1.29
0.06	0.0124	99.29	97.51	1.16
0.07	0.0145	99.29	97.51	1.16
0.08	0.0165	99.29	97.51	1.12
0.09	0.0186	98.58	97.15	1.12
0.1	0.0207	98.58	97.15	1.02

Table 5.3: Values of k reducing false alarm rate without affecting success rate as well as positive warning time detections. The row highlighted in red is the best result and was chosen to define the relaxation band for the CM predictor to be installed in the JET RTN.

It is very important to highlight the empirical fact that scatterplots of plasma state points in the parameter space can contain some points very far from the diagonal. If the values of k are chosen to be very high, a penalty in terms of drop in success rates was being paid. Table 5.4 shows how the larger values of k affected the success rate. A graphical representation comparing two JET discharges is also shown in figure 5.9.

k	$\mathbf{d_{B,k}}$ **(mT)**	**SR** (%)	**WT>0** (%)	**FA** (%)
0	0	97.51	96.80	1.62
0.1	0.0487	95.73	95.37	0.83
0.2	0.0974	94.66	94.31	0.56
0.3	0.1462	93.59	92.17	0.50
0.4	0.1949	92.88	90.39	0.36
0.5	0.2436	90.75	86.83	0.23
0.6	0.2923	86.48	81.85	0.20
0.7	0.3410	80.07	73.31	0.13
0.8	0.3897	72.24	65.48	0.10
0.9	0.4384	65.48	59.43	0.10
1	0.4872	60.14	54.09	0.07

Table 5.4: Effect of large k values on the success rate. Higher k values reduce false alarms but also reduce significantly the success rate as well as positive warning time detection rate.

Application of the CM predictor on JET discharges is illustrated in the following part of the chapter. Starting from an example of non-disruptive discharge- JPN 94152 in figure 5.10, a correct identification of a disruptive discharge- JPN 94156 is shown in figure 5.11. Then, an analysis of a missed alarm, JPN 94448 is given followed by a false alarm in JPN 94162 is also provided. All these examples are taken from the data obtained from PETRA, which houses the CM predictor and collects data for each discharge in real time. Note should be taken of the fact that during these discharges, the CM predictor was not being used for machine protection scenarios.

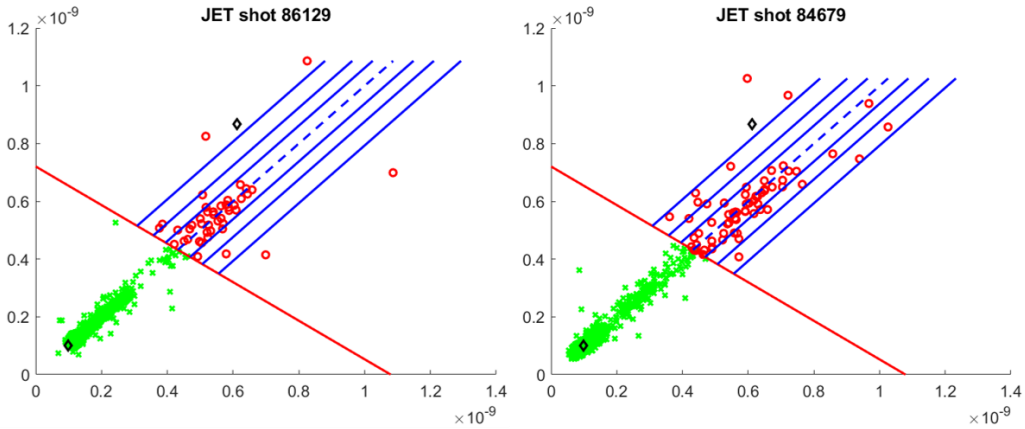

Figure 5.9: Example of JET discharges where several different bandwidths were chosen to filter out false alarms to obtain results shown in table 5.4. The green points are non-disruptive points, red points are disruptive points, red line is the separation hyperplane, diamond near green points is the non-disruptive centroid whereas the diamond near red points is the disruptive centroid. Blue lines are different bands and dashed line is the diagonal X=Y.

Figures 5.10-5.13 will have the same legends as follows. Green diamond represents non-disruptive centroid and red diamond represents disruptive centroid. Blue circles are non-disruptive plasma state points and red circles are disruptive plasma state points. Magenta line is X=Y diagonal and dashed blue lines around the diagonal define the relaxation band.

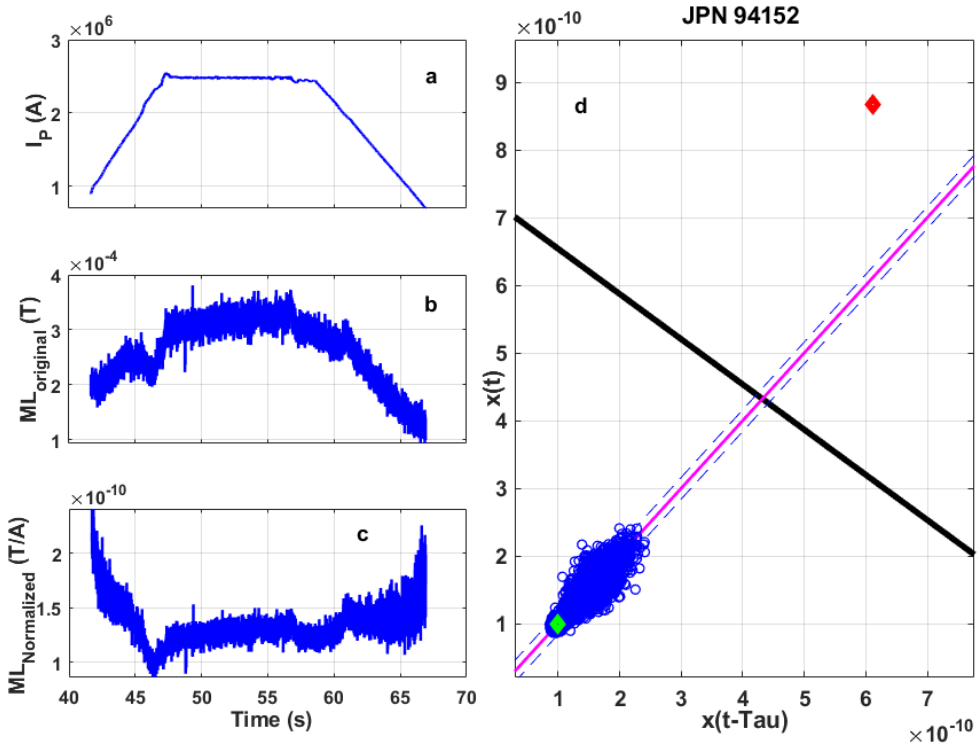

Figure 5.10: A non-disruptive discharge correctly identified by the CM predictor.

We can see that the discharge completes a proper cycle of plasma current ramp up, flat top and ramp down in 5.10 (a). The ML and ML/I_P are plotted in 5.10 (b) and 5.10 (c) respectively where they show no unusual activity. The evolution of plasma state is shown in 5.10 (d) where a clear clustering of points far away from disruptive centroid as well as separation hyperplane is visible. This is a correct prediction because there were no alarms raised by the CM predictor due to the fact that the plasma never switched its behavior from non-disruptive to disruptive. The next example is of a disruptive discharge, JPN 94156 where the CM predictor correctly identifies the change in plasma state from disruptive to non-disruptive and raises an alarm accordingly as shown in figure 5.11.

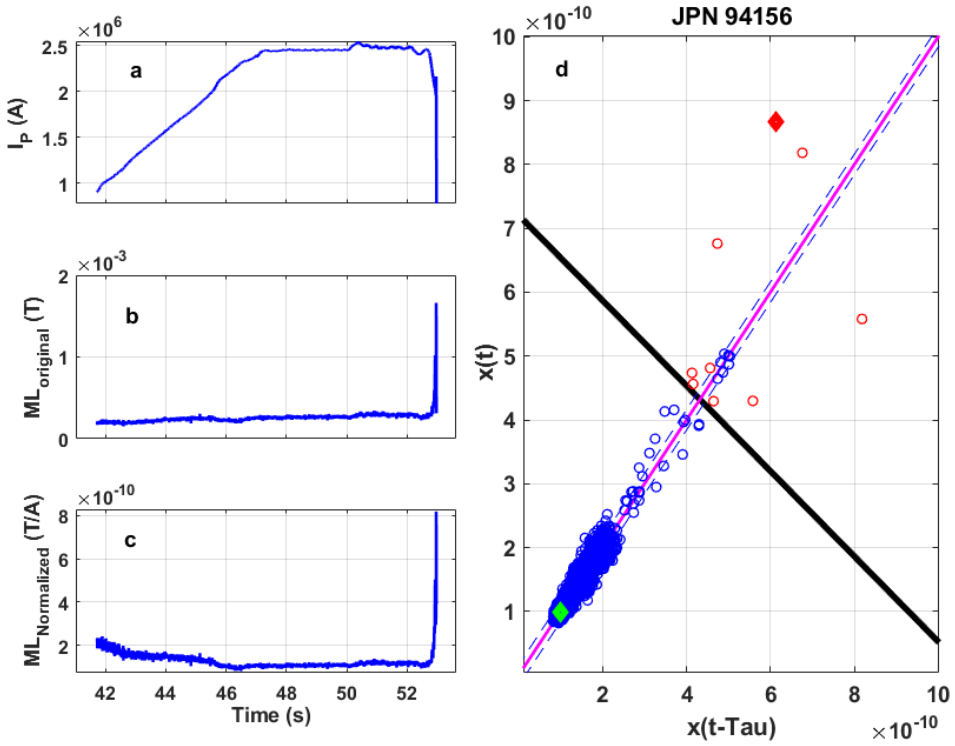

Figure 5.11: A disruptive discharge correctly identified by the CM predictor.

JPN 94156 is a disruptive discharge because as seen in figure 5.11 (a), the plasma current goes into a quench abruptly at ~ 53 s after ramp up and flat top phase. The upcoming disruption is also reflected in the sudden change of amplitude of ML signal in figure 5.11 (b) and consequently in figure 5.11 (c). Looking at figure 5.11 (d), we can see how the plasma goes from a non-disruptive state to a disruptive state by means of appearance of plasma state points from the cluster close to the non-disruptive centroid towards the separation hyperplane and into the disruptive zone. It is also worth noting that there are several points

in the disruptive zone which lie inside the relaxation band defined previously. Those points are correctly labelled as non-disruptive and shown with blue markers as compared to the disruptive points shown with red markers. Next is an example of a disruptive discharge not recognized by the CM predictor- which is terms of qualifying parameters, is a missed alarm.

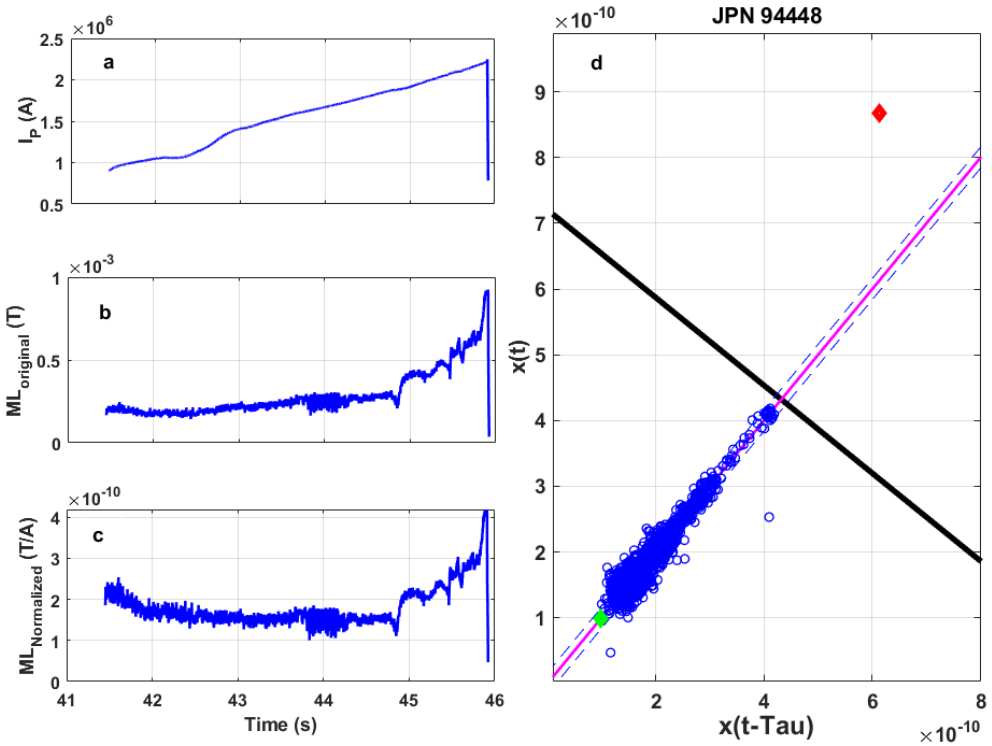

Figure 5.12: A disruptive discharge not identified by the CM predictor.

JPN 94448, a disruptive discharge was not correctly identified by the CM predictor as shown in figure 5.12. The discharge managed to go through the plasma current ramp up phase but just while entering the flat top region, disrupted violently as can be seen in figure 5.12 (a). As usual, figures 5.12 (b) and 5.12 (c) show corresponding activity in ML signals. Figure 5.12 (d) shows no points in the disruptive zone of the parameter space and hence, assigns JPN 94448 a non-disruptive label. Sometimes, the rate of current quench or the amplitude of saturated locked mode does not grow enough to surpass the separation hyperplane condition. In such a scenario, the CM predictor fails to identify a disruption correctly. This is a rare occurrence as will be shown in the following chapter where a detailed analysis of different JET campaigns is presented. Even though the plasma state points cluster is stretched far away from the non-disruptive centroid, some points almost reach the separation hyperplane

but cannot cross it. It is worth mentioning a factor that can sometimes cause some alarms to be missed and that is the enabling condition of the CM predictor. Depending on the experimental scenario, the JET RTPS and several other systems are enabled during a specific part of the discharge only. For example, if the condition for enabling CM predictor is a minimum value of I_P then, if the discharge disrupts immediately, the CM predictor does not see the disruptive behavior since it is not enabled, In the next example, a false detection is demonstrated where a non-disruptive discharge is incorrectly classified otherwise.

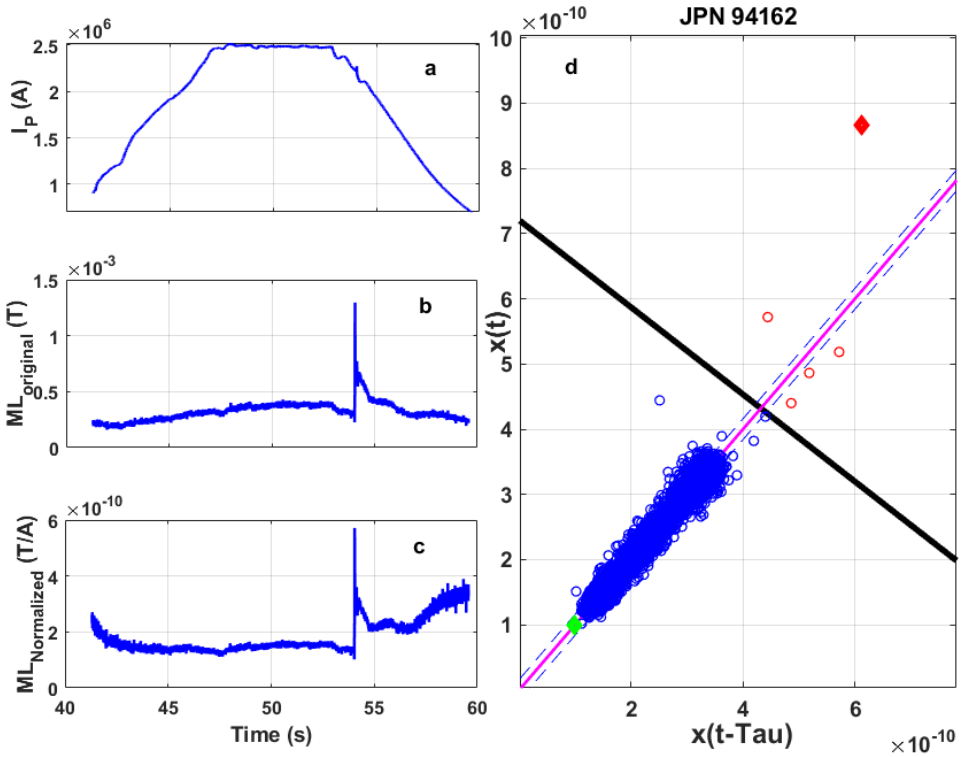

Figure 5.13: A non-disruptive discharge incorrectly identified by the CM predictor.

Here we demonstrate a false detection of JPN 94162- a non-disruptive discharge as a disruptive discharge. As shown in figure 5.13 (a), the discharge goes through the ramp up-flat top-ramp down phase in the expected manner. Even though there is a sudden activity on the ML signal, quite visible in figure 5.13 (b) and 5.13 (c), the discharge terminates safely. However, the CM predictor being sensitive to such abrupt changes in signal amplitudes, recognizes it as a disruptive behavior visible in figure 5.13 (d). The clustering of plasma state points is once again stretched away from the non-disruptive centroid and contrary to the missed alarm case, where no points could cross the separation hyperplane, four points did manage to appear in the disruptive zone outside the relaxation

band and hence, are identified as disruptive state points, causing the CM predictor to raise an alarm. Here again, the enabling condition for the predictor affects the overall rate of false alarms. If a discharge is to be executed at high I_P values (~1.5 MA and above), the I_P ramp up and ramp down phase can cause ML signal to pick up activity even though the plasma is in a non-disruptive state. The extreme sensitivity of CM predictor towards abrupt changes in ML amplitude demands that the predictor enabling criterion be set very carefully for each experimental scenario in order to obtain the maximum benefit of reliable prediction capability of the CM predictor.

In the next chapter, a detailed analysis of the performance of the CM predictor in the JET real time network is provided where a thorough comparison is made with other predictors constituting the JET RTPS.

Chapter 6 – Application and Results

In this chapter, a detailed report of the results obtained using the centroid method predictor is given. Application to the JT-60U data as well as various experimental campaigns in JET is presented. The JT-60U results show how the generic predictor described in chapter 5 could be adapted to a signal similar to the Locked Mode amplitude and with JET results, an in-depth analysis is presented including the first ever comparison between JET real-time protection system and the centroid method predictor.

6.1. JT-60U

JT60-U was the Japanese flagship tokamak before a new upgrade (JT-60SA) was proposed and approved for some ITER related studies. The centroid method predictor was tested on experimental discharges with high beta values [92]. The framework of the predictor remained unchanged and instead of the ML signal, a magnetic diagnostic signal called Magnetic Perturbation Time Derivative (MPTD) was used, which is sampled at 1 ms. The signal provides the amplitude of n=0 component of the saddle loop signal where n being the toroidal mode number. The reason behind usage of MPTD signal is that it is considered to provide a good gauging of an abrupt change of the plasma state- just like a disruption.

As shown in fig. 6.1 (c), the grouping of points representing plasma state is very concentrated in one single region. Here the x and y coordinates are obtained using the amplitude values of MPTD at time t and t-τ, which essentially means that a plasma state point P(x,y) has the current sample of MPTD as ordinate and the previous sample of MPTD as abscissa. Even though in fig. 6.1 (b) we could see some oscillations in the MPTD amplitude, the values are closely scattered evenly around 0 and hence, the plasma state points in fig. 6.1 (c) appear closely clustered around (0,0) point in our two dimensional parameter space.

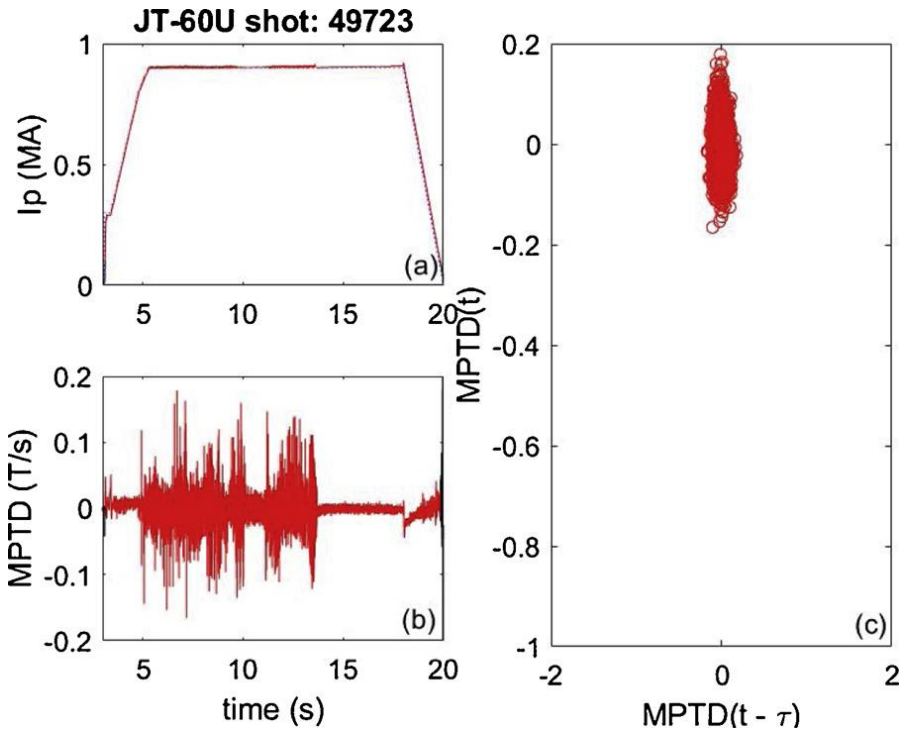

Figure 6.1: (a) Plasma current, (b) magnetic perturbation time derivative and (c) two dimensional parameter space for a non-disruptive discharge at JT60-U.

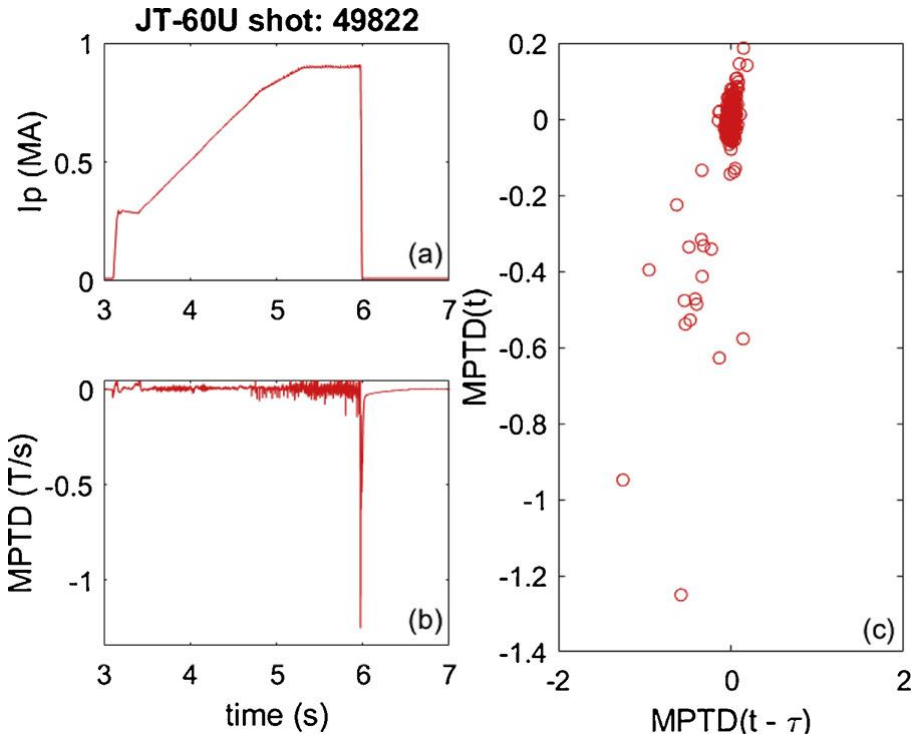

Figure 6.2: (a) Plasma current, (b) magnetic perturbation time derivative and (c) two dimensional parameter space for a disruptive discharge at JT60-U.

The difference between figures 6.1 (c) and 6.2 (c) is the scattering of the points representing plasma state. In case of a disruptive discharge (fig 6.2), the clustering of plasma state points is not very dense in a particular region, instead, there is a spread, indicating a change of behavior. Using this observation, information regarding disruptive and non-disruptive behavior of the plasma was compressed in two centroids, one each for disruptive and non-disruptive case. The non-disruptive centroid was very close to the point (0,0) whereas the disruptive centroid, was sufficiently far enough from its non-disruptive counterpart. As explained in chapter 5, the assignment of disruptivity label was done based on the Euclidean distance of the plasma state point P from either centroids. A linear separation hyperplane was obtained.

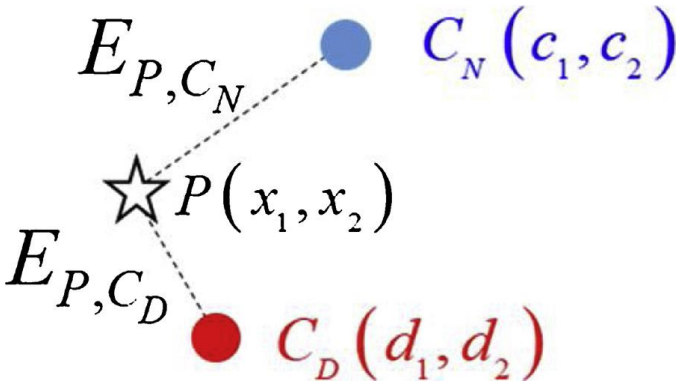

Figure 6.3: Plasma state point at each instance of the discharge is represented by point P. $E_{P,CN}$ and $E_{P,CD}$ are the Euclidean distances between P and centroids

The centroids were obtained using a dataset of training discharges keeping in mind the only condition to use data where the plasma current is above 0.1 MA during the discharge. In case of non-disruptive centroid determination, all the samples were split into pairs and hence, an even number of samples were required for each discharge. Only exception was made when for the last pair if there wasn't any sample of MPTD above 0.1 MA available, a solitary sample was used in chronological order to obtain the y coordinate of the plasma state point. The mean value of x and y coordinate of the collection of plasma state point provided the centroid for that particular non-disruptive discharge. The process was repeated for the whole training set of N non-disruptive discharges. Once obtained, all the N individual non-disruptive centroids were put together and another iteration of mean value calculation was carried out to procure the global

non-disruptive centroid, which as expected, turned out to be very close to the point (0,0) in the parameter space.

In case of the disruptive discharges, a time window of 20 ms around the disruption time was used to determine the coordinates of individual centroids. The sampling rate being 1 ms, the sample with the lowest amplitude of MPTD signal among the 20 selected samples, was chosen as the y coordinate and the sample previous to that sample was chosen as the x coordinate of the centroid. Again, the process was repeated for all N training discharges and the mean values of the x and y coordinates of those N individual centroids were used as global disruptive centroid.

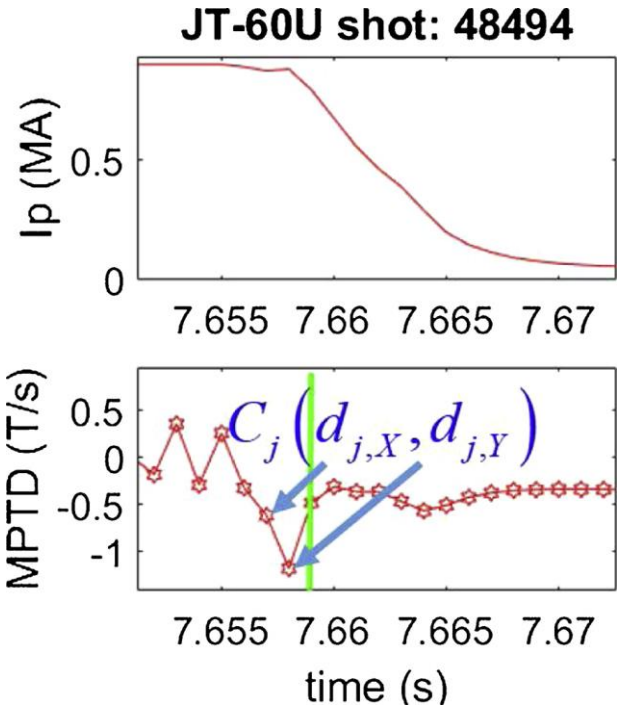

Figure 6.4: Illustration of how a disruptive centroid is selected. The green line represents the disruption time

The dataset of discharges tested with this predictor contained a total of 154 discharges, 76 of which were disruptive and 78 were non-disruptive. Two different approaches were used to assess the performance of the linear predictor where in the first approach, approximately 40% of disruptive and non-disruptive discharges were randomly chosen and used to train the predictor and using the centroids obtained, the remaining discharges were put to the classification test. In the other method, adaptive training from scratch was used as described in

chapter 4. For both the approaches, a necessary condition for alarm triggering was established in the sense of two consecutive plasma state points P_t and $P_{t-\tau}$ must appear in the disruptive region of the parameter space.

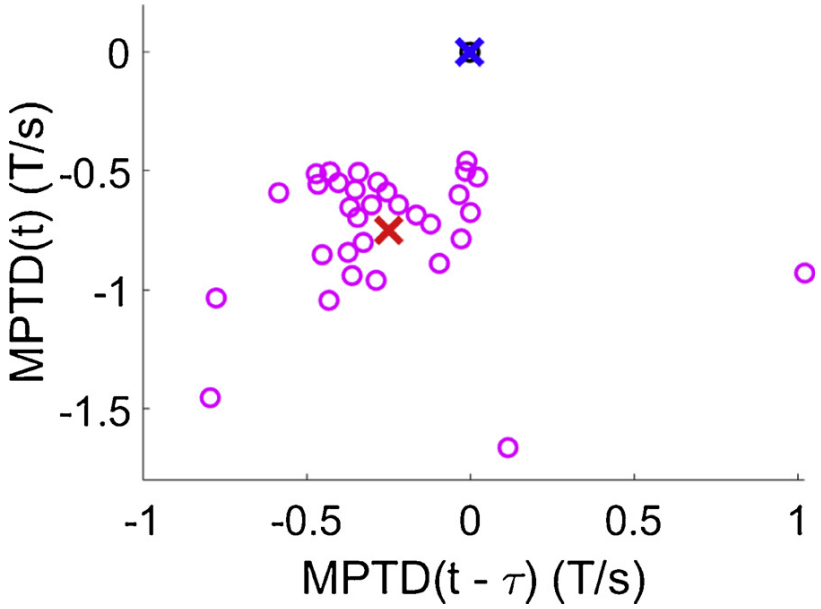

Figure 6.5: The red and blue crosses are respective global centroids for disruptive and non-disruptive discharges, the circles are individual centroids of training discharges

Using the centroids shown in figure 6.5, the equation defining disruptive behavior was obtained to be:

$$x_2 < -0.3300 \cdot x_1 - 0.4152$$

Several different training discharges were randomly chosen and tested with corresponding test discharges, resulting in highly encouraging detection rates with mean global success rate reaching 98.3%, the success rate with positive warning times as high as 95.4%, mean missed alarm rate being 1.7% and false alarm rate of 5.3% was achieved while obtaining an average warning time of 17 ms, meaning every detected disruption was recognized 17 ms prior to its occurrence on average. The warning time is an important parameter while assessing the performance of a predictor because it provides a measure of how the predictor can be utilized in terms of disruption handling. A very high average warning time would mean that the predictor is good enough to provide the operators sufficient time to change the discharge trajectory whereas a short warning time would only allow for actions to be taken that would minimize the harm done by a disruption.

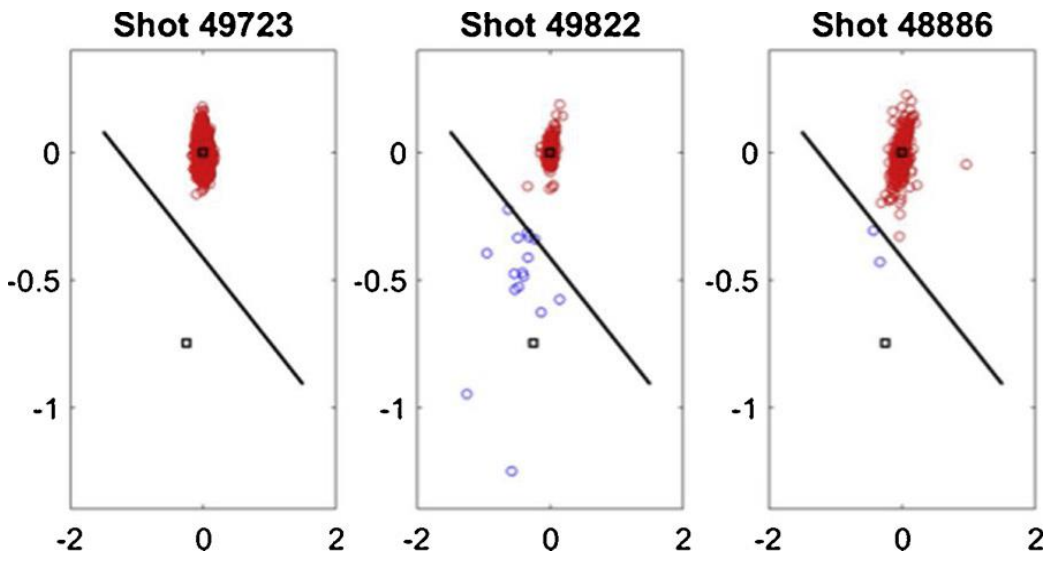

Figure 6.6: Illustrations of the parameter space for a non-disruptive (left), disruptive (center) and false alarm (right) case. The centroids are denoted by black squares.

In case of the alternative approach, the discharges were processed in a chronological order so that the predictor learns "on the go" about the disruptivity of the plasma- simulating a real time application scenario. The first predictor from scratch was obtained after the first disruption and for every missed alarm, re-training of the predictor was carried out to incorporate crucial information that the predictor would not have, causing it to miss a detection. The resultant predictor trained using such an approach used 1 disruptive and 2 non-disruptive discharges, provided a global success rate of 97.3% with positive success rate as high as 94.7% and a low missed alarm rate of 2.3%, missing only 2 alarms- requiring only 2 re-trainings [92]. The false alarm rate was considerably high, reaching 19.7% but this has to do with the high sensibility of the predictor towards disruptive behavior which in many cases, is present in a discharge but does not necessarily lead to a disruption and the discharge recovers and terminates without disrupting. This sensibility was also reflected in a comparatively higher average warning time of 59 ms, almost thrice that of a conventionally trained predictor. The linear equation for the predictor from scratch can be given by:

$$x_2 < -0.5580 \cdot x_1 - 0.3664$$

6.2. JET C38

The predictor was envisaged keeping in mind the ML signal and mode locking as a certain precursor to disruption and hence, it was only logical to test the predictor after its real-time implementation in JET. Previously, two different real time systems, namely APODIS and SPAD were developed and deployed in the JET RTN by CIEMAT and coworkers. However, this was the first time that comparison of a non-JET real time system was being made with all the constituents of the JET RTPS. The experimental campaign in focus was campaign C38- the penultimate campaign before the much anticipated DT campaign. As discussed in chapter 1, PETRA allows the scientists not only to choose from different experimental scenarios, it also allows them to modify conditions required to maintain a smooth operation of JET- the essential feature for machine safety. Different experimental scenarios in PETRA have preset safety measures programmed to be used by RTPS in order to prevent any undesirable, machine damaging experimental mishaps.

The PETRA feature providing constant machine safety is called the protection scenario. It contains several physics based predictors which are some of the most obvious indicators of plasma transitioning to a perilous state and entering the disruptive behavior. However, these predictors rely either on a threshold value, which upon surpassing for a certain duration of time in a continuous manner, would result in automated intervention of the RTPS or on fulfillment of a predefined condition for a chosen length of time during the course of the discharge. The protection scenario has two disruption mitigation alarms named PetraMit1 and PetraMit2 connected to different protection alarms as shown in table 6.1. The alarm trigger conditions are also given for reader's understanding. These trigger conditions can be modified depending upon the nature of the experiment at hand and are usually modified to make sure effective safety measures are in place for the case of an unexpected and unforeseen disruption.

Highlighted predictors in table 6.1 are the ones compared with the CM predictor. All the predictors mentioned in table 6.1 are always active for any operational discharge and have automated system interventions programmed. Any planned discharge with plasma current > 2 MA has disruption mitigation valve (DMV) enabled with RTPS and if any of the above mentioned system

raises an alarm, the DMV is triggered to inject massive amounts of gas to cool the plasma down to reduce the energy dump into the VV via disruption.

Mitigation alarm name	**Predictor Name**	**Trigger Condition**
Petramit1	LOCA	ML > 2 mT
	NRMLOCA	**ML/I_P > 400 pT/A for 20 ms continuously**
	CMBLV	Restraint ring loop voltage product > 500 V^2
	NRMCMBLV	**CMBLV/ I_P^2 > 50 V^2/A^2**
	SHRTDIDT	**Plasma current numerical derivative over 2 ms > 50 MA/s**
	LONGDIDT	**Plasma current numerical derivative over 16 ms > 7 MA/s**
Petramit2	VDE	From 40.05 s onwards, plasma vertical centroid numerical derivative (over 16 ms) > 10 m/s if an I_P derivative or restraint ring loop voltage type disruption has not been detected in the last 50 ms

Table 6.1: PETRA Protection scenario predictors

The C38 in JET took place between June 2019 and June 2020. Thousands of experimental discharges were made during this period for different experiments. After careful filtering, a database of 1544 discharges was obtained out of which 1091 were non disruptive discharges and 460 discharges were disruptive. Note should be made of the fact that no training was required in this case since the CM predictor was already implemented in the JET real-time network and was collecting data, the only difference was that it was not connected to any mitigation alarms. Also worth mentioning is the fact that in this dataset, only unintentional disruptions were considered since there are experiments to study the effects of disruptions and for that, disruptions are provoked intentionally.

The 453 disruptive discharges used for the performance analysis of CM predictor during C38 included experimental shots from different scenarios.

Special focus was put on the **Baseline** and **Hybrid** scenario experiments. These scenarios are two of the most important for JET as they are preparatory sessions of ITER operation. Both the scenarios are envisaged for testing different operational capabilities to arrive at a stationary scenario which could be suitable for sustained high DT fusion power. Baseline scenario aims for operations at high plasma current and magnetic field limits while keeping the current profile relaxed. Hybrid scenario focuses on operation at high beta values and shaped current profiles. As shown by Garzotti [93], the baseline scenario showed improved particle confinement whereas the hybrid scenario demonstrated a better efficiency of stored energy conversion into fusion power. Details of operational parameters set for the JET DTE campaign of both baseline and hybrid scenarios are given in table 6.2.

Parameter	**Baseline Scenario**	**Hybrid Scenario**
Plasma current $\mathbf{I_P}$ (A)	3.8-4.5	2.2-2.5/2.5-2.9
Toroidal magnetic field $\mathbf{B_T}$ (T)	3.45-3.7	2.8/3.4
Auxiliary heating power $\mathbf{P_{aux}}$ (MW)	42	42
Fusion power $\mathbf{P_{fus}}$ (MW)	15	15
Fusion energy $\mathbf{W_{fus}}$ (MJ)	75	75

Table 6.2: Baseline and hybrid scenario parameters [93]

6.2.1.CM predictor detection rates

In this section, a detailed discussion of the performance of CM predictor is presented. Parameters used for assessing the performance are the detection rates and warning time. An ideal predictor obtains very high success rates while minimizing the false alarms without compromising on the warning times. In JET, since the RTPS system is capable of intervention and the minimum time required for allowing the system intervention being 10 ms, alarms detected with warning times less than 10 ms are categorized as tardy alarms. Detection rates of the complete dataset are given in table 6.3.

Parameter	**Value**
Successful alarm rate	98.9 %
Missed alarm rate	1.1 %
False alarm rate	15.21 %
Average $T_{warning}$	172 ms

Table 6.3: CM predictor performance for the complete database of C38

The successful alarm rate in table 6.3 includes tardy alarms as well. The successful alarm rate with warning time greater than 10 ms is 77.9% and the successful alarm rate with warning time less than 10 ms is 20.9%. The average positive $T_{warning}$ is 225 ms whereas the average negative $T_{warning}$ is -25 ms. Here, the negative warning time means that the disruption was detected after it had already occurred. As can be seen in figure 6.7, the number of detections with $T_{warning} > 2$ s is very low and hence, the CM predictor emphasizes the potential usability as a mitigation predictor.

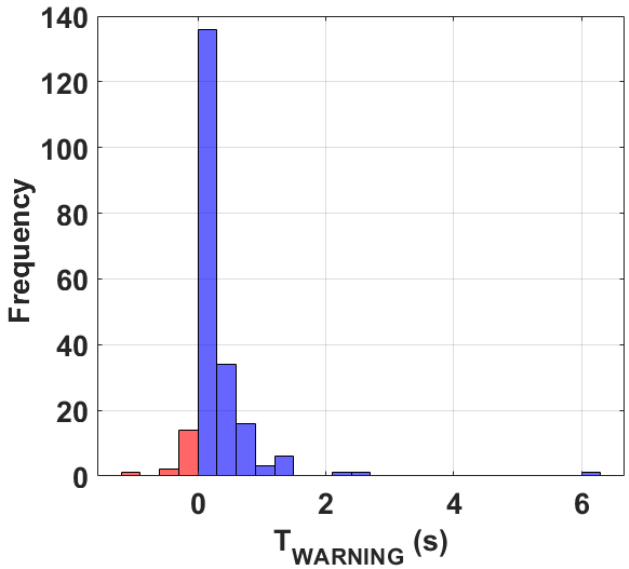

Figure 6.7: Warning times of the complete database of C38 for the CM predictor. The bars in red show detections post disruption.

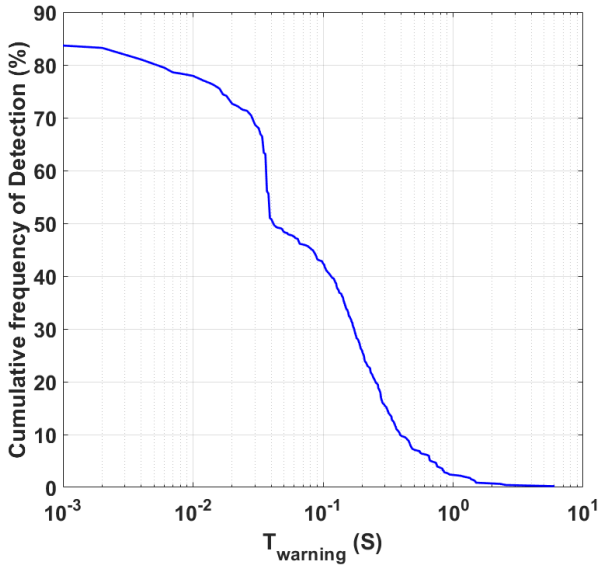

Figure 6.8: Cumulative frequency of detections as a function of $T_{warning}$ for all the detections.

Even though figure 6.7 provides a general outlook on $T_{warning}$, a better insight on the can be had through figure 4.8, where the cumulative fraction of successful detections is plotted as a function of $T_{warning}$. The semilog x-axis would suppress the contribution corresponding to $T_{warning} < 0$ s and hence, only the warning times > 10 ms are reflected in figure 6.8.

6.2.2.NRMLOCA predictor detection rates

The NRMLOCA predictor has been an integral part of the PetraMit1 and PETRA protection scenario. As discussed in chapter 3, it uses the exact same signals as the CM predictor, ML amplitude normalized to the plasma current. There is, however, a key difference in the operational functionality of both of them. If CM predictor has a unique pre-defined separation hyperplane with slope and intercept values for all type of experiments, the NRMLOCA works on a rather simple yet disadvantageous principle of using a threshold value. The threshold value not only needs to be crossed but also, the plasma needs to remain in the disruptive zone for at least 20 ms, otherwise, the alarm is not raised. Figure 6.9 shows the parameter space with the most commonly used threshold value for NRMLOCA.

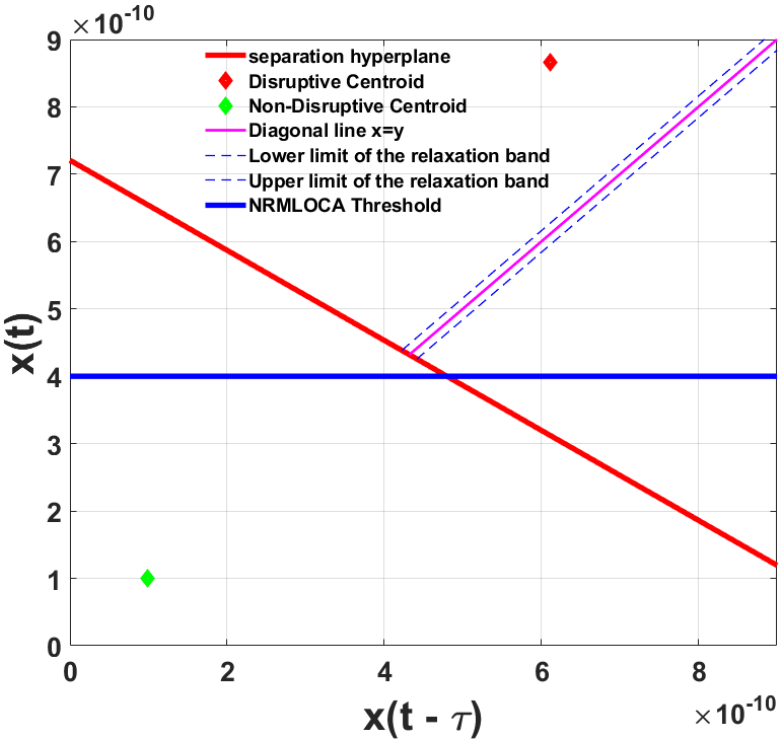

Figure 6.9: Combined parameter space for CM predictor and NRMLOCA.

Detection rates and warning times for NRMLOCA are given in table 6.4. It is most notable that the price paid for a 100% detection rate is a very high false alarm rate, also reaching ~100%. For any predictor, the most important evaluation parameter is the combination of high successful alarm rate and a very low false alarm rate- a criterion NRMLOCA clearly fails to fulfill. Furthermore only 65.12% of successful detections were made for $T_{warning} > 10$ ms with the remaining 34.88% detections being tardy detections. Also, the average $T_{warning}$ values is skewed to be higher than 100 ms due to the presence of an outlier (see fig. 6.10), a premature detection with a warning time of ~25 s. Removal of that outlier, brings down the average warning time to 72 ms, which is exactly 100 ms smaller compared to the CM predictor.

Parameter	**Value**
Successful alarm rate	100 %
Missed alarm rate	0 %
False alarm rate	99.91 %
Average $T_{warning}$	127 ms

Table 6.4: NRMLOCA predictor performance for the complete database of C38

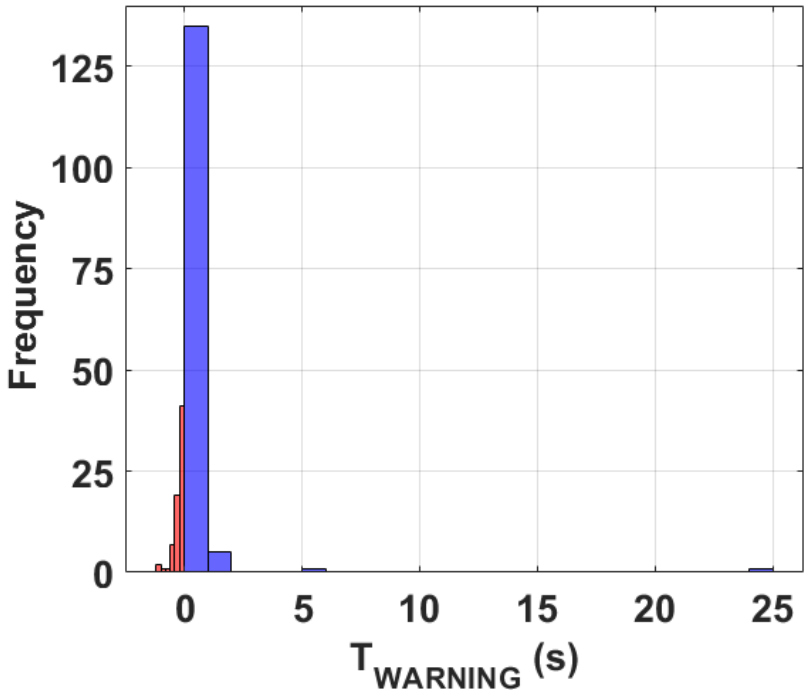

Figure 6.10: Warning times of the complete database of C38 for the NRMLOCA predictor. The bars in red show detections post disruption.

6.2.3.NRMCMBLV predictor detection rates

NRMCMBLV uses the product of restraint ring loop voltage normalized to plasma current for detection of possible disruptive behavior of the plasma. It also uses a static threshold value to classify plasma states and the default value for raising an alarm is NRMCMBLV > 50 pV^2/A^2. The performance on the complete dataset is summarized in table 6.5. Once again, it is clearly visible that the predictor obtains a 100% successful detection rate but also, the false alarm rate is $\sim$ 100%, rendering the predictor not usable for reliable plasma safety application owing to the fact that if for every discharge, an alarm is raised, the operators will never be able to push the plasma to the high performance mode and actually do experiments to study and understand the plasma in desired conditions, something very essential to the purpose of ITER.

Parameter	**Value**
Successful alarm rate	100 %
Missed alarm rate	0 %
False alarm rate	99.91 %
Average $T_{warning}$	870 ms

Table 6.5: NRMCMBLV predictor performance for the completeC38 database

Worth highlighting is the fact that out of 100% successful detections, 70.2% are tardy detections, meaning that even if the disruptions were detected, there was not sufficient time to allow the RTPS to react and alleviate the effects of the eventual disruption. Also, the staggeringly high average $T_{warning}$ is caused by several premature detections as shown in figure 6.11 (a). As many as 30 detections were made with warning times greater than 6 s, out of which, 25 have warning times in excess of 10 s. If all these 30 outliers are removed, the average warning time falls down to 47 ms, worse than NRMCMBLV and ~120 ms lower than the average $T_{warning}$ for the CM predictor. Figure 6.11 (b) shows the distribution of $T_{warning}$ for 30 outliers mentioned above.

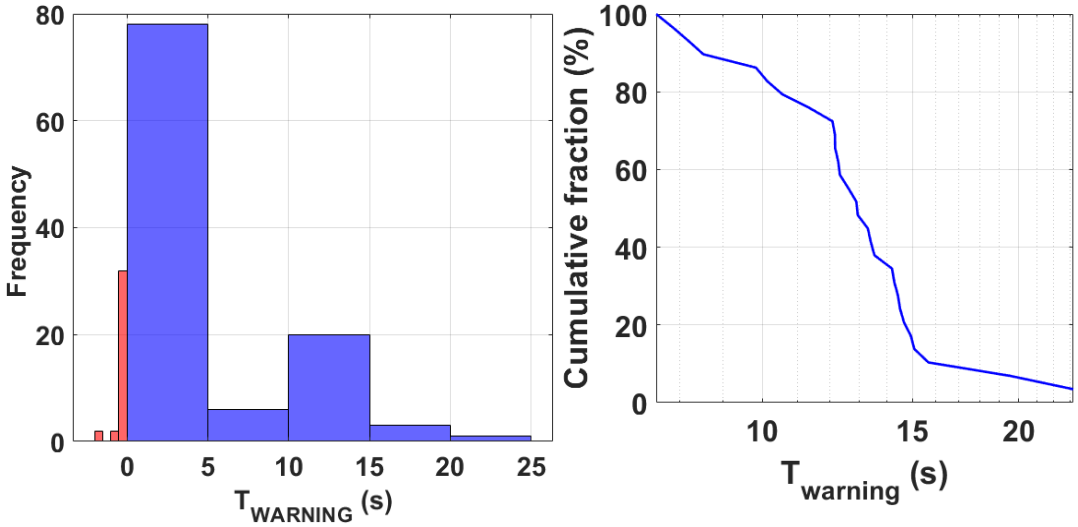

Figure 6.11: Warning times of the complete database of C38 for the NRMCMBLV predictor.

6.2.4. I_P time derivative predictor detection rates

Both the SHRTDIDT and LONGDIDT predictors are based on detection of variation of plasma current over 2 ms and 16 ms respectively. The main reason behind using such a detector for protection scenarios is that nearing a disruption, the loss of plasma equilibrium results in changes in magnetic field configuration which is reflected via variations in plasma current and vice versa is also possible. Both SHRTDIDT and LONGDIDT also rely on threshold values for disruptivity detection. Usually, in case of SHRTDIDT, the value has to be greater than 50 MA/s for 10 ms whereas for LONGDIDT, the value for triggering an alarm is 7 MA/s for 10 ms. Here again, the primary concern is not only the strong reliance on hard threshold to be fulfilled but also, the fulfillment of these thresholds for a given duration of time, which in case of JET, is the minimum time window required for actuators to respond for mitigation. The parameters are given in tables 6.6 and 6.7 with histograms for warning times in figures 6.12.

Parameter	Value
Successful alarm rate	94.7 %
Missed alarm rate	5.3 %
False alarm rate	10%
Average $T_{warning}$	12 ms

Table 6.6: SHRTDIDT predictor performance for the complete C38 database

As shown in table 6.6, the SHRTDID has a lower false alarm rate compared to the CM predictor, NRMLOCA and NRMCMBLV. However, the high successful detection rate needs to be further analyzed as in the case of previously discussed predictors. Out of 94.7% successful detections, only 18.54% detections were made with a warning time in excess of 10 ms, rest 76.16% of successful detections were made with less than 10 ms warning time. In fact, there is only one discharge where an upcoming disruption was detected 6 s in advance, which affects the average warning time of the complete database immensely. Upon considering the particular discharge with 6 s of $T_{warning}$ an outlier, the average warning time for SHRTDIDT reduces down to -1 ms, which means that SHRTDIDT detected disruptions just after their occurrences- failing in the very duty it is desigdned to be used for. Figure 6.12 shows tendencies of warning times for SHRTDIDT where 6.12 (a) demonstrates the overall distribution of the warning times and 6.12 (b) gives a better insight into the warning times inferior to 10 ms.

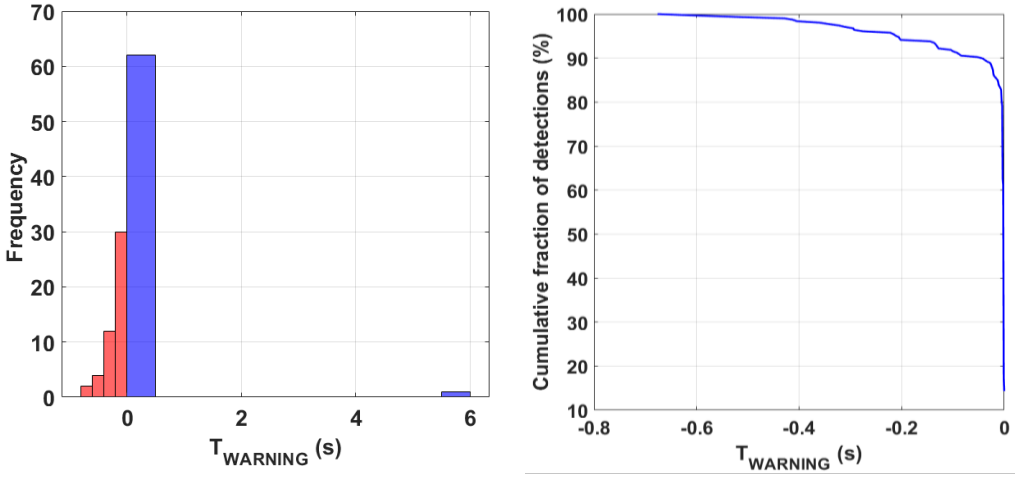

Figure 6.12: Warning times of the complete database C38 for SHRTDIDT.

For LONGDIDT, even though the false alarm rate is better compared to NRMLOCA and NRMCMBLV, the detector still has a scope for improvement mainly because out of the 98% successful detections, 84% are tardy detections, with warning times less than 10 ms. So, the effective successful detection rate falls down to a mere 14%, which is lower than the false alarm rate. The average warning time is also affected by a solitary detection with warning time of 6s just like in the case of SHRTDIDT as shown in figure 6.13 (a). Removal of the outlier brings the average $T_{warning}$ down to -13 ms, meaning that most of the disruptions

were detected after their occurrence. Figure 6.13 (b) represents the overall distribution of warning times inferior to 10 ms.

Parameter	Value
Successful alarm rate	98 %
Missed alarm rate	2 %
False alarm rate	23.37%
Average $T_{warning}$	550 µs

Table 6.7: LONGDIDT predictor performance for the complete database C38

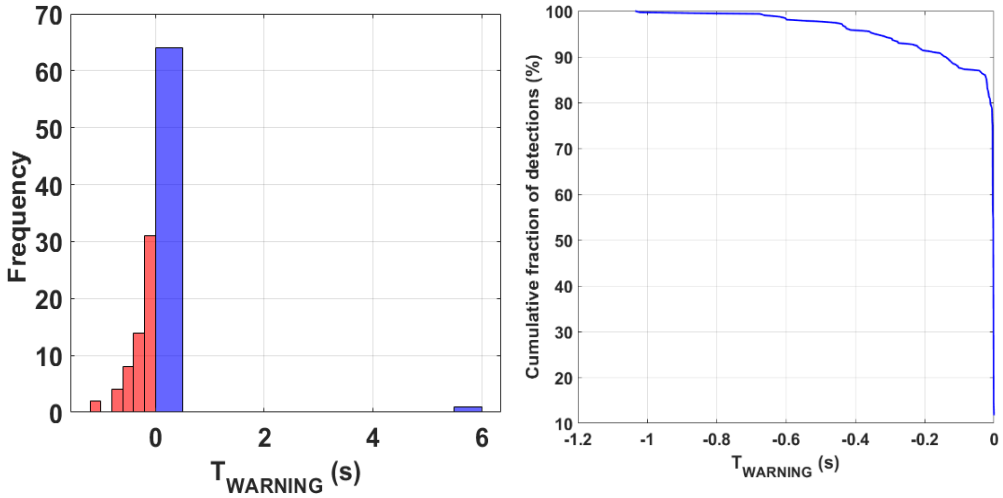

Figure 6.13: Warning times of the complete database C38 for the LONGDIDT.

Comparing both the I_P time derivative predictors, the similarities in results is rather obvious. The working principle for both the predictor is identical and the only difference is the necessary duration of fulfillment of the threshold condition and the values of the threshold. These detectors have a much better performance compared to NRMLOCA and NRMCMBLV in terms of false alarms but negative warning times (after the removal of solitary outlier for both SHRTDIDT and LONGDIDT) leave much to be desired from these predictors for their use in machine safety department for ITER and subsequent ITER class tokamaks. Detecting disruptions while they are occurring is not ideal.

6.2.5.Baseline and hybrid scenario comparison

A direct comparison of performances of all the detectors summarized is sections 6.2.1-6.2.4 is presented in this section with special focus on the baseline and hybrid scenario experiments made during C38 campaign in JET. A total of 424 discharges are included, out of which 78 are disruptive and rest 346 non-disruptive. The 78 disruptive discharges are further divided according to the experimental scenario, 53 of them belonging to the baseline scenario and the **remaining** 25 to the hybrid scenario.

As reflected in table 6.8 the CM predictor has better results in terms of high success rate with positive warning times. Care must be taken in interpreting the false detection rates, owing to the fact that whenever an event is detected by any of the PetraMit1 constituent, RTPS of JET takes immediate action to terminate the discharge. In table 6.9, we compare the average warning times and their standard deviation. Here again, the CM predictor outperforms NRMLOCA, SHRTDIDT and LONGDIDT predictors. Actually, the NRMCMBLV is also worse than the CM predictor but a couple of premature detections inflate the average $T_{warning}$ value as can be observed considering the standard deviation of the same.

Detector	**Success Rate (%)**	**Success Rate with positive $T_{warning}$ (%)**	**Success Rate with negative $T_{warning}$ (%)**	**Missed Rate (%)**
CM	96.16	84.62	11.54	3.84
NRMLOCA	100	69.23	30.77	0
NRMCMBLV	100	61.54	38.46	0
SHRTDIDT	97.5	52.5	45.00	2.5
LONGDIDT	100	43.59	56.41	0

Table 6.8: Comparison of detection rates for different detectors comprising PetraMit1

The analysis, comparing the alarm times of several detectors with the ones of CM predictor, has produced some interesting results. Here, a clarification is appropriate- the term alarm time is defined as the first instance a predictor detects an upcoming disruption for each discharge. Mathematically, $\Delta T = T_{SIGNAL} - T_{CM}$, where T_{SIGNAL} is the alarm time for a particular detector and T_{CM} is the

alarm time for the CM predictor. Tables 6.10 and 6.11 present comparisons of ΔT values as well as the percentage of alarms detected by the CM predictor earlier than those of the detectors in PetraMit1 for both BS and HS experiments.

Detector	**Avg $T_{warning}$ (ms)**	**σ $T_{warning}$ (ms)**
CM	117	204
NRMLOCA	38	210
NRMCMBLV	546	1635
SHRTDIDT	-5	55
LONGDIDT	-16	77

Table 6.9: Comparison of warning times for different detectors comprising PetraMit1

Detector	**Avg $T_{warning}$ (ms)**	**$(Avg\ T_{warning})_{CM} - (Avg\ T_{warning})_{DETECTOR}$ (ms)**	**Disruptions detected in advance (%)**
CM	108	0	100
NRMLOCA	80	28	83.87
NRMCMBLV	-3	111	87.1
SHRTDIDT	-7	115	90.3
LONGDIDT	-7	115	93.55

Table 6.10: Here in fourth column, we present the percentage of disruptions detected by CM predictor before any other system of PetraMit1 for baseline scenario experiments.

Detector	**Avg $T_{warning}$ (ms)**	**$(Avg\ T_{warning})_{CM} - (Avg\ T_{warning})_{DETECTOR}$ (ms)**	**Disruptions detected in advance (%)**
CM	126	0	100
NRMLOCA	-4	130	80
NRMCMBLV	1095	-969	70
SHRTDIDT	-3	129	80
LONGDIDT	-25	151	80

Table 6.11: Percentage of disruptions detected by CM predictor before any other system of PetraMit1 for hybrid scenario experiments.

AVERAGE	CM	NRM LOCA	NRMCMBLV	SHRT DIDT	LONG DIDT
Positive $T_{warning}$ (ms)	33	18	4	0	0
Negative $T_{warning}$ (ms)	-31	-55	-17	-17	-18

Table 6.12: Comparison of average $T_{warning}$ for baseline scenario experiments.

In tables 6.12 and 6.13 we present a comparison between positive and negative warning times for both baseline and hybrid scenario. Apart from being the predictor with least number of negative $T_{warning}$ detections, the CM predictor has the smallest average value for the same – a demonstration of efficiency of detections.

AVERAGE	CM	NRM LOCA	NRMCMBLV	SHRT DIDT	LONG DIDT
Positive $T_{warning}$ (ms)	21	16	4818	0	18
Negative $T_{warning}$ (ms)	-65	-182	-98	-89	-98

Table 6.13: Comparison of average $T_{warning}$ for hybrid scenario experiments.

Again, it is important to stress on the fact that, for a vast majority of discharges, the CM predictor does detect the incoming disruptions well in advance of the minimum time interval required to undertake mitigation actions. In the next section we discuss the performance with regards to the vessel force.

6.2.6. Vessel Forces

Disruptions result in large amounts of dynamic vessel forces in big devices. In tokamaks such as JET, where the plasma cross-section is elongated, a routinely observed phenomenon is the vertical displacement of plasma centroid. This displacement results due to the loss of plasma position control, often caused by several different instabilities. Hence, the volume of the plasma moves upwards or downwards with reference to the VV, eventually making contact with material

surfaces. Such movement leads to a reduction of plasma volume, without a significant change in the plasma current. When the plasma makes contact with VV walls, currents start flowing through the vessel walls, famously known as the 'halo currents' (I_H). Apart from the halo currents, the other type of currents arising in the VV structures, due to the movement of the plasma, are the eddy currents, which contrary to the halo currents, complete their full path in the structures. A current density can be associated with these in-vessel currents ($\mathbf{j}_{\text{in-vessel}}$) and the interaction of these currents with the magnetic field produces $\mathbf{j}_{\text{in-vessel}} \times \mathbf{B}$ forces on vessel components. As per [94], the overall force caused on VV components by a disruption can be estimated using,

$$F_d = f_d 2\pi a_w I_p B_0$$

with $2\pi a_w$ being the poloidal circumference of the plasma chamber wall, I_p is the net plasma current, B_0 is the magnetic field and f_d is a dimensionless coefficient. However, in JET and other tokamaks, F_d/I_p^2 is used to evaluate the experimental observations, since only a fraction of plasma current ends up flowing through the VV structures. The forces produced by these currents can be of swing or roll type, causing significant structural and mechanical stresses to the VV [95]. In JET, the operational protocols demand a simulation of the planned discharge with operational parameters, to obtain a prediction of the vessel force (F_P) produced in the event of a disruption.

It was interesting to obtain and compare the amplitude of the vessel forces at T_{SIGNAL} for the various predictors. As can be seen in figure 6.14, the mean and standard deviation values of F_P for the CM predictor are notably higher compared to the other predictors. Especially, the values compared with detection times for NRMLOCA (see fig. 6.15) are of importance due to the recurring mention of both the predictors using the same disruption precursor for forecasting- the mode locking phenomenon. Of course detections made at higher values of vessel forces justify to react promptly and take appropriate mitigation action to minimize the disruption consequences. As per Lehnen [96] and de Vries [35], the forces thus produced by the halo currents are not only dependent on the ratio of I_H/I_P but also, on the duration for which the halo current is flowing through the VV.

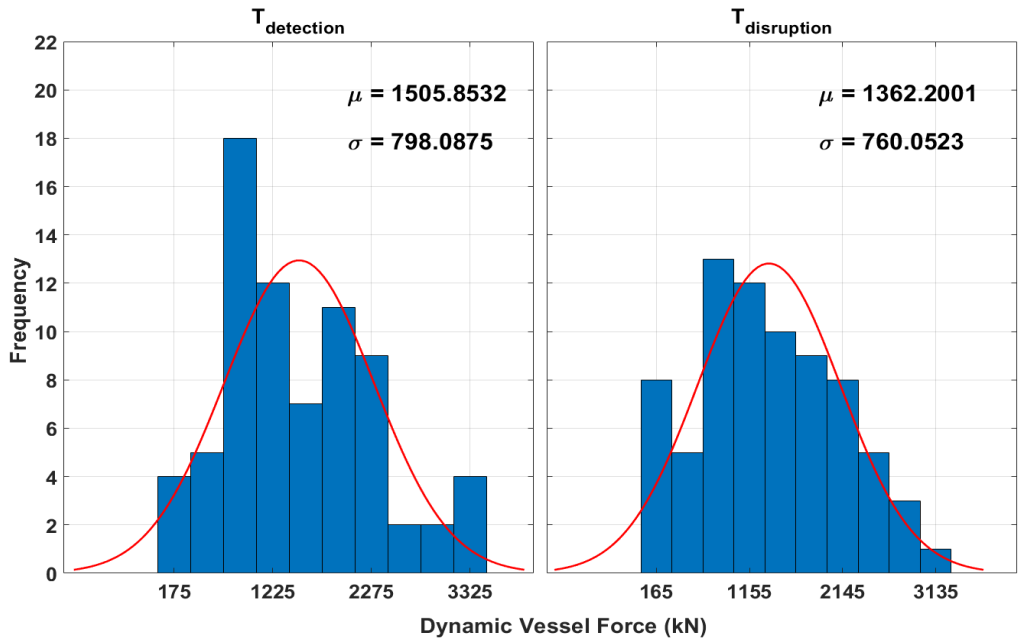

Figure 6.14: A direct comparison of values of F_P at $T_{detection}$ and $T_{disruption}$ for CM predictor.

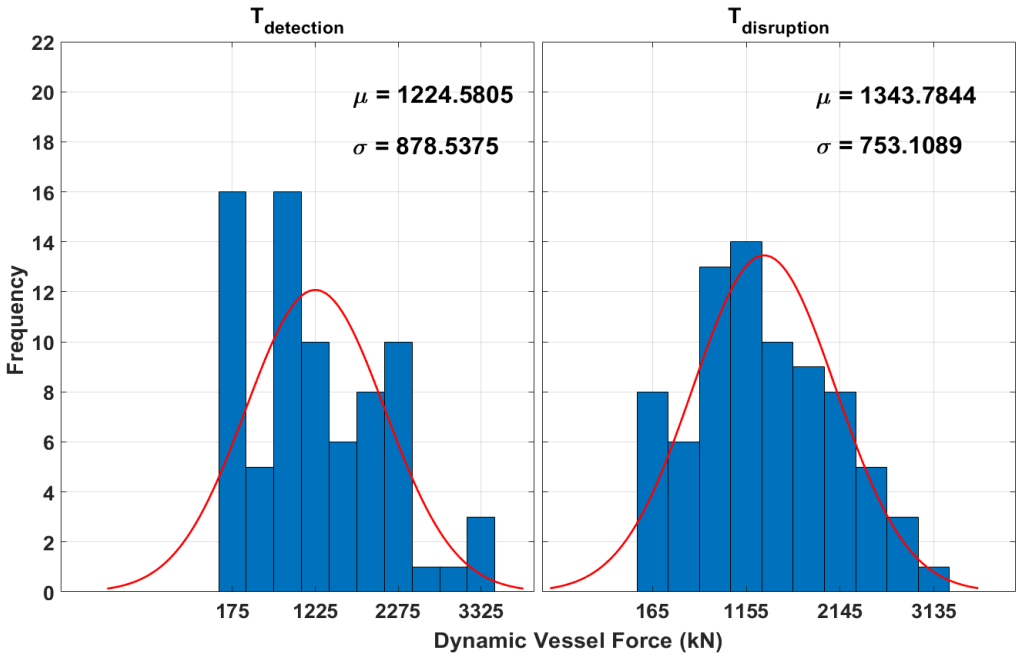

Figure 6.15: A direct comparison of values of F_P at $T_{detection}$ and $T_{disruption}$ for NRMLOCA

The JET vessel characteristic time ~714 ms [33] being longer than the duration of majority disruptions, the reaction of VV to this force can be compared to a spring system, which would create a damping effect on oscillations caused by the dynamic forces on VV. For a mass-damper-string system, the displacement is directly proportional to the force provided the force is applied continuously or

for much longer than the natural frequency of the spring- the JET vessel for our toy model. Using the simple analogy of the concept of instantaneous impulse, where **F**.dt is dependent mainly on the force, even for a shorter duration- one cannot deny the possibility of experiencing much larger displacements just because of resonance between two systems. So, ideally, one should aim at avoiding disruptions at higher force values. The advantage of CM predictor making detections at higher values of F_P is the fact that it allows us to regulate the value of I_P- the most influential quantity on the resultant vessel forces. In addition, the detections are made before the rest of the PetraMit1 predictors as depicted in figure 6.16.

All the disruptions detected by the CM predictor went on to exhibit VDE. In JET, the disruptions have been identified to be accompanied by toroidal variation of the plasma current [97]. Combination of this toroidal variation and occurrence of VDEs amounts for a majority of electromagnetic loads produced on VV during and after a disruption. Moreover, different classes of VDEs and asymmetries in plasma current variation further result in different types of movement of the VV [98-100]. The CM predictor, detecting disruptions in advance as summarized in previous sections, can provide crucial time to react and if possible, prevent the occurrence of such VDEs. On average, for all the 75 detected disruptions of our database, the CM predictor raised alarms of an upcoming disruption 265 ms before there was a VDE detected.

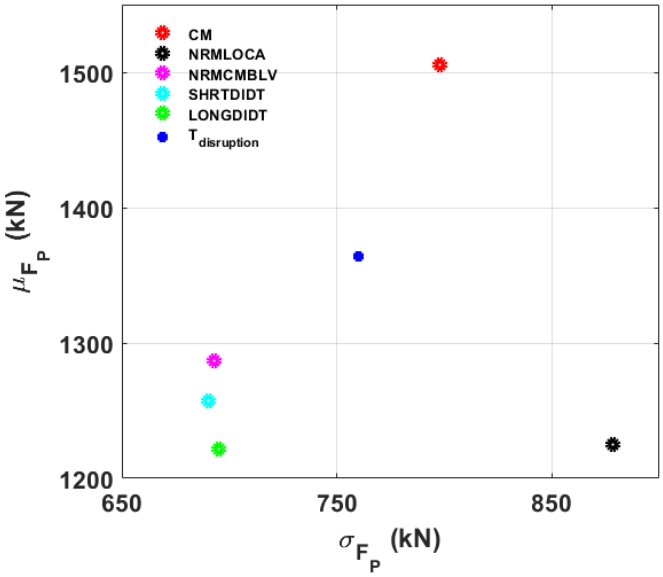

Figure 6.16. A comparison of mean and standard deviation values of F_P at $T_{detection}$ and $T_{disruption}$ between different predictors.

6.3. JET C39

The C39 in JET was a rather short tritium preparation campaign which took place between October-December 2020. Approximately 300 experimental discharges were made during this period mainly for the upcoming DT campaign in 2021. After careful filtering, a database of 279 discharges was obtained out of which 250 were non disruptive discharges and 29 discharges were disruptive. Once again, it is important to highlight that no training was required in this case since the CM predictor was already implemented in the JET real-time network and was collecting data

The 29 disruptive discharges used for the performance analysis of CM predictor during C39 included experimental shots from different scenarios except the **baseline** and **hybrid** scenario experiments. Since C39 was carried out to prepare JET for upcoming DT campaigns, main experiments carried out in C39 involved usage of Tritium. Also a dedicated set of experiments towards runaway electrons was executed, which produced a several disruptive discharges but since these disruptions are expected and in some cases, even intentionally provoked, the disruptive discharges from runaway electrons experiment were consciously ignored from the database for the performance analysis of the CM predictor.

6.3.1. CM predictor detection rates

Similar to section 6.2.1, parameters used for assessing the performance are the detection rates and warning time. Detection rates of the dataset are given in table 6.14.

Parameter	Value
Successful alarm rate	100 %
Missed alarm rate	0 %
False alarm rate	2 %
Average $T_{warning}$	172 ms

Table 6.14: CM predictor performance for the complete database of C39

Tardy alarms are also included in the computation of successful alarm rate in table 6.14. The successful alarm rate with warning time greater than 10 ms is 96.56% and the successful alarm rate with warning time less than 10 ms is 3.44%. The average positive $T_{warning}$ is 165 ms and all the disruptions were

detected before their actual occurrence. Hence, the negative $T_{warning}$ is a redundant quantity for CM predictor in C39.

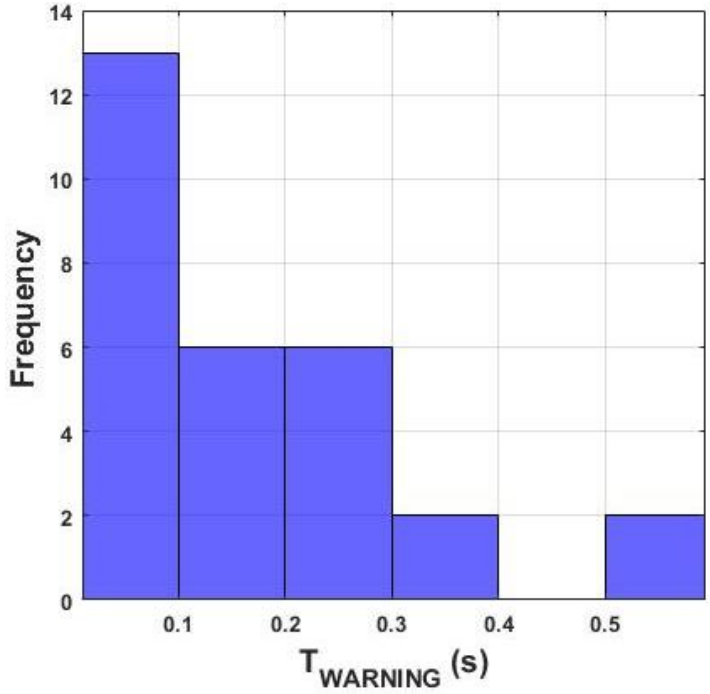

Figure 6.17: Warning times of C39 for the CM predictor.

Even though figure 6.17 provides a general outlook on $T_{warning}$, figure 6.18 is more useful to assess the performance of the CM predictor in C39.

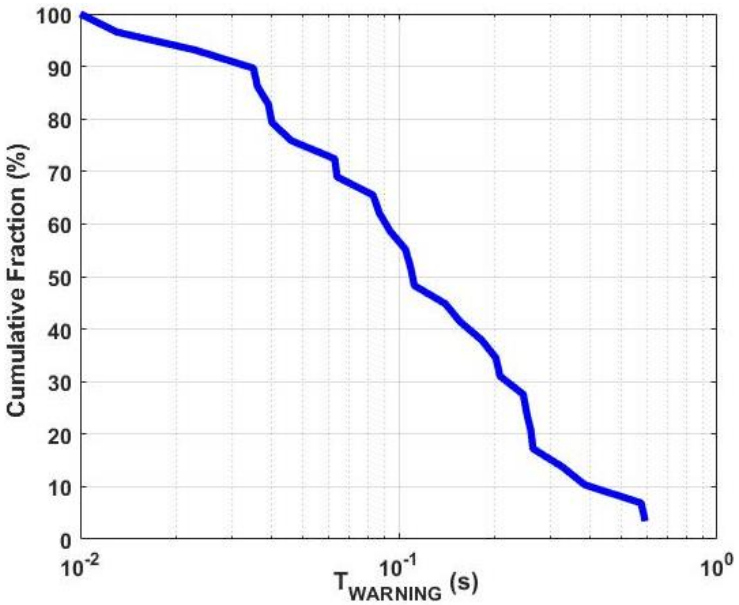

Figure 6.18: Cumulative frequency of detections as a function of $T_{warning}$ for all the detections made with at least 10 ms of reaction time.

6.3.2.NRMLOCA predictor detection rates

Detection rates and warning times for NRMLOCA are given in table 6.15. The successful detection rate is identical to the CM predictor but as in the case of C38, the false alarm rate is 100%- rendering the feasibility of the detector questionable. The average warning time for NRMLOCA is 139 ms, smaller compared to the CM predictor by a margin of 33 ms- a duration of time which could prove crucial for a disruption handling scenario.

Parameter	Value
Successful alarm rate	100 %
Missed alarm rate	0 %
False alarm rate	100 %
Average $T_{warning}$	139 ms

Table 6.15: NRMLOCA predictor performance for C39

Figure 6.19 represents the warning times in form of histogram and cumulative fraction form. The similarity of successful detection rates between CM predictor and NRMLOCA predictor can be clearly depicted in figures 6.18 and 6.19.

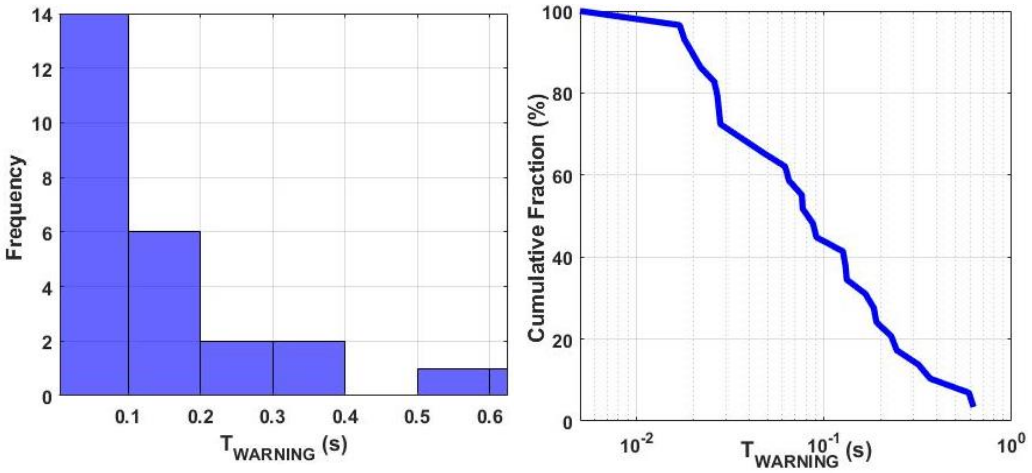

Figure 6.19: Warning times of C39 for the NRMLOCA predictor. There are no bars in red, which means there are no detections post disruption.

6.3.3.NRMCMBLV predictor detection rates

The performance of NRMCMBLV predictor for C39 dataset is summarized in table 6.16. Just like NRMLOCA, the predictor obtains a 100% successful detection rate but also, the false alarm rate is 100%, which would mean that if the predictor is used actively for the device protection, practically every discharge would raise an alarm- inhibiting the operator from continuing the discharge towards achieving the scientific goal of the experiment.

Parameter	Value
Successful alarm rate	100 %
Missed alarm rate	0 %
False alarm rate	100 %
Average $T_{warning}$	833 ms

Table 6.16: NRMCMBLV predictor performance for C39

Worth highlighting is the fact that out of 100% successful detections, 82.76% are tardy detections, meaning that even if the disruptions were detected, there was not sufficient time to allow the RTPS to react and alleviate the effects of the eventual disruption. Also, the staggeringly high average $T_{warning}$ is caused by several premature detections as shown in figure 6.20 (a). A detection with a warning time ~16 s and another one of the order of ~8 s inflates the average warning time. If these 2 outliers are removed, the average warning time falls down to mere 7 ms, worse than NRMLOCA and ~165 ms lower than the average $T_{warning}$ for the CM predictor. Figure 6.20 (b) depicts the tendency of $T_{warning}$ for NRMCMBLV.

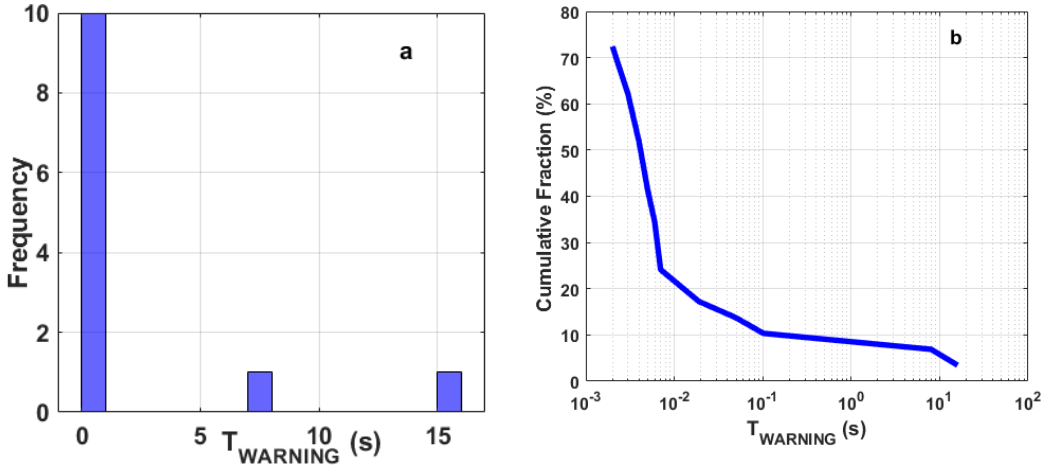

Figure 6.20: Warning times of the complete database of C39 for the NRMCMBLV predictor.

6.3.4. I_P time derivative (SHRTDIDT and LONGDIDT)

As demonstrated in table 6.17, the SHRTDID has a lower false alarm rate compared to NRMLOCA and NRMCMBLV but it is worse compared to the CM predictor. However, the high successful detection rate needs to be further analyzed as in the case of previously discussed predictors. Out of 100% successful detections, only 6.9% detections were made with a warning time in excess of 10 ms, rest 93.1% of detections were made with less than 10 ms warning time.

Parameter	Value
Successful alarm rate	100 %
Missed alarm rate	0 %
False alarm rate	7.2%
Average $T_{warning}$	4 ms

Table 6.17: SHRTDIDT predictor performance for C39

Unlike C38, there is no outlier for SHRTDIDT and hence, the average warning time listed in table 6.17 is absolute. Figure 6.21 shows tendencies of warning times for SHRTDIDT where 6.21 (a) demonstrates the overall distribution of the warning times and 6.21 (b) gives a better insight into the warning times inferior to 10 ms.

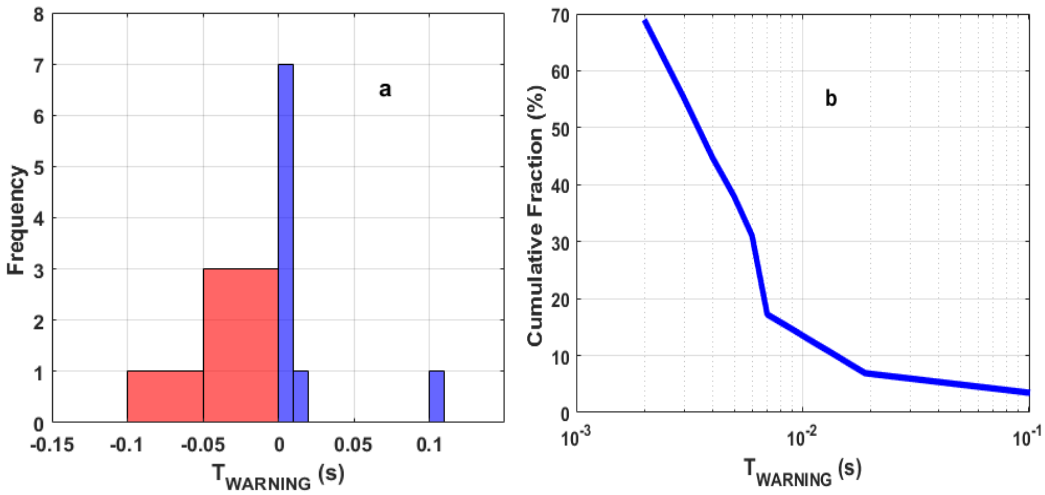

Figure 6.21: Warning times of the complete database of C39 for the SHRTDIDT predictor.

Parameter	Value
Successful alarm rate	100 %
Missed alarm rate	0 %
False alarm rate	23.6%
Average $T_{warning}$	7 ms

Table 6.18: LONGDIDT predictor performance for C39

Similar to C38, LONGDIDT shows that even though the false alarm rate is better compared to NRMLOCA and NRMCMBLV, the detector still has a scope for improvement mainly because out of the 100% successful detections, 96.6% are tardy detections, with warning times less than 10 ms. So, the effective successful detection rate falls down to a tame 3.5%, which is lower than the false alarm rate. Similar to SHRTDIDT, the absence of outliers means that the average warning time given in table 6.18 is an absolute value. Figure 6.22 (b) represents the overall distribution of warning times inferior to 10 ms.

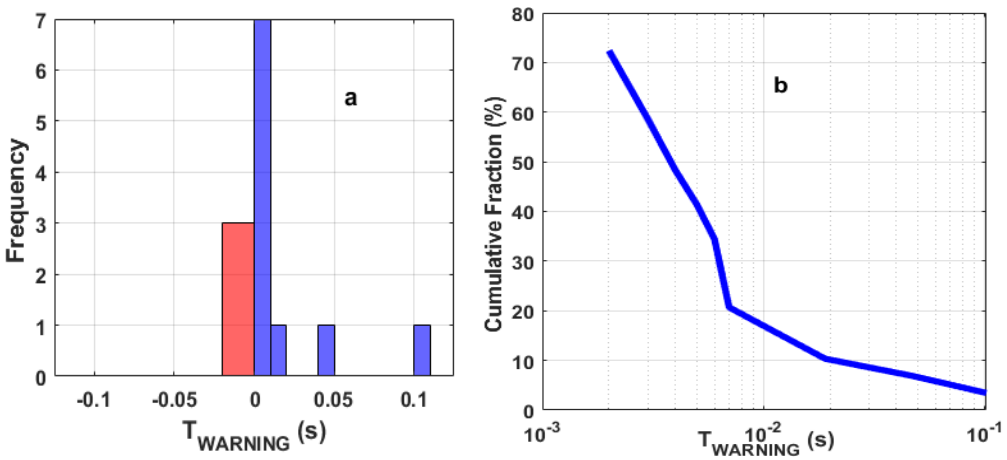

Figure 6.22: Warning times of the complete database of C39 for the LONGDIDT predictor.

6.3.5. Vessel Forces

Figure 6.23 and 6.24 present a comparison between the predicted vessel forces at the instances of occurrence of disruption and the time of detection between the CM predictor and the NRMLOCA predictor. Just like in the case of C38, the detections made by CM predictors are on higher average values of predicted vessel forces, making a case for early actions to cool down the plasma or to reduce the plasma current in order to reduce the impact of eventual

disruption on VV. It is worth noting that the difference between the mean values of the predicted vessel forces between $T_{disruption}$ and $T_{detection}$ is ~150 kN for CM predictor as compared to ~50 kN for NRMLOCA. The standard deviation values for the predicted forces are not too far off from one another for $T_{detection}$ and $T_{disruption}$ in case of both the CM and NRMLOCA predictors.

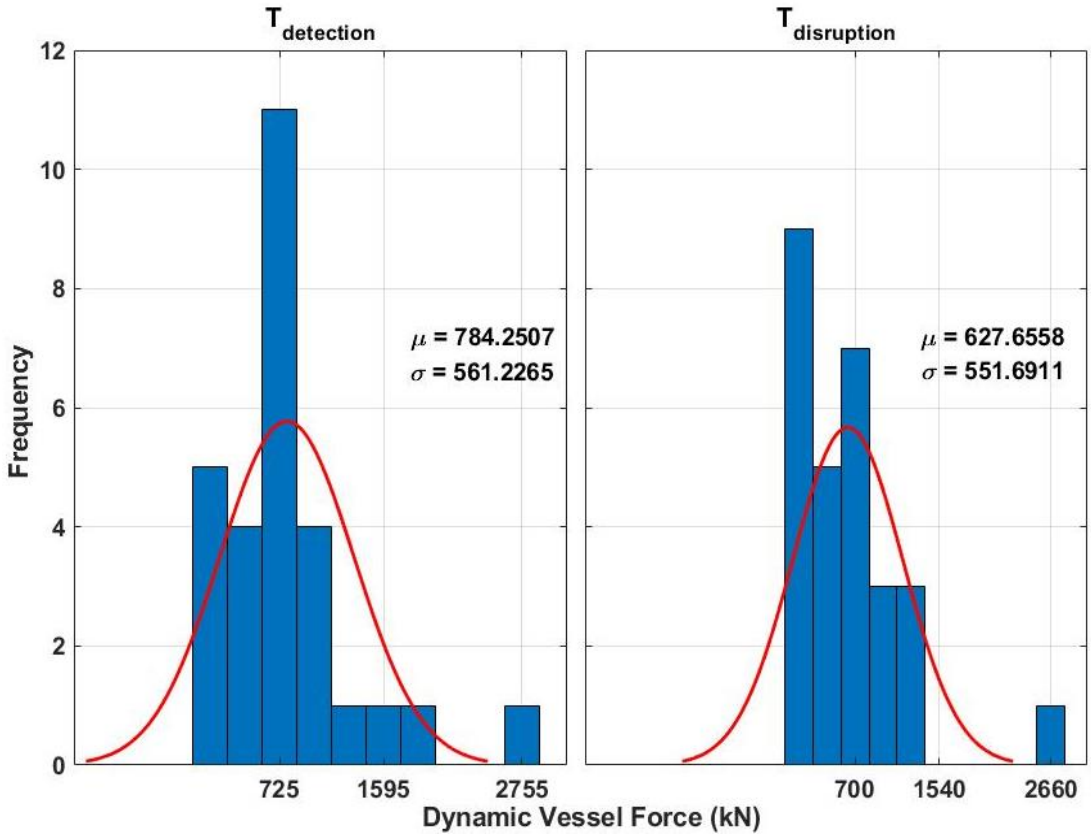

Figure 6.23: A direct comparison of values of F_P at $T_{detection}$ and $T_{disruption}$ for CM predictor.

Here in figure 6.25, a comparison is presented for the mean and standard deviation values of predicted vessel forces for all the detectors of PetraMit1 and CM predictor. Maintaining the consistency with C38, the CM predictor registered highest average values at $T_{detection}$ while not being far off from the standard deviation values.

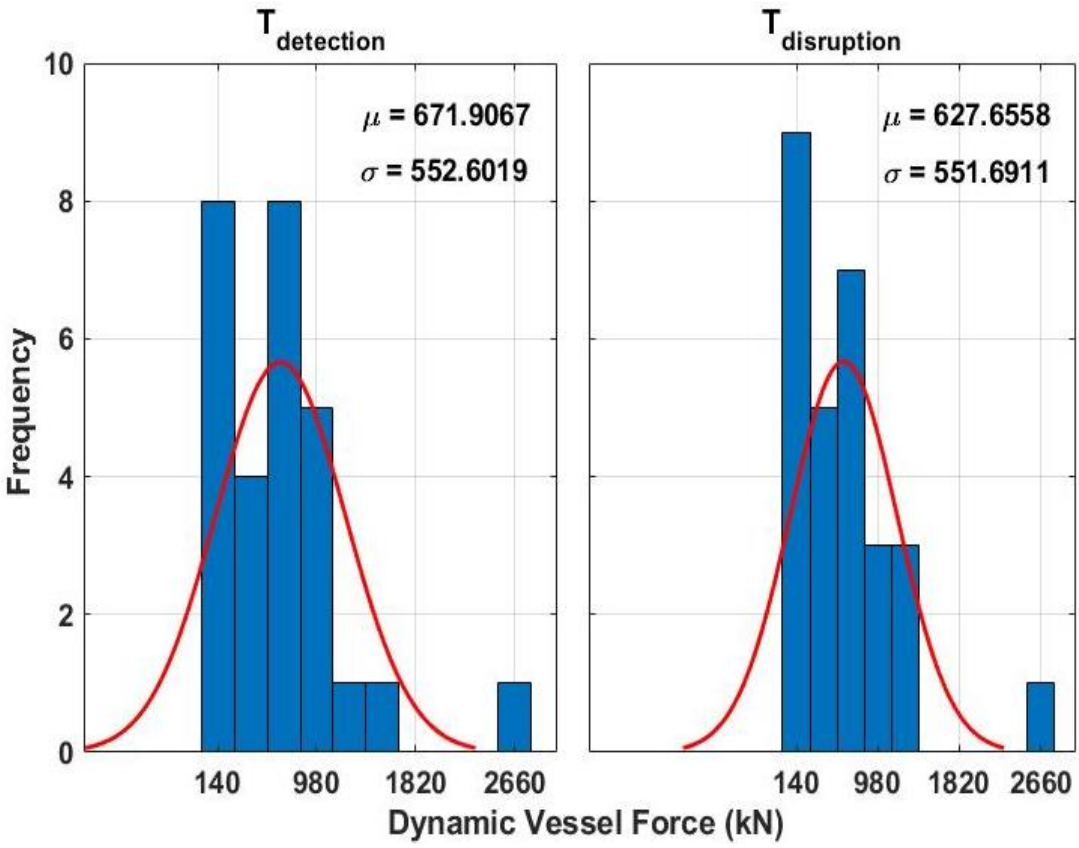

Figure 6.24: A direct comparison of values of F_P at $T_{detection}$ and $T_{disruption}$ for NRMLOCA predictor.

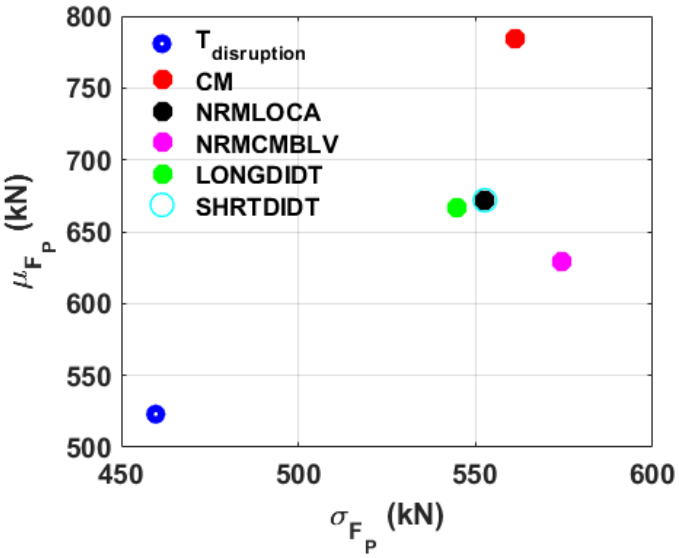

Figure 6.25. A comparison of mean and standard deviation values of F_P at $T_{detection}$ and $T_{disruption}$ between different predictors.

It is worth mentioning that unlike C38 and other future campaigns, the detailed scenario specific analysis was not possible owing to the fact that C39 has a rather smaller dataset in terms of disruptive discharges- which in a way is a positive sign so as to demonstrate that the operational boundaries are being pushed in a very careful manner to obtain maximum knowledge from an experiment and also prepare the device for an even more important experimental campaign. Still, with the analysis presented here, it is demonstrated once again that CM predictor is capable of outperforming the remaining PetraMit1 predictors even in case of a DT campaign- a detail very important as will be shown in the next sections and for the implementation of the CM predictor as a permanent member of device protection scenarios for future DT capable devices regardless of them being experimental or commercial fusion reactors.

6.4. JET C40A

C40A in JET was a short Tritium campaign carried out between January-July 2021 where different types of experiments were carried out to finalize the scientific goals for C41. However, due to a lot of starts and stops for commissioning of various essential systems during the campaign resulted in a small amount of experimental discharges- precisely 49 non-disruptive and 88 disruptive discharges. This means that even though a small scenario-wise analysis can be made, it can only be an indicative one rather than a benchmarking analysis and hence, will be skipped for C40A. Out of these 137 discharges, 15 discharges were made for **Baseline** scenario scientific goals, 20 discharges were made for **Hybrid** scenario scientific goals and the remaining 102 discharges were used for several different scientific goals including cleaning pulses to remove the impurities that might have gotten trapped in the VV due to a disruption. The campaign proved to be an excellent rehearsal for the highly anticipated C41- also known as DTE campaign, which is discussed in detail in section 6.5

6.4.1.CM predictor detection rates

Detection rates of the complete dataset are given in table 6.19. A very high success rate of the order of ~99% is achieved by the CM predictor out of which ~78.5% detections are made with warning times equal or higher than 10 ms- the criterion to define tardy detections. Remaining 20.5% of successful detections are tardy detections. Also, in this campaign, it was the first time that

a disruption was detected prematurely by the CM predictor with a $T_{warning}$ of 19 s, which influences highly the average warning time. Removal of the outlier with 19 s $T_{warning}$, we obtain an average of 145 ms of warning time, which is still a reasonably acceptable value. The CM predictor obtained an average value of -5 ms for the warning times for tardy detections, the detections made post disruptions are shown in red in figure 6.26.

Parameter	**Value**
Successful alarm rate	98.9 %
Missed alarm rate	1.1 %
False alarm rate	26.53 %
Average $T_{warning}$	363 ms

Table 6.19: CM predictor performance for the complete database of C40A

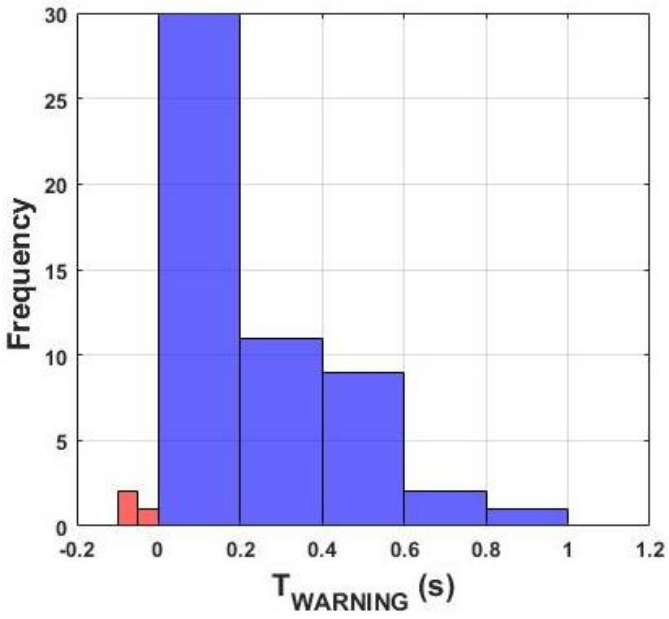

Figure 6.26: Warning times of the complete database of C40A for the CM predictor. The bars in red show detections post disruption.

As shown in figure 6.26, the majority of detections were made with a $T_{warning}$ between 0-0.6 s prior to the disruption- another demonstration of the capability of CM predictor to be used for mitigation purposes. A better insight on the overall trends of warning times can be had through figure 6.27, where the

cumulative fraction of successful detections is plotted as a function of $T_{warning}$. The semilog x-axis would suppress the contribution corresponding to $T_{warning} < 0$ s and hence, only the warning times > 10 ms are reflected in figure 6.27.

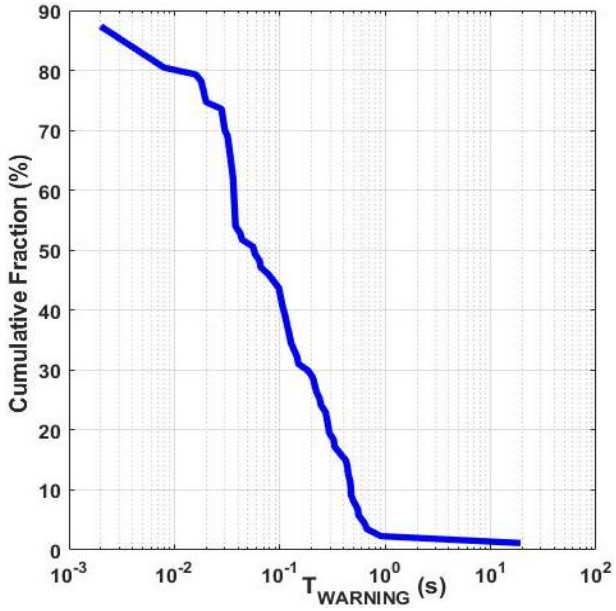

Figure 6.27: Cumulative frequency of detections as a function of $T_{warning}$ for all the detections made with at least 10 ms of reaction time.

6.4.2.NRMLOCA predictor detection rates

Detection rates and warning times for NRMLOCA are given in table 6.20. Consistent with the trends observed for C38 and C39, a 100% detection rate is accompanied by a 100% false alarm rate. Furthermore only ~55% of successful detections were made for $T_{warning}$ > 10 ms with the remaining ~45% detections being tardy detections. The average $T_{warning}$ value is -77 ms due to the presence of an outlier in both the premature detection (~19 s) and tardy detection side (- 28 s). Removal of those outliers, improves the average warning time to 23 ms, which is ~120 ms smaller compared to the CM predictor. The only improvement from CM predictor is that no alarms were missed but that loses significance due to the fact that the false alarm rate is 100%- meaning that every discharge, the NRMLOCA predictor raised an alarm. The average warning time for tardy detections -43 ms, much worse compared to the CM predictor. The warning times of the remaining alarms after removal of the two outliers are shown in figure 6.28. Compared to figure 6.26, the number of detections made post disruption is quite high for NRMLOCA than for CM predictor.

Parameter	Value
Successful alarm rate	100 %
Missed alarm rate	0 %
False alarm rate	100 %
Average $T_{warning}$	-77 ms

Table 6.20: NRMLOCA predictor performance for C40A

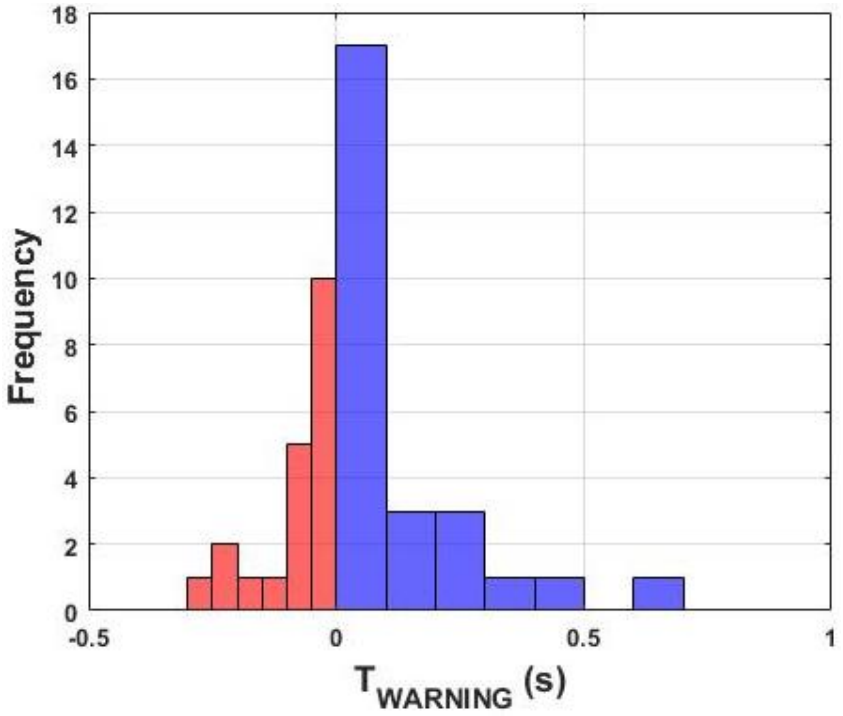

Figure 6.28: Warning times of the complete database of C40 for the NRMLOCA predictor. The bars in red show detections post disruption.

6.4.3.NRMCMBLV predictor detection rates

Table 6.21 demonstrates the detection rates for the complete restrained ring loop voltage predictor. No different to the previous campaigns discussed in this chapter, the predictor obtains a 100% successful detection rate but also, the false alarm rate is 100% and hence, either the alarms from this predictor are ignored or they produce hindrance in achieving scientific goals for a given experiment.

Parameter	Value
Successful alarm rate	100 %
Missed alarm rate	0 %
False alarm rate	100 %
Average $T_{warning}$	480 ms

Table 6.21: NRMCMBLV predictor performance for C40A

Worth highlighting is the fact that out of 100% successful detections, 86.4% are tardy detections. Also, the staggeringly high average $T_{warning}$ is caused by several premature detections as shown in figure 6.29 (a). As many as 4 detections were made with warning times greater than 6 s, out of which, 3 have warning times in excess of 10 s. There is also a tardy detection with warning time ~18 s, which is also a clear outlier. If all these 5 outliers are removed, the average warning time falls down to 48 ms, better than NRMCMBLV and ~100 ms lower than the average $T_{warning}$ for the CM predictor. Figure 6.29 (b) shows the distribution of $T_{warning}$ for all the discharges with positive warning times. As can be seen, a mere ~35% detections were made before the occurrence of a disruption, rest all were a posteriori detections.

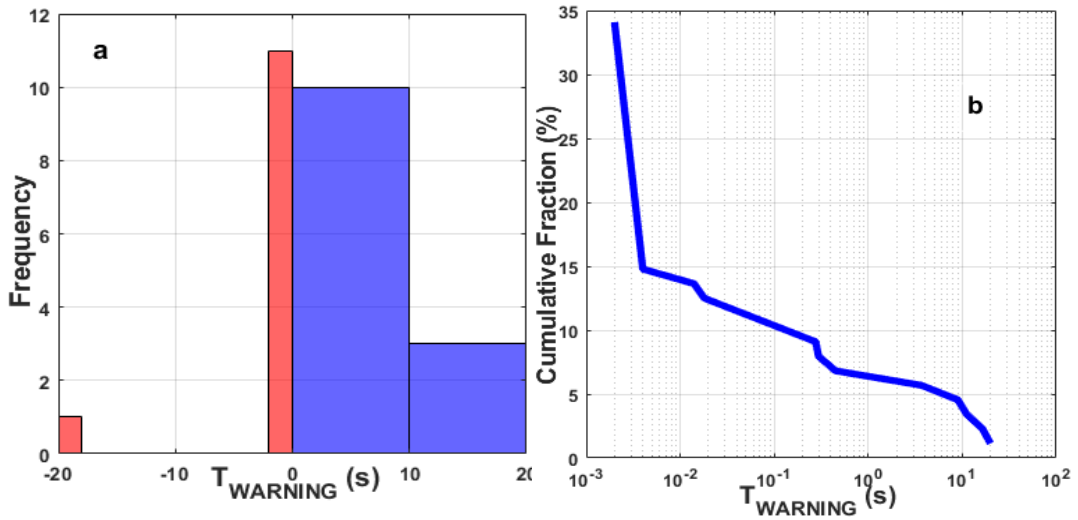

Figure 6.29: Warning times of the complete database of C40 for the NRMCMBLV predictor.

6.4.4. I_P time derivative (SHRTDIDT and LONGDIDT)

The performance evaluation parameters for SHRTDIDT and LONGDIDT are given in tables 6.22 and 6.23 respectively. For SHRTDIDT, the average warning time has a negative value, which means that majority of the disruptions were detected after they had already occurred because there are no outliers in terms of very high warning times be it positive or negative values.

Parameter	Value
Successful alarm rate	93.2 %
Missed alarm rate	6.8 %
False alarm rate	16.33%
Average $T_{warning}$	-18 ms

Table 6.22: SHRTDIDT predictor performance for C40A

Worth highlighting is the fact that no detections were made with sufficient $T_{warning}$ for mitigation action to be employed. In other words, all the successful detections for SHRTDIDT were tardy detections with an average positive warning time of the order of 1 ms. Histogram to illustrate the high number of tardy detections is shown in figure 6.30. There is no figure with cumulative fraction of successful detections for SHRTDIDT because a majority of detections are made with either negative or 0 warning times, which would not be plotted on a logarithmic x axis.

Parameter	Value
Successful alarm rate	98.9 %
Missed alarm rate	1.1 %
False alarm rate	51%
Average $T_{warning}$	-29 ms

Table 6.23: LONGDIDT predictor performance for C40A

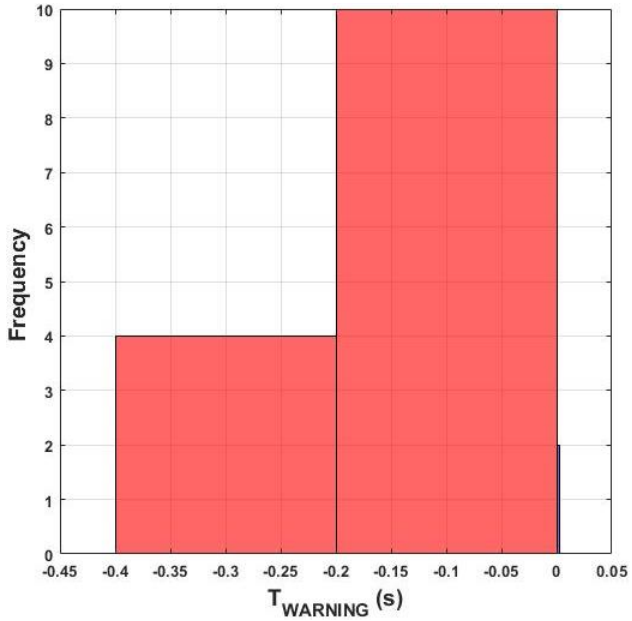

Figure 6.30: Warning times of C40A for the SHRTDIDT predictor.

LONGDIDT has a better performance comparing with SHRTDIDT in terms of successful alarm rate as well as missed alarms. 87.5% of the successful detections for LONGDIDT are in fact tardy detections but when compared to SHRTDIDT, LONGDIDT at least has 11.4% detections with warning times more than 10 ms. The average positive warning time is 30 ms and the average negative warning time is -68 ms. The histogram of detection count as a function of warning time is given in figure 6.31 (a). As opposite to SHRTDIDT, there are at least several detections with non-zero positive warning times and hence figure 6.31 (b) represents the overall distribution of positive warning times.

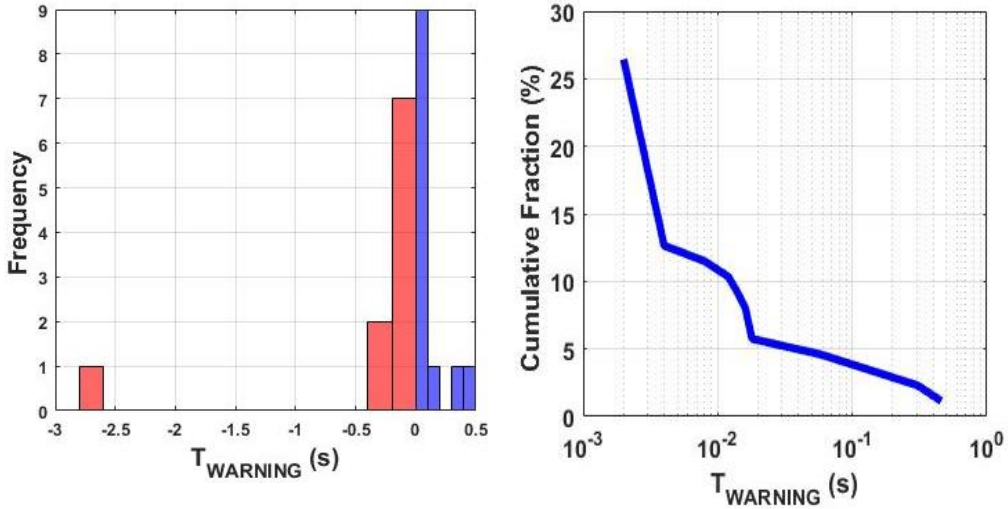

Figure 6.31: Warning times of the complete database of C40 for the LONGDIDT predictor.

6.4.5. Vessel Forces

In case of predicted vessel forces, the trend is followed just like in the case of C38 and C39, where the detections made by CM predictor are on higher average values of predicted vessel forces when compared to the values of predicted forces of disruption time. The mean value of the predicted vessel forces between $T_{disruption}$ and $T_{detection}$ is higher by ~80 kN for CM predictor whereas for NRMLOCA, value is lower by ~300 kN as shown in figure 6.32 and 6.33 respectively. Even though the peaks of the fitted distributions lie in the similar ranges of the value of F_P, CM predictor has more number of detections in the peak of distribution, meaning that a majority of detections were made while the predicted vessel force value was the highest among the distribution of values.

The case of NRMLOCA is a curious one because the average values of F_P at $T_{detection}$ are lower by ~300 kN compared to the mean value of F_P at $T_{disruption}$, this means that if one were to assign how perilous the disruption would be based on this value, they could end up severely underestimating the hazardous capacity of such a disruption. Also, the standard deviation of the F_P is different by ~120 kN, which means that there might be detections at even lower values of F_P.

The comparison between NRMLOCA, NRMCMBLV, SHRTDIDT and LONGDIDT as shown in figure 6.34 is also interesting in terms of the fact that all these predictors raise alarms at values of F_P in acceptable range of vicinity of the mean and standard deviation values of $T_{disruption}$. This however, is the only factor where the ring loop voltage and plasma current time derivative predictors perform better than NRMLOCA, in rest all the aspects, NRMLOCA is superior to them but the overall dominance of CM predictor is still maintained.

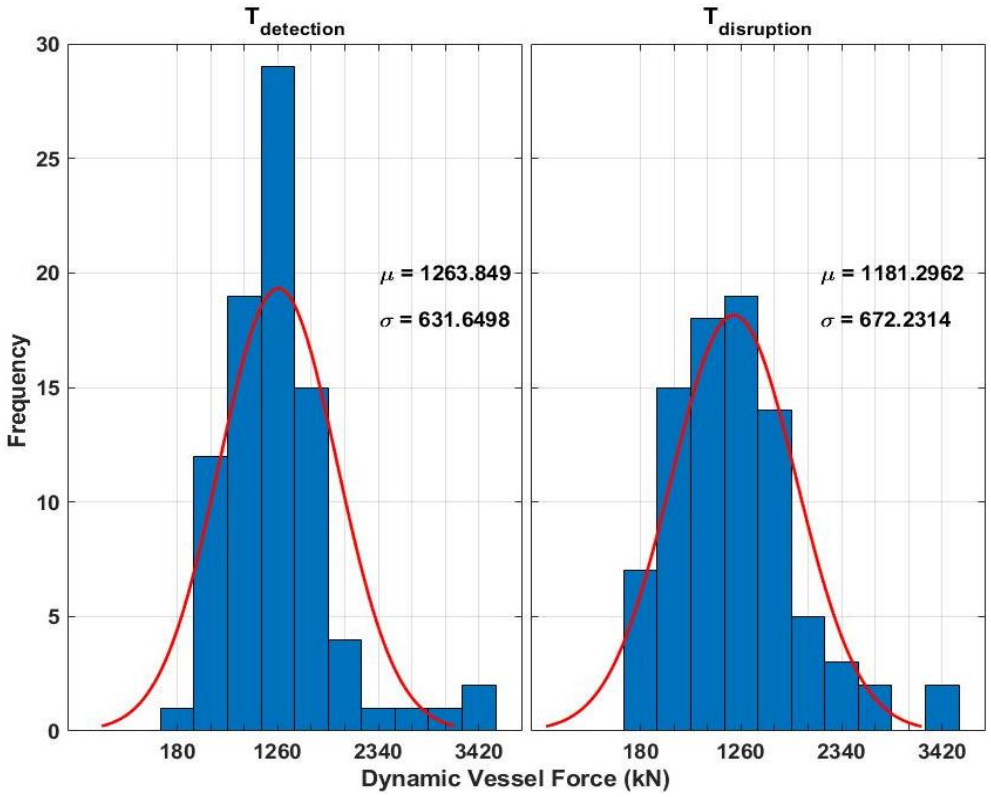

Figure 6.32: A direct comparison of values of F_P at $T_{detection}$ and $T_{disruption}$ for CM predictor.

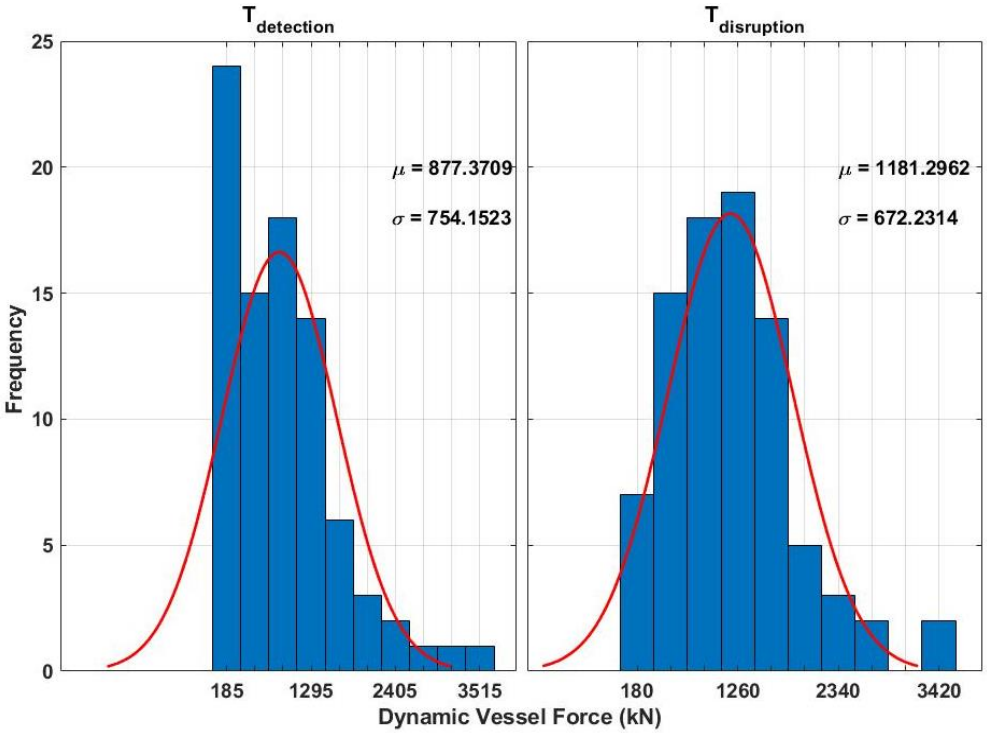

Figure 6.33: A direct comparison of values of F_P at $T_{detection}$ and $T_{disruption}$ for NRMLOCA

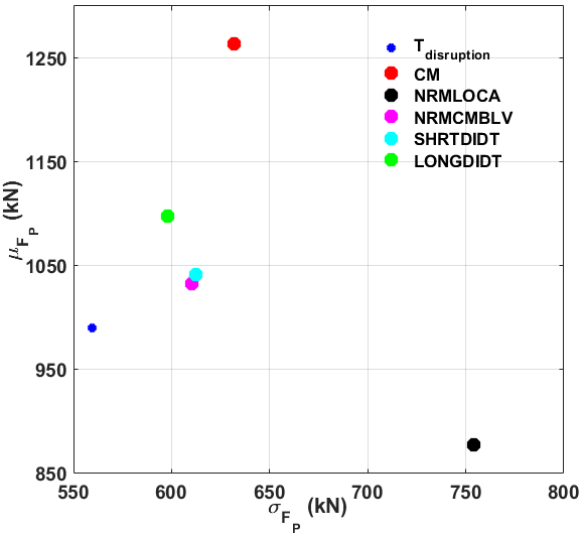

Figure 6.34. A comparison of mean and standard deviation values of F_P at $T_{detection}$ and $T_{disruption}$ between different predictors.

6.5. JET C41

After successful preparation with C38 and C39 as well a dress rehearsal in C40A, the much awaited deuterium-tritium experimental campaign 2 (also known as DTE2) was carried out in the latter half of 2021 during the months of August-December. A total of 653 discharges were produced, including dry runs as well as cleaning discharges and also, several hundreds of vessel conditioning shots. The principal objective of C41 was to demonstrate that DT experiments can be done in metallic walls of JET and compare the highest net fusion energy output to the one obtained during DTE1 (in 1990s). C41 is seen as a culmination of ITER related preparations in JET with demonstration of working principles. The C41 had experimental discharges programmed for 18 different types of experiments. Some of the more important scenarios are listed in table 6.24.

Code	Experiment description
M21-01	*Hybrid scenario for high fusion performance in DT*
M21-02	DT scenario with optimized non-thermal fusion
M21-03	*Baseline scenario for high fusion performance in DT*
M21-06	Integrated high performance seeded scenario
M21-12	Confinement and transport in mixed DT plasmas
M21-17	2^{nd} harmonic heating of T in DT plasmas for ITER
M21-27	Fuel retention and long term outgassing

Table 6.24: Some important experimental scenarios in C41

Upon concerted efforts, we realized that the number of useful discharges for the analysis of CM predictor performance is underwhelming for such an important campaign. A total of 95 disruptive and 161 non-disruptive discharges were considered for the analysis presented in this section. Such low number of useful discharges is explained by the need of meticulous preparation required to guarantee maximum efficiency of the tritium used for particular scenario experiments and quality data production. Several experiments require very clean machine environment, which implies a high number of cleaning/machine conditioning discharges during the preparatory phase. Out of 256 available discharges, 39 discharges belong to the **hybrid** scenario whereas 25 discharges belong to the **baseline** scenario experiments. Furthermore, out of 39, 25 discharges are non-disruptive and 14 disruptive from hybrid scenario compared to 13 non-disruptive and 12 disruptive discharges from baseline scenario.

6.5.1.CM predictor detection rates

CM predictor continued obtaining favorable detection rates throughout the course of C41. A very high detection rate of ~99% successful detection was achieved while maintaining the false alarm rate below 25%. A more than acceptable average warning time of 160 ms is obtained as well. Only a solitary alarm was missed as shown in table 6.25.

Parameter	**Value**
Successful alarm rate	98.9 %
Missed alarm rate	1.1 %
False alarm rate	24.22 %
Average $T_{warning}$	160 ms

Table 6.25: CM predictor performance for the complete database of C41

Just like all previous campaigns, the successful alarm rate in table 6.25 has contributions from detections with warning times ≥ 10 ms as well as tardy alarms. The successful alarm rate with warning time greater than 10 ms is 78.9% and the successful alarm rate with warning time less than 10 ms is 20%. The average positive $T_{warning}$ is 177 ms whereas the average negative $T_{warning}$ is -1 ms. As shown in figure 6.35, the number of detections with $T_{warning} > 1$ s is very low

and hence, the CM predictor emphasizes the potential usability as a mitigation predictor.

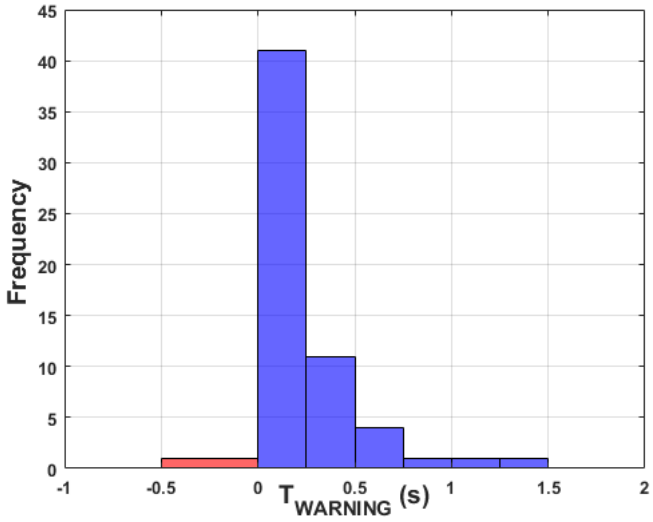

Figure 6.35: Warning times of the CM predictor for C41. The bars in red show detections post disruption.

As we have done in previous sections, here we present a different perspective on the warning times by means of figure 6.36, where the cumulative fraction of successful detections is plotted as a function of $T_{warning}$. Warning times corresponding to 0 and negative values are suppressed on the semi logarithmic x-axis. It is still worth mentioning that ~87% of the detections were made prior to the occurrence of a disruption.

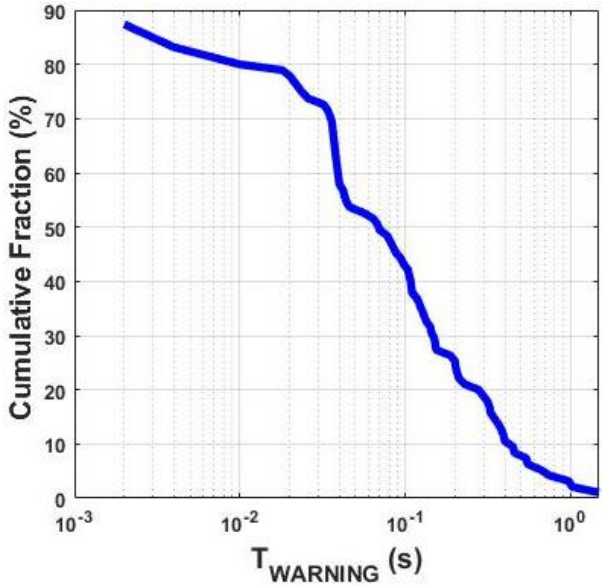

Figure 6.36: Cumulative frequency of detections as a function of $T_{warning}$

6.5.2.NRMLOCA predictor detection rates

The NRMLOCA predictor demonstrated no difference in the performance compared to the previous campaigns. A 100% successful detection rate accompanied by a 100% false alarm rate does not help in making a case for NRMLOCA for ITER operations as shown in table 6.26.

Parameter	Value
Successful alarm rate	100 %
Missed alarm rate	0 %
False alarm rate	100 %
Average $T_{warning}$	-353 ms

Table 6.26: NRMLOCA predictor performance for C41

The average warning time in table 6.26 is skewed due to the presence of a tardy detection with warning time of -35 s. Removal of the outlier improves the average $T_{warning}$ to 16 ms, which would still be ~145 ms smaller compared to the CM predictor. Moreover, the average positive $T_{warning}$ is ~57 ms, being 120 ms smaller to the one of CM predictor. The average negative $T_{warning}$ is -9 ms, approaching an order of magnitude worse compared to the CM predictor.

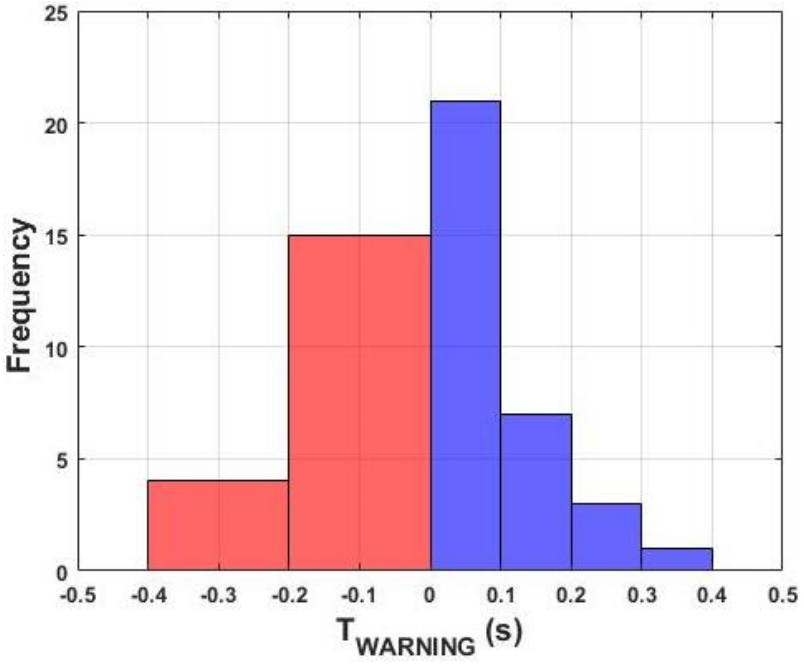

Figure 6.37: Warning times of the complete database of C41 for the NRMLOCA predictor. The bars in red show detections post disruption.

A direct comparison between figures 6.35 and 6.37 shows a worse performance of NRMLOCA in terms of number of detections a posteriori. Using the same diagnostic signal for prediction and yet, such vast difference in the performance is yet another proof of disadvantage of using a simple threshold value- a point raised in section 6.2.2. The tendency has been demonstrated time and again throughout the analysis of C38, C39, C40A- improvement in detection time is a feature of CM predictor, obtained using a two dimensional SVM like framework where decision boundary is expressed by a linear equation but is not a simple threshold.

6.5.3. NRMCMBLV predictor detection rates

The detection rates of NRMCMBLV predictor are also consistent with the trends observed for C38, C39 and C40A. No alarms are missed but alarms were raised for every single discharge of the database- losing meaning of the prediction qualification. A high average warning time as reflected in table 6.27 is a consequence of seven premature detections with warning times above 2 s, with the highest being ~ 16 s. Removal of all the seven outliers brings the average $T_{warning}$ down to -8 ms- in other words, except for the premature predictions, all other predictions on average were a posteriori predictions.

Parameter	Value
Successful alarm rate	100 %
Missed alarm rate	0 %
False alarm rate	100 %
Average $T_{warning}$	660 ms

Table 6.27: NRMCMBLV predictor performance for C41

The 100% successful detection rate in table 6.27 comprises of a staggering 88.4% tardy detections and mere 11.6% detections with $T_{warning}$ above 10 ms. Here it is worth remembering that out of those 11.6%, 7 are premature detections, which we have deemed as outliers. So, in terms of actual detections with $T_{warning} > 10$ ms, there are only four discharges. Figure 6.38 (a) shows the distribution of outliers according to their warning times. Frequency value corresponding to the first bin with positive warning times also includes several detections with $T_{warning}$ being 0 s. Figure 6.38 (b) shows the distribution of $T_{warning}$ for all the detections with positive warning times.

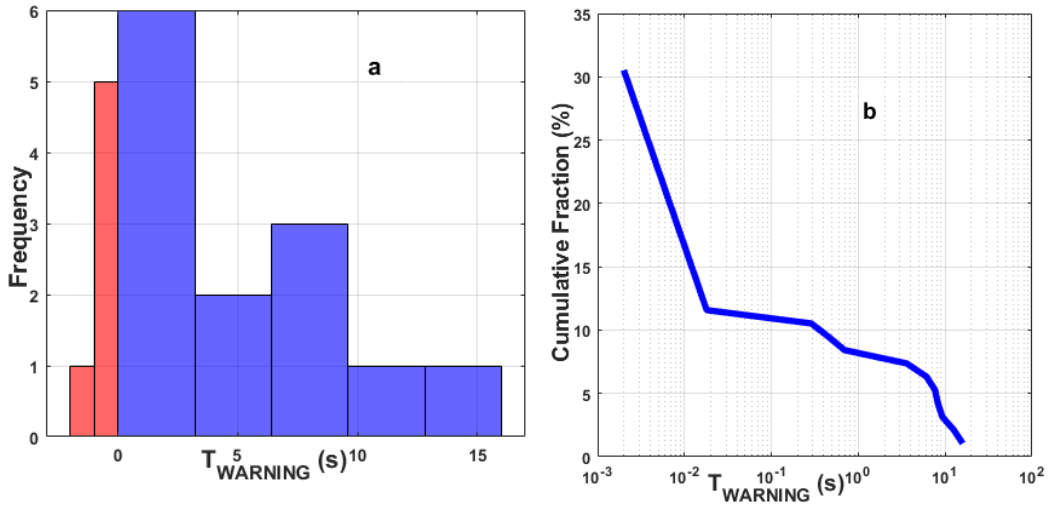

Figure 6.38: Warning times for C41 for the NRMCMBLV predictor.

6.5.4. I_P time derivative (SHRTDIDT and LONGDIDT)

SHRTDIDT and LONGDIDT are two predictors designed to detect a sudden current quench, which could sometimes be a precursor to an impending disruption. As seen for the previous campaigns, the performance of either of SHRTDIDT or LONGDIDT is nowhere close the one of CM predictor. Even for C41, SHRTDIDT obtained a negative average warning time as shown in table 6.28. All the successful detections were tardy detections with most detections producing negative warning times, again, correctly reflected in table 6.29.

Parameter	Value
Successful alarm rate	98.9%
Missed alarm rate	1.1 %
False alarm rate	8.7%
Average $T_{warning}$	-12 ms

Table 6.28: SHRTDIDT predictor performance for C41

The average values of negative warning time is ~ 19 ms whereas average positive warning time is 1 ms for SHRTDIDT. Only 33% of successful detections obtain positive warning times, rest 67% showed negative warning times. The comparison of warning times is given in figure 6.39. 50% of the positive warning time detections had a warning time less than 1 ms and the remaining 50% showed

a warning time of 2 ms. Due to this, there only a histogram showing warning time distribution for SHRTDIDT and not a cumulative frequency distribution curve.

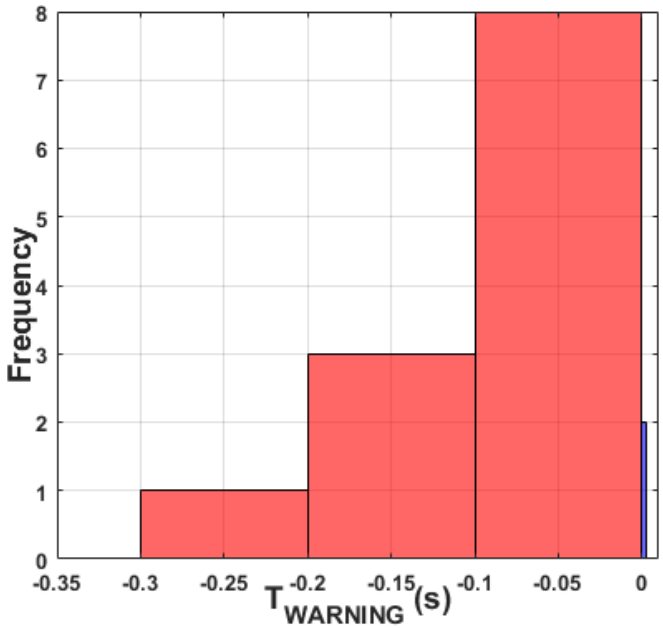

Figure 6.39: Warning times of C41 for the SHRTDIDT predictor.

In comparison to SHRTDIDT, the LONGDIDT showed some improvement in average warning time but the higher rate of false alarms was also observed. The 98.9% successful detection rate shown in table 6.29 is a combination of 83.1% tardy detections and only a 15.8% detection with warning times superior to 10 ms.

Parameter	Value
Successful alarm rate	98.9 %
Missed alarm rate	1.1 %
False alarm rate	29.2%
Average $T_{warning}$	-8 ms

Table 6.29: LONGDIDT predictor performance for C41

Being based on a similar working principle as SHRTDIDT, LONGDIDT had similarities in tendencies in the performance. Identical to SHRTDIDT,

LONGDIDT had only 33% of successful detections with a positive warning time with mean value of 1.5 ms. Remaining 67% of successful predictions returned an average warning time of -12 ms. Furthermore, another striking similarity was observed in terms of 50% of the positive warning time detections being less than 1 ms and the remaining 50% having a warning time of 2 ms. This explains why there is only a histogram in figure 6.40 as opposed to sections 6.3.4 and 6.4.4.

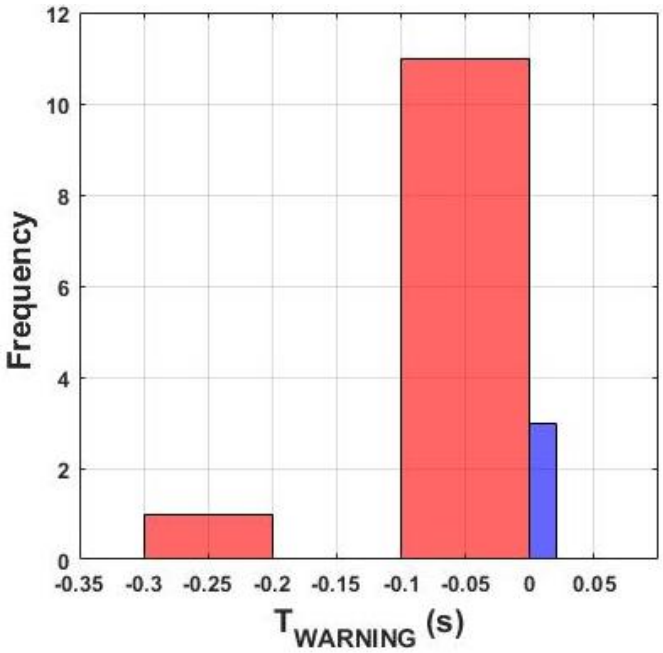

Figure 6.40: Warning times of the complete database of C41 for the LONGDIDT predictor.

6.5.5. Vessel Forces

Last but not the least, the comparison of predicted vessel forces is also carried out for C41 database. The CM predictor once again did the excellent job by predicting the disruptions at higher mean values of F_P compared to NRMLOCA and all the other PetraMit1 predictors. The CM predictor detected upcoming disruptions with an average of ~100 kN higher value of F_P as shown in figure 6.41. The standard deviation value is lower to that of disruption time, which is a positive because this means that even if the disruption is detected at a slightly lower value of F_P, it will not be too small to be ignored.

Predictions made by NRMLOCA were as usually, at lower values of F_P compared to the values for disruption time. The difference being ~200 kN, which is a significant difference, especially when it is lower. Also, as shown in figure

6.42, the majority of predictions made by NRMLOCA were at very low values of F_P, lower than 500 kN. This could create a severe underestimation of danger of an upcoming disruption and result in catastrophic consequences.

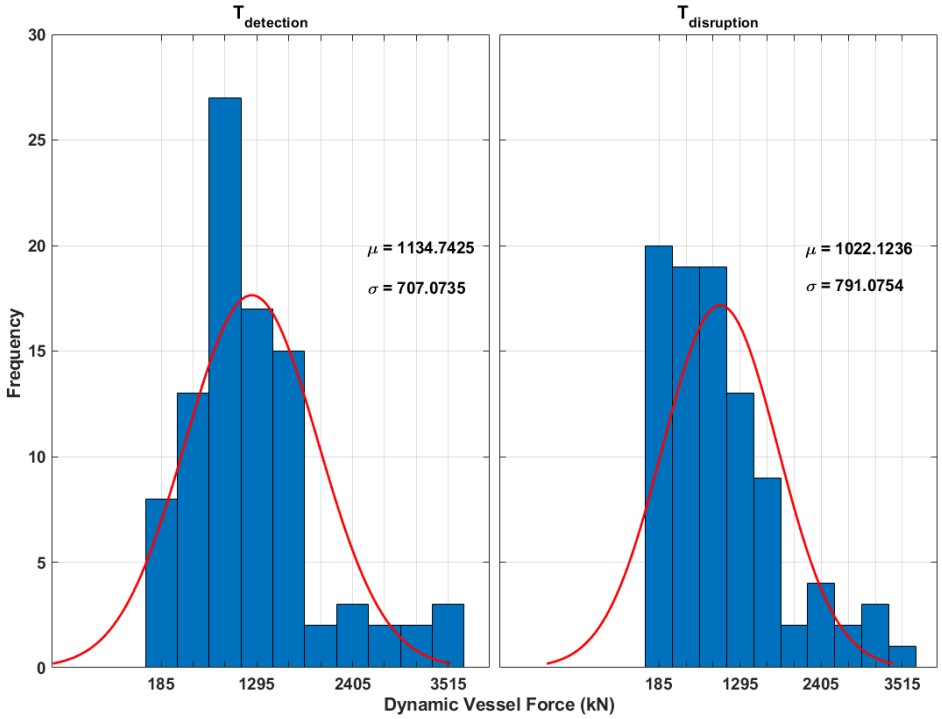

Figure 6.41: A direct comparison of values of F_P at $T_{detection}$ and $T_{disruption}$ for CM predictor.

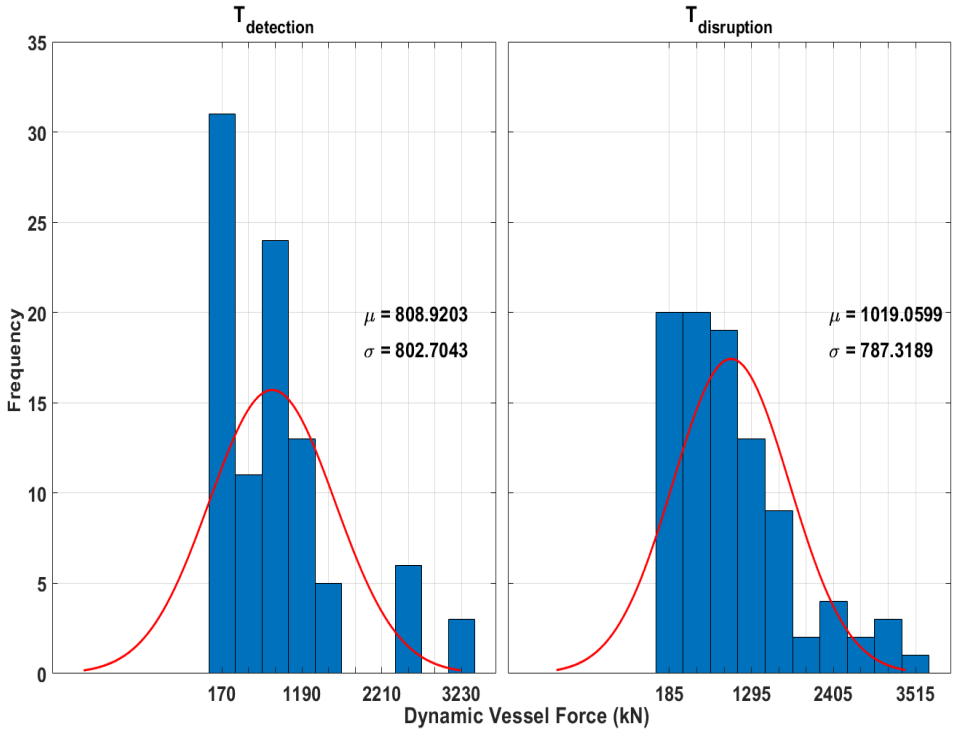

Figure 6.42: A direct comparison of values of F_P at $T_{detection}$ and $T_{disruption}$ for NRMLOCA

Remaining predictors comprising PetraMit1 were also looked at in terms of F_P value comparison. Figure 6.43 shows a comparison of mean and standard deviation values for $T_{detection}$ and $T_{disruption}$. SHRTDIDT and LONGDIDT are quite similar with NRMCMBLV also demonstrating likewise trends. Both CM and NRMLOCA predictors are equidistant to the point of F_P closer to the average values at $T_{disruption}$ but CM predictor is on higher values of mean F_P, making it crucial for disruption handling action.

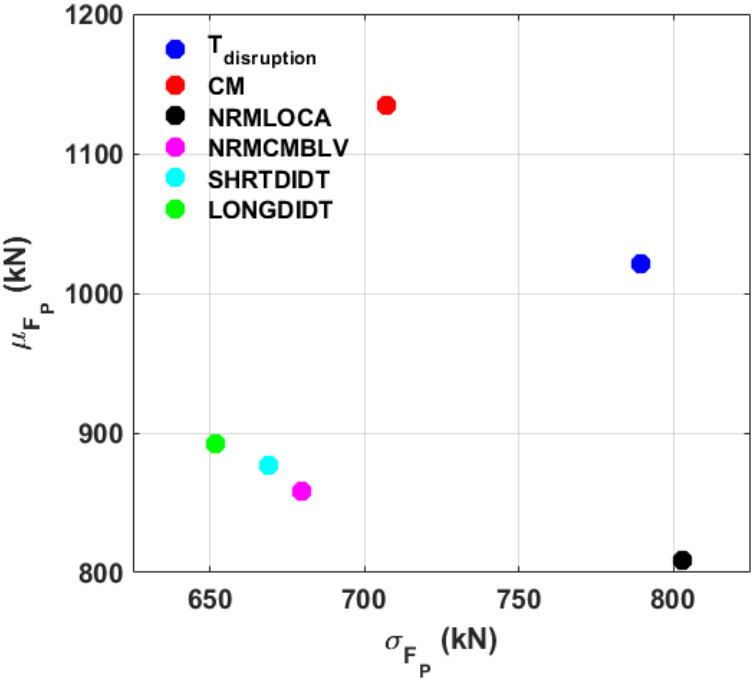

Figure 6.43. A comparison of mean and standard deviation values of F_P at $T_{detection}$ and $T_{disruption}$ between different predictors.

Chapter 7 – Discussion and Future work

In this chapter, a review of the results discussed in chapter 6 is made. Mainly the effectiveness of the CM predictor over PetraMit1 systems. Also, a brief discussion about how the CM predictor could be exploited better for JET, ITER and other similar devices' real time protection system is presented.

7.1. Feasibility of CM predictor

The CM predictor, originating from the need and idea of a simple, easily scalable and implementable, cross device disruption predictor for mitigation purposes, shows excellent results in the very first experimental campaign after the real time implementation in JET. With a very straightforward implementation and rather basic working principle where in the real time system, after acquiring the signals for ML and I_P, the only mathematical operation needed to check if the plasma is in disruptive state or not is a simple division, the CM predictor should attract a lot of interest for ITER, DEMO and other ITER class tokamaks.

The first and most important task was the preparation of a reliable database of the JET experimental campaigns C38-C41, where intentional disruptions and discharges where Error Field Correction Coils (EFCC) were used, had to be ignored to truly evaluate the performance of CM predictor. The reason for excluding the EFCC related experiments is the existence of cross-talk between EFCC and magnetic diagnostics, causing ML amplitude signal to saturate and thus, rendering it unusable for the CM predictor. An exhaustive database was prepared which was useful not only for this thesis work but also for the other activities of the disruption prediction group of CIEMAT.

Useful tools and repositories were created during the course of this work. As a result, the analysis of the CM predictor for future real time implementations will be a seamless task with minimum effort on the part of the scientist. The only important factor being the reliability of the disruption database and availability of the signals. Reliability of the database is qualified in terms of determination of instances of disruptions with utmost precision since the computation of warning times is directly dependent on the disruption time. Similarly, the signals to be used for CM predictor need to be independent of any type of random offset,

and guarantee the fulfillment of IID hypothesis to avoid any artifact caused by possible existence of bias.

Scenario wise analysis of the CM predictor also provides insight on the possible use of the predictor for disruption type classification- a task which could be extremely useful for future operational conditions in order to be able to not only detect an incoming disruption but also, know the type and choose a mitigation method accordingly instead of causing the plasma to cool down using MGI or killer pellets and try to have a soft landing of the discharge. Disruption type classification could also help in finding the physics relation with the precursor used- the Mode Locking phenomenon.

7.2. Future Work

The most exciting aspect for the future work related to the CM predictor is its potential use at ITER and DEMO and before that, at JET and JT60- SA to demonstrate the robustness and reliability for machine safety. Lack of a concrete and closed model of origin and evolution of disruptive behavior in plasma leave much to be desired from data driven methods. A possible line of continuation of this work could be in the direction of extension of the model to include disruption type classification, where not only the disruptions are to be detected in advance, in addition, the identification of the type of impending disruption could also be attempted to improve the corresponding course of action in the lines of maintaining the discharge running and hence, improving the overall efficiency of the reactor.

Apart from type classification, another line of research could be opened by combining such simple models with more complex methods like anomaly detection or genetic algorithms. Using a sure precursor like mode locking for machine safety application while incorporating an anomaly detection algorithm using Martingales for example, could lead to interesting results.

Independence of the model on historical data by means of possible from scratch implementation also revolutionizes the data load handling necessities for a data driven method like the CM predictor. Instead of having to go through terabytes of data, using a set of select signals, a similar predictor could be obtained. For that, a different precursor could be chosen, tried and tested for development of a linear predictor based on the general equation mentioned in chapter 4.

Using all the knowledge about disruption prediction that is being created across the globe, models based on transfer learning could also be developed. This type of models can further advance our capacity to predict disruptions using the information garnered across various tokamaks using different methods for disruption prediction. Such a predictor could prove to be the ultimate predictor with a wide range of versatility and applicability.

Bibliography

1. IAEA world energy outlook
   https://www.iea.org/reports/world-energy-outlook-2020
2. Clean Energy Wire
   https://www.cleanenergywire.org/factsheets/history-behind-germanys-nuclear-phase-out
3. Stanford News
   https://news.stanford.edu/2022/05/30/small-modular-reactors-produce-high-levels-nuclear-waste/
4. NASA Solar Physics Marshall Space Flight Center
   https://solarscience.msfc.nasa.gov/interior.shtml
5. Nuclear fusion cross sections and reactivities
   https://scipython.com/blog/nuclear-fusion-cross-sections
6. ITER NEWSLINE: Searching for the perfect shape
   https://www.iter.org/newsline/-/3037
7. Max-Planck Institut für Plasmaphysik
   https://commons.wikimedia.org/w/index.php?curid=24388371
8. Blum J et al, 2016, "Control Methods for the Optimization of Plasma Scenarios in a Tokamak", System Modeling and Optimization. CSMO 2015. IFIP Advances in Information and Communication Technology, vol 494. Springer, Cham.
9. J D Lawson, 1957, "Some Criteria for a Power Producing Thermonuclear Reactor", Proc. Phys. Soc. B 70 6
10. A J Webster, 2003, "Fusion: Power for the future", Phys. Educ. 38 135
11. EUROFUSION media library
    https://www.euro-fusion.org/media-library/fusion-experiments/

12. A Murari et al, 2005, “Burning Plasma diagnostics for the physics of JET and ITER”, Plasma Phys. Control. Fusion 47 B249
13. J Figueiredo et al, 2016, “JET diagnostic enhancements in preparation for DT operations”, Rev. Sci. Instrum. 87 11D443
14. J Figueiredo et al, 2018, “JET diagnostic enhancements testing and commissioning in preparation for DT scientific campaigns”, Rev. Sci. Instrum. 89 10K119
15. Creative Commons License https://creativecommons.org/licenses/by-nc-nd/4.0/
16. P H Rebut et al, 1985, “The Joint European Torus: Installation, first results and prospects”, Nucl. Fusion 25 1011
17. C I Stuart et al, 2021, “PETRA: A generalised real-time event detection platform at JET for disruption prediction, avoidance and mitigation”, Fusion Engineering and Design 168 112412
18. INTOR: The international fusion reactor that never was https://www.iter.org/newsline/62/146
19. F Wagner et al, 1982, “Regime of Improved Confinement and High Beta in Neutral-Beam-Heated Divertor Discharges of the ASDEX Tokamak”, Phys. Rev. Lett. 49 1408
20. K Steinmetz et al, 1987, “Observation of a high-confinement regime in a tokamak plasma with ion cyclotron resonance heating”, Phys. Rev. Lett. 58 124
21. Kaye S M et al, 1984, “Attainment of high confinement in neutral beam heated divertor discharges in the PDX tokamak”, J. Nucl. Mater. 121 115
22. Burrell K H et al, 1987, “Observation of an improved energy-confinement regime in neutral-beam–heated divertor discharges in the DIII-D tokamak”, Phys. Rev. Lett. 59 1432

23. Tanga A et al, 1987, “Magnetic separatrix experiments in JET”, Nucl. Fusion 27 1877
24. Keilhacker M et al, 1999, “High fusion performance from deuterium-tritium plasmas in JET”, Nucl. Fusion 39 209
25. M Shimada et al, 2007, “Progress in the ITER Physics Bases, Chapter 1: Overview and summary”, Nucl. Fusion 47 S1
26. Martin Greenwald, 2002, “Density limits in toroidal plasmas”, Plasma Phys. Control. Fusion 44 R27
27. F C Schuller, 1995, “Disruptions in tokamaks”, Plasma Phys. Control. Fusion 37 A135
28. T C Hender, 2014, “Active Control of Magneto-hydrodynamic Instabilities in Hot Plasmas, Chapter 7:Disruptions”, Springerlink, ISBN 9783662442227
29. T C Hender et al, 2007, “Chapter 3: MHD stability, operational limits and disruptions”, Nucl. Fusion 47 S128
30. V Riccardo et al, 2010, “JET disruption studies in support of ITER”, Plasma Phys. Control. Fusion 52 124018
31. P C de Vries et al, 2012, “The impact of the ITER-like wall at JET on disruptions”, Plasma Phys. Control. Fusion 54 124032
32. H Dreicer, 1959, “Electron and Ion Runaway in a Fully Ionized Gas. I”, Phys. Rev. 115, 238
33. H Dreicer, 1960, “Electron and Ion Runaway in a Fully Ionized Gas. II”, Phys. Rev. 117 329
34. Sokolov Yu A, 1979, “Multiplication of accelerated electrons in a tokamak”, JETP Lett. 29 218
35. P C de Vries et al, 2009, “Statistical analysis of disruptions in JET”, Nucl. Fusion 49 055011

36. H P Furth et al, 1963, “Finite-Resistivity Instabilities of a Sheet Pinch”, Phys. Fluids 6 459
37. A H Reiman, 1991, “Tokamak magnetic islands in the presence of nonaxisymmetric perturbations”, Phys. Fluids B 3 2617
38. Peter Montag, 2018, “Modeling the Formation of Current Sheets in Symmetric and Asymmetric Reconnection”, PhD Thesis
39. M F F Nave et al, 1990, “Mode locking in tokamaks”, Nucl. Fusion 30 2575
40. R J La Haye, 2006, “Neoclassical tearing modes and their control”, Phys. Plasmas 13 055501
41. R J La Haye, 2002, “Control of neoclassical tearing modes in DIII–D”, Phys. Plasmas 9 2051
42. G Pautasso et al, 2003, “Chapter 12: Study of Disruptions in ASDEX Upgrade”, Fusion Science and Technology 44 716
43. A Isayama et al, 2005, “Steady-state sustainment of high-β plasmas through stability control in Japan Atomic Energy Research Institute Tokamak-60 Upgrade”, Phys. Plasmas 12 056117
44. G Sias et al, 2019, “A locked mode indicator for disruption prediction on JET and ASDEX upgrade”, Fusion Engineering and Design 138 254
45. D R Ferreira et al, 2022, “Explainable deep learning for the analysis of MHD spectrograms in nuclear fusion”, Mach. Learn.: Sci. Technol. 3 015015
46. B Cannas et al, 2004, “Disruption forecasting at JET using neural networks”, Nucl. Fusion 44 68
47. B Cannas et al, 2004, “Neural approaches to disruption prediction at JET”, 31st EPS Conference on Plasma Physics
48. B Cannas et al, 2007, “A prediction tool for real-time application in the disruption protection system at JET”, Nucl. Fusion 47 1559

49. B Cannas et al, 2013, “Automatic disruption classification based on manifold learning for real-time applications on JET”, Nucl. Fusion 53 093023
50. G Pautasso et al, 2001, “Prediction and mitigation of disruptions in ASDEX Upgrade”, Journal of Nucl. Materials 290 1045
51. F C Morabito et al, 2001, “Fuzzy-neural approaches to the prediction of disruptions in ASDEX Upgrade”, Nucl. Fusion 41 1715
52. G Pautasso et al, 2002, “On-line prediction and mitigation of disruptions in ASDEX Upgrade”, Nucl. Fusion 42 100
53. B Cannas et al, 2010, “An adaptive real-time disruption predictor for ASDEX Upgrade”, Nucl. Fusion 50 075004
54. D Wroblewski et al, 1997, “Tokamak disruption alarm based on a neural network model of the high- beta limit”, Nucl. Fusion 37 725
55. R Yoshino et al, 2003, “Neural-net disruption predictor in JT-60U”, Nucl. Fusion 43 1771
56. R Yoshino et al, 2005, “Neural-net predictor for beta limit disruptions in JT-60U”, Nucl. Fusion 45 1232
57. C Windsor et al, 2005, “A cross-tokamak neural network disruption predictor for the JET and ASDEX Upgrade tokamaks”, Nucl. Fusion 45 337
58. C Rea et al, 2018, “Disruption prediction investigations using Machine Learning tools on DIII-D and Alcator C-Mod”, Plasma Phys. Controlled Fusion 60 084004
59. C Rea et al, 2019, “A real-time machine learning-based disruption predictor in DIII-D”, Nucl. Fusion 59 096016
60. A Murari et al, 2008, “Prototype of an adaptive disruption predictor for JET based on fuzzy logic and regression trees”, Nucl. Fusion 48 035010

61. D Silver et al, 2016, “Mastering the game of Go with deep neural networks and tree search”, Nature 529 484
62. J Kates-Harbeck et al, 2019, “Predicting disruptive instabilities in controlled fusion plasmas through deep learning”, Nature 568 526
63. J X Zhu et al, 2021, “Hybrid deep-learning architecture for general disruption prediction across multiple tokamaks”, Nucl. Fusion 61 026007
64. J Vega et al, 2008, “Data mining technique for fast retrieval of similar waveforms in Fusion massive databases”, Fusion Engineering and Design 83 132
65. J Vega et al, 2009, “New developments at JET in diagnostics, real-time control, data acquisition and information retrieval with potential application to ITER”, Fusion Engineering and Design 84 1916
66. J Vega et al, 2009, “Automated estimation of L/H transition times at JET by combining Bayesian statistics and support vector machines”, Nucl. Fusion 49 085023
67. J Vega et al, 2010, “A universal support vector machines based method for automatic event location in waveforms and video-movies: Applications to massive nuclear fusion databases”, Rev. Sci. Instrum. 81 023505
68. J Vega et al, 2010, “Accurate and reliable image classification by using conformal predictors in the TJ-II Thomson scattering”, Rev. Sci. Instrum. 81 10E118
69. J Vega et al, 2013, “Spatial location of local perturbations in plasma emissivity derived from projections using conformal predictors”, Nuclear Instrum and Methods in Physics Research A 720 14
70. J Vega et al, 2013, “Results of the JET real-time disruption predictor in the ITER-like wall campaigns”, Fusion Engineering and Design 88 1228
71. J Vega et al, 2014, “Real-time change detection in data streams with FPGAs”, Fusion Engineering and Design 89 644

72. J Vega et al, 2014, “Adaptive high learning rate probabilistic disruption predictors from scratch for the next generation of tokamaks”, Nucl. Fusion 54 123001
73. J Vega et al, 2022, “Disruption prediction with artificial intelligence techniques in tokamak plasmas”, Nat. Phys. 18 741
74. W Noble, 2006, “What is a support vector machine?”, Nat. Biotechnol 24 1565
75. A Santagiustina et al, 1995, “Studies of Tearing Mode Control in JET”, JET Proc. 22nd EPS Conf. on Controlled Fusion and Plasma Physics (European Conference Abstracts) 19c IV p 461
76. G Rattá et al, 2008, “Feature extraction for improved disruption prediction analysis at JET”, Rev. Sci. Instrum. 79 10F328
77. G Rattá et al, 2010, “An advanced disruption predictor for JET tested in a simulated real-time environment”, Nucl. Fusion 50 025005
78. G Rattá et al, 2012, “Improved feature selection based on genetic algorithms for real time disruption prediction on JET”, Fusion Engineering and Design 87 1670
79. R Moreno et al, 2014, “Robustness and increased time resolution of JET Advanced Predictor of Disruptions”, Plasma Phys. Control. Fusion 56 114003
80. E J Strait et al, 2019, “Progress in disruption prevention for ITER”, Nucl. Fusion 59 112012
81. M Lehnen et al, 2016, “Plasma disruption management in ITER” Preprint: 2016 IAEA Fusion Energy Conf. (Kyoto, 17–22 October 2016) EX/P6-39
82. P C de Vries et al, 2011, “Survey of disruption causes at JET”, Nucl. Fusion 51 053018
83. S Dormido-Canto et al, 2013, “Development of an efficient real-time disruption predictor from scratch on JET and implications for ITER”, Nucl. Fusion 53 113001
84. R Aledda et al, 2013, “Multivariate statistical models for disruption prediction at ASDEX Upgrade”, Fusion Eng. Des. 88 1297

85. J Vega et al, 2014, “Simulations of nuclear fusion diagnostics based on projections with Venn predictors and context drift detection”, Annals of Mathematics and Artificial Intelligence 74 223
86. V Vovk et al, 1999, “Machine learning applications of algorithmic randomness”, Proc. 16th Int. Conf. on Machine Learning (Bled, Slovenia)
87. J Vega et al, 2015, “Advanced Disruption Predictor Based On The Locked Mode Signal: Application To JET”, Proceedings of Science (ECPD2015) 028
88. S Esquembri et al, 2018, “Real-Time Implementation in JET of the SPAD Disruption Predictor Using MARTe”, IEEE Transactions on Nuclear Science 65 836
89. J Vega et al, 2020, “A linear equation based on signal increments to predict disruptive behaviours and the time to disruption on JET”, Nucl. Fusion 60 026001
90. J Vega et al, 2015, “Disruption precursor detection: Combining the time and frequency domains”, IEEE 26th Symposium on Fusion Engineering (SOFE)
91. C Reux et al, 2013, “Use of the disruption mitigation valve in closed loop for routine protection at JET”, Fusion Eng. Des. 88 1101
92. J Vega et al, 2017, “Assessment of linear disruption predictors using JT-60U data”, Fusion Eng. Des. 146 1291
93. L Garzotti et al, 2019, “Scenario development for D–T operation at JET”, Nucl. Fusion 59 076037
94. A H Boozer, 2012, “Theory of toakamk disruptions”, Phys. Plasmas 19 058101
95. S Gerasimov et al, 2020, “Overview of disruptions with JET-ILW”, Nucl. Fusion 60 066028
96. M Lehnen et al, 2015, “Disruptions in ITER and strategies for their control and mitigation”, Journal of Nucl. Materials 39 463

97. L Zakharov et al, 2012, "Understanding disruptions in tokamaks", Phys. Plasmas 19 055703

98. H Strauss et al, 2013, "Sideways wall force produced during tokamak disruptions", Nucl. Fusion 53 073018

99. R R Khayrutdinov et al, 2016, "Local and integral forces on the vacuum vessel during thermal quench in the ITER tokamak", Plasma Phys. Control. Fusion 58 115012

100. H Strauss et al, 2010, "Wall Forces Produced During ITER Disruptions", Phys. Plasmas 17 082505